学位論文

Quantum Phase Diagram of Helium Three Monolayer on HD Plated Graphite

（HD 膜を敷いたグラファイト上単原子層ヘリウム 3 の量子相図）

東京大学大学院　理学系研究科
物理学専攻

鎌田　雅博

平成 29 年 12 月　博士（理学）申請

Abstract

Helium three (^{3}He) monoatomic layer adsorbed on an atomically flat surface of graphite is an ideal testing ground for studying a strongly correlated Fermion system with spin $S = 1/2$ in two dimensions. One advantage of this system is its high purity. Since ^{3}He film is fabricated at low temperatures (a few K) and any atoms/molecules other than helium are frozen at an inside wall of the filling line at higher temperatures before reaching the sample cell, they cannot contaminate the ^{3}He film. One can control film coverage (areal density) to a large extent by just adding a known amount of ^{3}He atoms into the cell, without imposing lattice disorder. A ^{3}He monolayer shows a variety of quantum phases depending on its density: self-bound liquid, normal fermi liquid, commensurate solid, and incommensurate solid [1,2]. ^{3}He has such a large zero point motion that atom-atom exchange is significant even in the solid phase, resulting in interactions between nuclear spins, and it is known that the competition among the multiple spin exchange (MSE) interactions, which were originally recognized to be important to explain the peculiar nuclear magnetism in bulk solid ^{3}He [3] also plays an essential role to understand the magnetism of the 2D solid phases as well [4]. The competition causes strong magnetic frustration, and the frustration is stronger at lower densities. Especially, the 2nd layer low-density solid phase (C2 phase) is interesting. This phase is known as a characteristic phase so called the 4/7 commensurate solid whose counterpart does not exist in the bulk ^{3}He, and is stabilized by the delicate balance among the hard-core potential of ^{3}He-^{3}He interaction, the zero-point motion of ^{3}He atom, and the potential corrugation from the underlayer. The nuclear spin system of this phase is strongly frustrated due to the geometrical effect of a triangular lattice, in addition to the competition among MSE interactions, resulting in the quantum spin liquid (QSL) ground state with gapless excitations.

The magnetism of ^{3}He monolayers on graphite preplated with a monolayer of helium but with a bilayer of HD (^{3}He/HD/HD/gr) have also been studied [5, 6, 7, 8]. The density of the 2nd HD layer is lower than that of the 1st helium layer, which leads to the ^{3}He-C2 phase on the HD having the lowest areal density ever studied. The exchange interactions are greater at low densities, and therefore the ^{3}He/HD/HD/gr system is advantageous when one tries to reveal the nuclear magnetism of the C2 phase at the low T limit. However, the thermodynamic property of this system has not been studied intensively, and the quantum phase diagram near solidification density remains unclear.

In this work, we performed heat capacity (C) measurements on ^{3}He/HD/HD/gr system in wide ranges of temperature ($0.15 \leq T \leq 90$ mK), and density ($0.10 \leq \rho \leq 13.63$ nm^{-2}), in order to reveal the magnetic phase diagram of this system, and low-T thermodynamic properties of the QSL state in the C2 phase. Especially we made detailed measurements in the density region near solidification ($\rho = 4.5 - 5.5$ nm^{-2})

We observed that heat capacities at densities higher than 5.05 nm^{-2} have very broad peaks, and shift to lower temperature without changing the shape of the curve with

increasing density up to 5.92 nm^{-2}. Therefore this is a highly compressible phase in which the effective exchange interactions strongly depend on its density. Normalized specific heats of this phase behave like those of the C2 phase of the bilayer ^{3}He system. Thus we call this phase the C2-like phase. We found that the C2 phase compresses over an even wider density range of 17 % than that in the C2 phase ($\approx 8-9$ %). We thus speculate that the quantum liquid crystal is a more feasible phase for the C2 phase rather than the commensurate solid.

At the highest three densities in this study (ρ = 9.33, 11.01 and 13.63 nm^{-2}), we observed ferromagnetic heat capacities which share a similar temperature dependence with that of the high-density ferromagnetic solid phase in the bilayer ^{3}He system with a triangular lattice incommensurate to the lattice of the first layer.

We found a new phase at 4.74 nm^{-2} (C3 phase), which has not been reported previously. This phase is separated from the Fermi liquid and the C2-like phase via two transitional regions, and exists within a narrow density window (less than 2 %). Therefore the C3 phase is expected to be the "true" commensurate phase. The reason why the commensurate phase exists at such a low density where the bilayer system is in the liquid phase, is that the amplitude of the potential corrugation by the 2nd HD layer is greater by a factor of ≈ 3 compared with the 1st ^{3}He layer. The magnetic heat capacity of the C3 phase shows a very broad single peak at $T = 21$ mK followed by an unconventional temperature dependence of $C \propto T^{2/3}$ down to 0.3 mK. We also found that the magnetic susceptibility (χ), previously measured by other workers [8, 9], shows an equally anomalous temperature dependence of $\chi \propto T^{-1/3}$, which is not recognized by those authors. These facts indicate that the magnetic ground state of the C3 phase is the gapless QSL with novel elementary excitations such as Majorana Fermions.

At low densities ($\rho \lesssim 4.2$ nm^{-2}), measured heat capacities satisfy the $C = \gamma T$ dependence at low T, which is characteristic of the degenerate Fermi liquid. With increasing density effective mass of a ^{3}He quasiparticle, deduced from γ, shows the divergence up to $m^*/m = 4.4 \pm 0.3$ until 4.2 nm^{-2}. At the lowest densities ($0.1 \lesssim \rho \lesssim 0.7$ nm^{-2}), we observed the formation of the self-condensed liquid, judging from the γ coefficient smaller than the value of the noninteracting Fermi gas. Its critical density (0.7 nm^{-2}) is quantitatively consistent with that of 1 - 3 layers on graphite [1], but contradict recent Monte Carlo studies which claims that the potential corrugation play an essential role to stabilize the self-condensed liquid.

[1] D. Sato, K. Naruse, T. Matsui, and H. Fukuyama, Phys. Rev. Lett. **109**, 235306 (2012).
[2] D. S. Greywall, Phys. Rev. B **41**, 1842 (1990).
[3] M. Roger, J. H. Hetherington and J. M. Delrieu, Rev. Mod. Phys. **55**, 1 (1983).
[4] M. Roger, Phys. Rev. B **30**, 6432 (1984).
[5] M. Siqueira, C. P. Lusher, B. Cowan, and J. Saunders, Phys. Rev. Lett. **71**, 1403 (1993).
[6] A. Casey, H. Patel, J. Nyéki, B. P. Cowan, and J. Saunders, J. Low Temp. Phys. **113**,

265 (1998).
[7] A. Casey, H. Patel, J. Nyéki, B. P. Cowan, and J. Saunders, Phys. Rev. Lett. **90**, 115301 (2003).
[8] H. Ikegami, R. Masutomi, K. Obata, and H. Ishimoto, Phys. Rev. Lett. **85**, 5146 (2000).
[9] R. Masutomi, Y. Karaki, and H. Ishimoto, Phys. Rev. Lett. **92**, 025301 (2004).

論文要旨

グラファイト上に吸着したヘリウム３（^{3}He）単原子層はスピン 1/2 をもつ２次元強相関フェルミオン系の研究舞台として理想的な系である。この系の利点は純度の高さにある。^{3}He 膜は低温（数ケルビン）で作成されるためヘリウム以外の原子や分子はサンプルセルに到達する前に試料導入用ラインの内壁で凍ってしまい、^{3}He 膜を汚染する事はない。また格子欠陥を導入することなく膜の面密度を大きく変えることができるのも利点である。^{3}He 単原子層はその密度に応じて様々な量子相を示し、自己凝集液体、フェルミ液体、整合固体相、不整合固体相になる [1,2]。^{3}He はその大きな零点振動のため固体相においても原子交換の寄与が大きく、結果として核スピン間の相互作用が起こる。そして元々はバルク固体 ^{3}He の特異な磁性を説明するために考えられた多体交換相互作用 [3] が２次元固体の磁性を理解するにあたっても本質的であることが知られている [4]。これらの競合が強い磁気フラストレーションを起こし、低密度ほどより強くなる。特に、吸着第２層目の低密度固体（C2 相）は、4/7 整合相と呼ばれるバルク ^{3}He には対応する相がない特徴的な相が、^{3}He 間のハードコアポテンシャルや零点振動、下地による周期ポテンシャルの微妙なバランスによって実現することが知られており、興味深い。この相の核スピン系は、三角格子と多体交換相互作用の競合のためにバルク ^{3}He よりも強いフラストレーションが起こり、結果としてギャップレス励起をもつ量子スピン液体（QSL）になる。

下地にヘリウムを１層敷いた上の ^{3}He 単原子相だけでなく、下地を２層 HD にした系（^{3}He/HD/HD/gr）の磁性も研究されている。 [5,6,7,8]。HD 層の面密度はヘリウム層に比べて密度が小さいため、HD 上では知られている中で最も低い面密度の ^{3}He-C2 相が得られる。密度が低い方が ^{3}He の相互作用が大きくなるため、^{3}He/HD/HD/gr は低温極限での C2 相の核磁性を調べる上で有利である。しかし、この系の熱力学特性は詳細に調べられておらず、固化が起こる付近の密度の量子相図についてもまだよく知られていない。

本研究では ^{3}He/HD/HD/gr に対し、この系の磁気相図を明らかにすること及び C2 相のスピン液体状態の低温極限での熱力学特性を明らかにすることを目的として熱容量（C）測定を広い温度範囲（$0.15 \leq T \leq 90$ mK）及び密度範囲（$0.10 \leq \rho \leq 13.63$ nm^{-2}）にわたって行った。特に、固化が起こる付近の面密度域（$\rho = 4.5 - 5.5$ nm^{-2}）は詳細に測定した。

まず、5.05 nm^{-2} 以上の面密度域で熱容量は非常にブロードなピークをもち、5.92 nm^{-2} まで密度を増やすとその形を変えずに低温にシフトすることを観測した。このことから。これは大きな圧縮性を有する相であり、その交換相互作用は密度の変化に応じて比較的大きく変化することが分かった。交換相互作用 J で規格化した比熱の振る舞いが２層ヘリウム系の C2 相に似ていることから我々はこの相を C2-like 相と名付けた。C2-like 相は C2 相（8 - 9 %）より大きい 17%もの圧縮性をもつことが分かった。ここから C2-like 相は整合相よりも量子液晶相である可能性が高いと考えられる。

もっとも高い密度域（9.33, 11.01, 13.63 nm^{-2}）では、強磁性的な熱容量を観測し、２層ヘリウム系で見られた第１層目の格子に不整合な三角格子をもつ高密度強磁性固体と同様の温度依存性を示すことが分かった。

我々は、4.74 nm^{-2} 付近で、これまで報告された事のない新たな量子相を発見した（C3 相)。この相は 2 つの遷移領域でフェルミ液体相、及び C2-like 相と隔てられており、2 %以下の非常に狭い面密度範囲で存在する。この事実から C3 相が ”真の ” 整合相であると期待される。 2 層ヘリウム系ではまだ液体層であるような低い面密度で整合相が安定化できる要因として、下地の第 2 層目 HD が作る周期ポテンシャルの振幅が第 1 層目 ^{3}He のそれの 3 倍程度大きい点が挙げられる。C3 相の磁気比熱は $T = 21$ mK で広いシングルピークをもち、低温では $C \propto T^{2/3}$ という非常に特異な温度依存性が 0.3 mK まで観測された。我々はまた過去に測定された帯磁率 (χ) [8, 9] の結果が、原著者らは指摘していなかったものの $\chi \propto T^{-1/3}$ とやはり特異な温度依存性を示すことを見出した。これらの事実は、C3 相の磁気基底状態がギャップレス QSL であり、マヨラナフェルミオンなどの新規な素励起を持つことが期待される。

低密度域 ($\rho \lesssim 4.2$ nm^{-2}) では、フェルミ液体に特徴的な $C = \gamma T$ の熱容量が観測された。この γ から求まる ^{3}He 準粒子の有効質量 m^* は密度とともに増加し 4.2 nm^{-2} で $m^*/m = 4.4 \pm 0.3$ まで増大する。もっとも低密度の液体領域 ($0.10 \lesssim \rho \lesssim 0.7$ nm^{-2}) において、γ 係数が相互作用のないフェルミ気体の値よりも小さいことから自己凝集液体が形成していることを観測した。臨界密度の値 (0.7 nm^{-2}) はグラファイト上 1 - 3 層目で観測された値 [1] と定量的に一致するが、下地のポテンシャルが自己凝集相の安定化に本質的な役割を果たすとする最近のモンテカルロ計算の結果と矛盾する。

[1] D. Sato, K. Naruse, T. Matsui, and H. Fukuyama, Phys. Rev. Lett. **109**, 235306 (2012).
[2] D. S. Greywall, Phys. Rev. B **41**, 1842 (1990).
[3] M. Roger, J. H. Hetherington and J. M. Delrieu, Rev. Mod. Phys. **55**, 1 (1983).
[4] M. Roger, Phys. Rev. B **30**, 6432 (1984).
[5] M. Siqueira, C. P. Lusher, B. Cowan, and J. Saunders, Phys. Rev. Lett. **71**, 1403 (1993).
[6] A. Casey, H. Patel, J. Nyéki, B. P. Cowan, and J. Saunders, J. Low Temp. Phys. **113**, 265 (1998).
[7] A. Casey, H. Patel, J. Nyéki, B. P. Cowan, and J. Saunders, Phys. Rev. Lett. **90**, 115301 (2003).
[8] H. Ikegami, R. Masutomi, K. Obata, and H. Ishimoto, Phys. Rev. Lett. **85**, 5146 (2000).
[9] R. Masutomi, Y. Karaki, and H. Ishimoto, Phys. Rev. Lett. **92**, 025301 (2004).

Contents

Chapter 1

Introduction

A wide variety of studies have been performed on low dimensional quantum systems, through theoretical and experimental approaches. These systems have revealed many interesting phenomenon which cannot be seen in the bulk three dimensional (3D) systems, thanks to enhanced quantum fluctuations or interparticle correlation. Here we show some examples.

In two dimensional (2D) systems with continuous symmetry, the finite temperature phase transition to a state with long range order is prohibited, which is known as the Mermin-Wagner theorem. However, Kosterlitz and Thouless predicted the finite temperature phase transition (KT transition) between vortex-antivortex bound and unbound states [1]. The KT transition was experimentally observed in a superfluid ^{4}He thin film [2]

The 2D electron systems in the inversion layer of a MOSFET in high magnetic field have quantised energy levels (Landau levels), and its Hall resistance is also quantised in units of h/e^2, where h is Planck constant and e is the elementary charge [3]. Later, the fractionalized quantisation of the Hall resistance due to strong electron-electron interactions was discovered [4]

High temperature superconductivity was first found in the cuprate $La_{2-x}Ba_xCuO_4$ [5]. In this material quasi-2D CuO planes become.

Helium three (^{3}He) monoatomic layer physisorbed on atomically flat graphite substrates is an ideal system to study strongly correlated fermions with spin $S = 1/2$. In this system one can easily change the areal density to a large extent without imposing lattice distortion, and the ^{3}He film shows a variety of quantum phases depending on its density. The 2nd layer low density solid phase (C2 phase) is especially interesting, because this phase is believed to be the commensurate solid with the triangular lattice, and its nuclear spin system is known as the candidate of a quantum spin liquid (QSL) state [6]. The magnetic susceptibility of this phase shows the gapless behavior down to 10 μK [7]. The magnetic specific heat shows T-linear behavior, which also indicates the gapless excitations. However, this T-linear behavior is observed within the relatively limited temperature range, so it is still unclear whether this is the behavior at low T limit. By replacing the 1st layer helium by a bilayer of HD molecule, one can enhance the exchange interaction among ^{3}He atoms on the topmost layer, thanks to the lower density of the second layer HD. It is advantageous to investigate the low T behavior. However, in spite of the advantage, the thermodynamic studies of the ^{3}He films on a bilayer of HD are

limited. Moreover, the phase diagram of the ^{3}He layer on the HD is not well understood compared with the bilayer ^{3}He systems.

In this thesis, we report the results of heat capacity measurements on ^{3}He on a bilayer of HD in wide range of temperature and density region ($0.15 < T < 90$ mK, $0.10 < \rho < 13.63$ nm^{-2}), in order to clarify the thermodynamic property of the QSL state at low T limit, and to reveal the quantum phase diagram of this system.

The thesis is organized as follows. In Chapter 2 the background knowledge related to this work is briefly reviewed. In Chapter 3 the experimental apparatus and methods of heat capacity measurements are described. In Chapter 4 how to prepare a bilayer of HD and ^{3}He films is described. The results of our heat capacity measurement are described from Chapter 5 to 8. The quantum phase diagram of ^{3}He/HD/HD/gr at $T = 0$, revealed in this work, is shown in Fig.1.1. In Chapter 5 the frustrated magnetism of the C2-like and IC phases are discussed. In Chapter 6 the existence of a new quantum phase which have not been reported (the C3 phase in the figure) and its unconventional nuclear magnetism are discussed. In Chapter 7 the critical behavior of the normal Fermi liquid near localization are discussed. In Chapter 8 the liquid puddles in the 1st and 2nd layer ^{3}He on HD are reported. In Chapter 9 the summary of this work and future prospects are described.

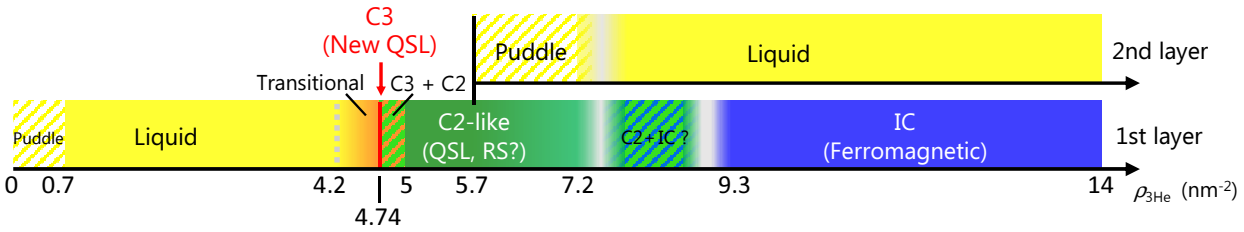

Fig. 1.1: $T = 0$ phase diagram of ^{3}He film on graphite preplated with a bilayer of HD. QSL and RS represents the quantum spin liquid and the random singlet.

Chapter 2

Background

2.1 Helium-helium and helium-graphite interactions

Helium atom

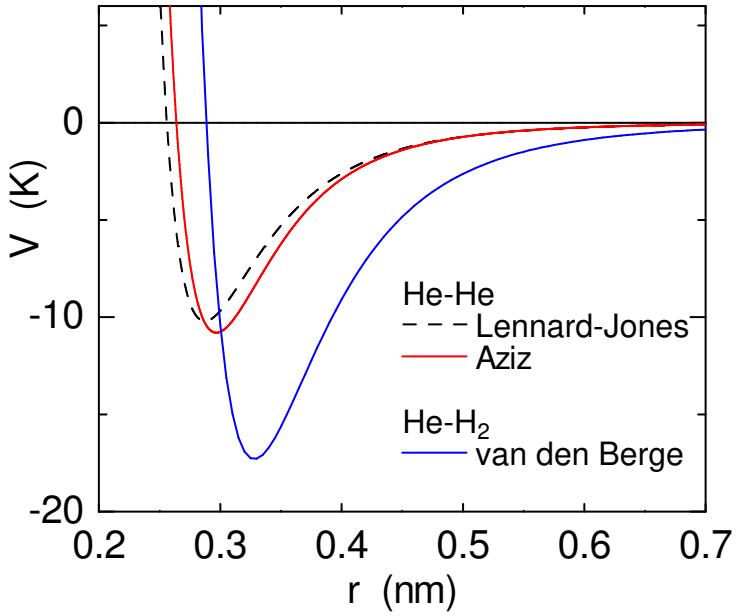

Fig. 2.1: Interatomic potentials between two helium atoms. The dashed line is the Lennard-Jones potential, and the red solid line is the Aziz potential (Ref.[8]). A potential between a helium atom and a hydrogen molecule is also plotted as the blue solid line (Ref.[9]).

Helium atom is an element with atomic number 2, which have two electrons in 1s orbital. Helium is the smallest atom which has closed shell and spherical symmetry. There are two stable isotopes of helium, namely, ^{3}He and ^{4}He. ^{3}He is fermion with $S = 1/2$ nuclear spin and ^{4}He is Boson with no nuclear spin.

The interatomic interactions between helium atoms are electrical dipole-dipole interaction (Van der Waals force) if the atomic distance is large. Although helium has spherical symmetry, the fluctuating charge distribution causes the weak attractive force. However, if the atomic distance is small, the interactions are dominated by strong repulsion due to overlap of the electronic orbitals. These interactions can be expressed as the Lennard-Jones (LJ) potential

$$V(r) = 4\epsilon \left[\left(\frac{\sigma}{r}\right)^{12} - \left(\frac{\sigma}{r}\right)^{6} \right] \tag{2.1}$$

where, $\epsilon = 10.22$ K, $\sigma = 0.2556$ nm. The LJ potential is shown in Fig.2.1. It is known that the potential proposed by Aziz *et al.* [8] shows good agreement with the experimental results rather than the LJ potential. The Aziz potential is also shown in Fig.2.1. The potential between a helium atom and a Hydrogen molecule by van der Bergh [9] is also plotted in Fig.2.1 as the blue solid line.

Thanks to its weak interaction and extremely large zero point motion due to small atomic mass, helium is the only material which do not solidify even at $T = 0$ under 1 atm. Helium solidify at about 29 bar for ^{4}He and 35 bar for ^{3}He at $T = 0$. Even in the solid phase, the large zero point motions enable the exchange between. That is why the solid helium is called "quantum solid". Moreover, due to its strong hard core repulsion, exchange interactions among more than two atoms cannot be ignored.

Graphite substrate

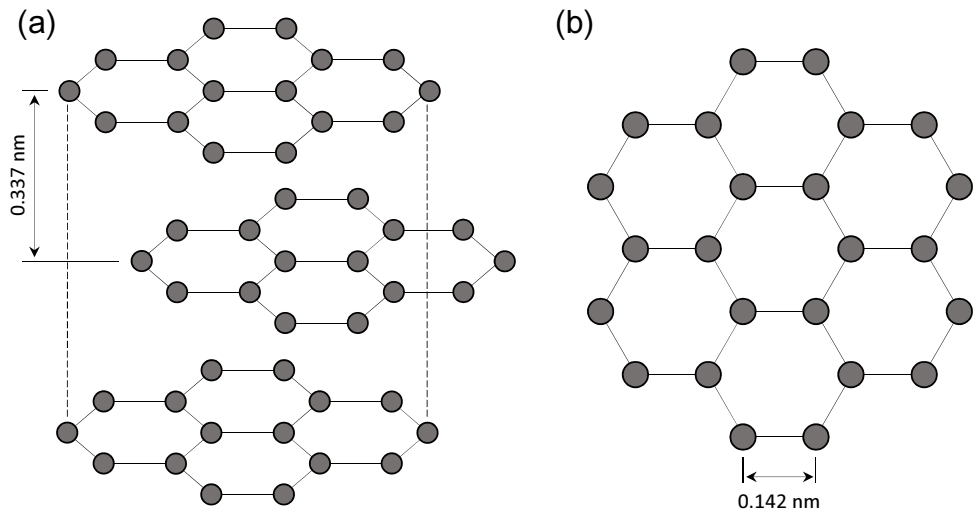

Fig. 2.2: (a) Schematic view of crystalline structure of graphite with the common ABAB stacking. (b) Graphite lattice seen from the c-axis.

Graphite is a layered material composed of carbon atoms. Honeycomb graphene sheets are piled up with ABAB type stacking as shown in Fig.2.2 (a). In this study, we used exfoliated graphite Grafoil [11] as an adsorption substrate for ^{3}He monolayers. Grafoil is often used for studies on Helium films because it has quite large specific surface area ($\approx$ 20 m^2/g). Grafoil consists of small platelets of graphite. A typical platelet size is 10 – 20 nm, and a typical thickness is 10 graphene sheets. A scanning tunneling microscopy (STM) study observed that the surfaces of the platelets are atomically flat except about 10 % of inhomogeneities [12]. Figure 2.3 shows the adsorption potentials between graphite and a helium atoms as a function of the distance from graphite surfaces z [10, 13]. A, S, SP in the figure represent positions which are shown in the inset picture. The deepest potential is about -200 K at the point S. A helium atom feels the corrugated potential of graphite. The amplitude of the potential corrugation is approximately 10 K for the 1st layer but decreases rapidly as z increase.

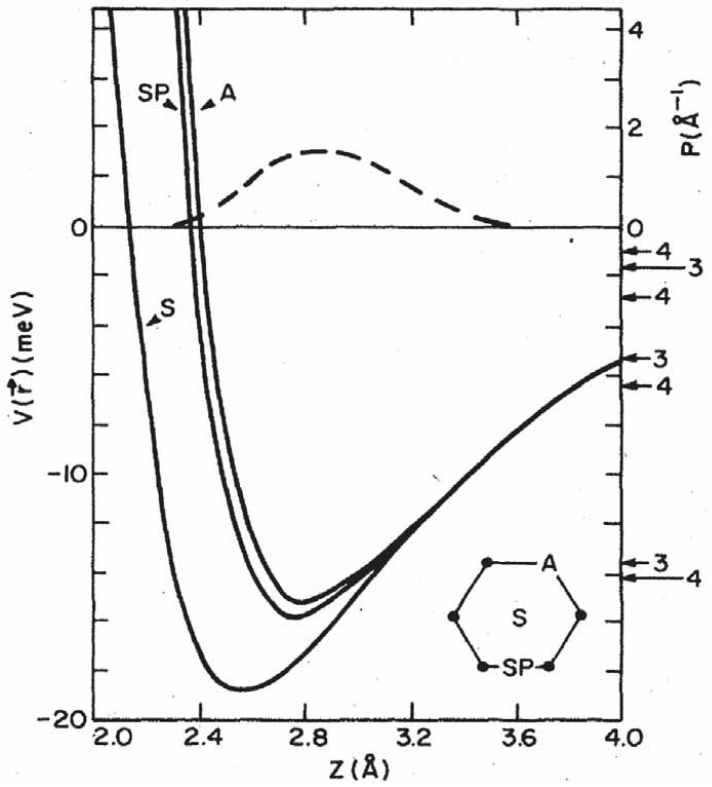

Fig. 2.3: The adsorption potential between a helium atom and a graphite surface (Ref.[10]). A, S, and SP represent graphite symmetry points described in the lower right picture The dashes line is the probability density of ^{4}He in the laterally averaged potential. The arrows at the right of the graph show enegy levels of ^{3}He and ^{4}He

2.2 Quantum phases of various ^{3}He monolayers adsorbed on graphite

Helium monolayers adsorbed on the graphite surface have been studied intensively. These are ideal test grounds for studying 2D quantum systems, thanks to their high purity and atomically flat surfaces of the graphite substrate. Figure 2.4 shows the calculated density distribution of the ^{4}He films on Grafoil [14]. The 1st and 2nd layers are well isolated and regarded as good 2D systems.

Figure 2.5 shows the three different types of ^{3}He monolayers: the 1st layer ^{3}He (^{3}He/gr), the 2nd layer ^{3}He (^{3}He/^{3}He/gr and ^{3}He/^{4}He/gr), and the ^{3}He monolayer on graphite preplated with a bilayer of Hydrogen (^{3}He/H_2/H_2/gr and ^{3}He/HD/HD/gr). By changing underlayers ^{3}He monolayers feel different potential corrugations. Table 2.1 shows the densities of atom/molecule layers below the topmost ^{3}He layers, $\rho_{\rm substrate}$, and the ones of the C2 phases ρ_{C2}. The ^{3}He/HD/HD/gr system has the C2 phase whose density is lower than the bilayer ^{3}He systems. The C2 phase with even lower density is expected for the ^{3}He/H_2/H_2/gr system which has the smallest value of $\rho_{\rm substrate}$. However, among three isotopes of hydrogen molecules (H_2, HD, D_2), H_2 and D_2 are not preferable to be used in the experiments at millikelvin temperatures or lower, because they release the large

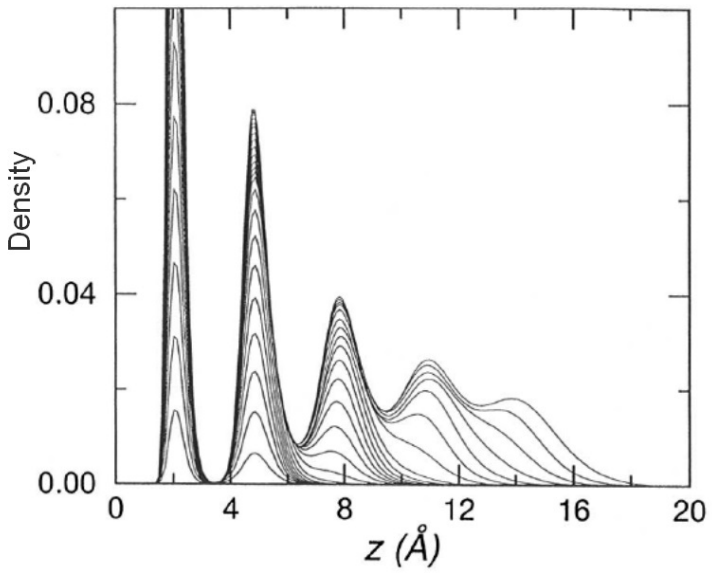

Fig. 2.4: Density profile of ^{4}He on a graphite surface. z is the distance from the top graphene layer (Ref.[14])

ortho-para conversion heat [15]. The difference in the density of ^{3}He momnolayers strongly affects exchange interactions J among ^{3}He atoms on the topmost layer. The interaction J is enhanced, and J of the C2 phase of ^{3}He/HD/HD/gr is approximately 10 times larger than that of the bilayer ^{3}He systems [7].

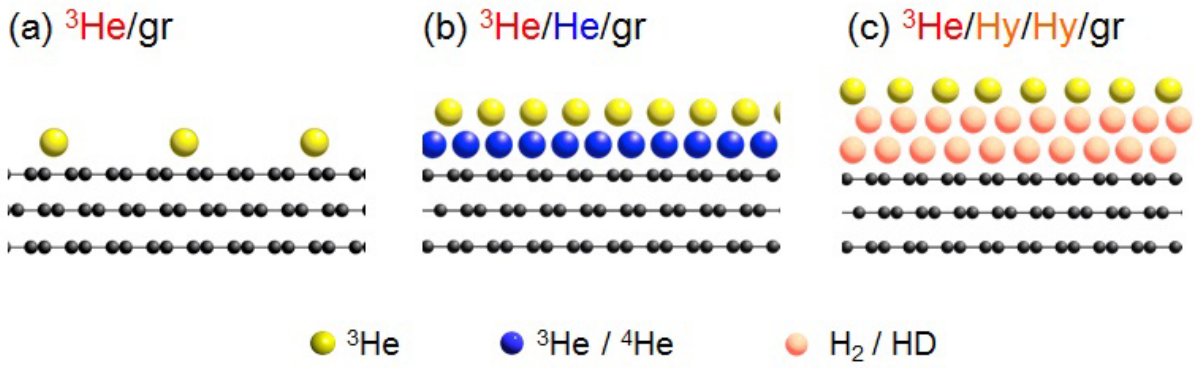

Fig. 2.5: Schematic pictures of ^{3}He monolayers on (a) bare graphite surface (^{3}He/gr), (b) graphite preplated with a helium monolayer (^{3}He/^{3}He/gr and ^{3}He/^{4}He/gr), and (c) graphite preplated with a bilayer of Hydrogen (^{3}He/H_2/H_2/gr and ^{3}He/HD/HD/gr)

Figure 2.6 compares the corrugated potentials between ^{3}He/HD/HD/gr and ^{3}He/^{3}He/gr systems [22]. The corrugated potentials of a bilayer of HD and monolayer of ^{3}He on graphite is shown in Fig.2.6 (a). The x-axis is the distance in the direction indicated by

	^{3}He/^{3}He/gr	^{3}He/^{4}He/gr	^{3}He/HD/HD/gr	^{3}He/H_2/H_2/gr	^{3}He/D_2/D_2/gr
$\rho_{\mathrm{substrate}}$ (nm^{-2})	11.6 [16]	12.0 [16]	9.1−9.2 [17, 18]	8.65 [19]	9.32 [19]
ρ_{C2} (nm^{-2})	6.4 [6]	6.8 [20]	5.2−5.5 [18, 21]	(4.9)	(5.3)

Table 2.1: Listed densities of atom/molecule layers below the topmost ^{3}He layers, $\rho_{\mathrm{substrate}}$, and the densities of the C2 phases ρ_{C2}. The C2 phases of ^{3}He/H_2/H_2/gr and ^{3}He/D_2/D_2/gr have not been observed experimentally, so ρ_{C2} of them are estimated as 4/7 of $\rho_{\mathrm{substrate}}$.

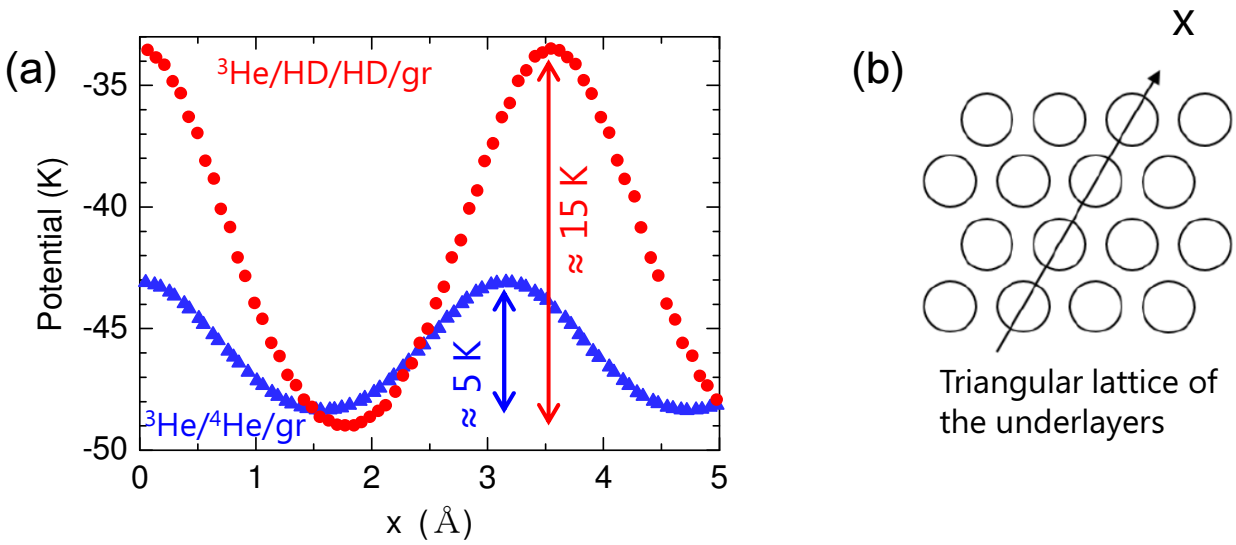

Fig. 2.6: (a) Potential corrugations which ^{3}He atoms on the topmost layer feel. The red and blue symbols represent the potential corrugation of a bilayer HD on graphite and a monolayer ^{3}He on graphite, respectively. The direction of the x-axis is indicated as the black arrow in (b). The origin of the x-axis is at the top of underlying HD/^{3}He.

the black arrow in Fig.2.6 (b), where the open circles represent triangular lattices of the HD or ^{3}He layer. The origin of the x-axis is at the top of underlying HD/^{3}He. In this calculation the densities of HD and ^{3}He underlayers are 9.1 and 11.6 nm^{-2}, respectively. The averaged potential of the 2nd HD layer is weaker than the 1st ^{3}He layer due to the longer distance from graphite surface. The amplitude of the potential corrugation of the 2nd HD layer is $\approx$ 15 K, three times greater than that of the 1st ^{3}He layer of $\approx$ 5 K. What causes the stronger potential corrugation in the HD layer is the larger lattice constant and deeper minimum of the helium-hydrogen potential (see Fig.2.1).

In the following, Phase diagrams of the ^{3}He monolayers are introduced.

2.2.1 1st layer ^{3}He on graphite (^{3}He/gr)

Figure.2.7(a) shows the phase diagram of the 1st layer ^{3}He on graphite.

At density below 4.3 nm^{-2}, the ^{3}He layer is in the Fermi liquid phase [24, 28]. Large zero-point energy of ^{3}He overcomes the potential corrugation from the graphite substrate. In the lowest density range ($0 < \rho < 0.8$ nm^{-2}) the liquid do not cover the whole surfaces of graphite and forms the self-condensed phase by interatomic interactions among ^{3}He atoms [23]. At $\rho > 4.3$ nm^{-2} , the Fermi liquid and a commensurate solid phase coexist.

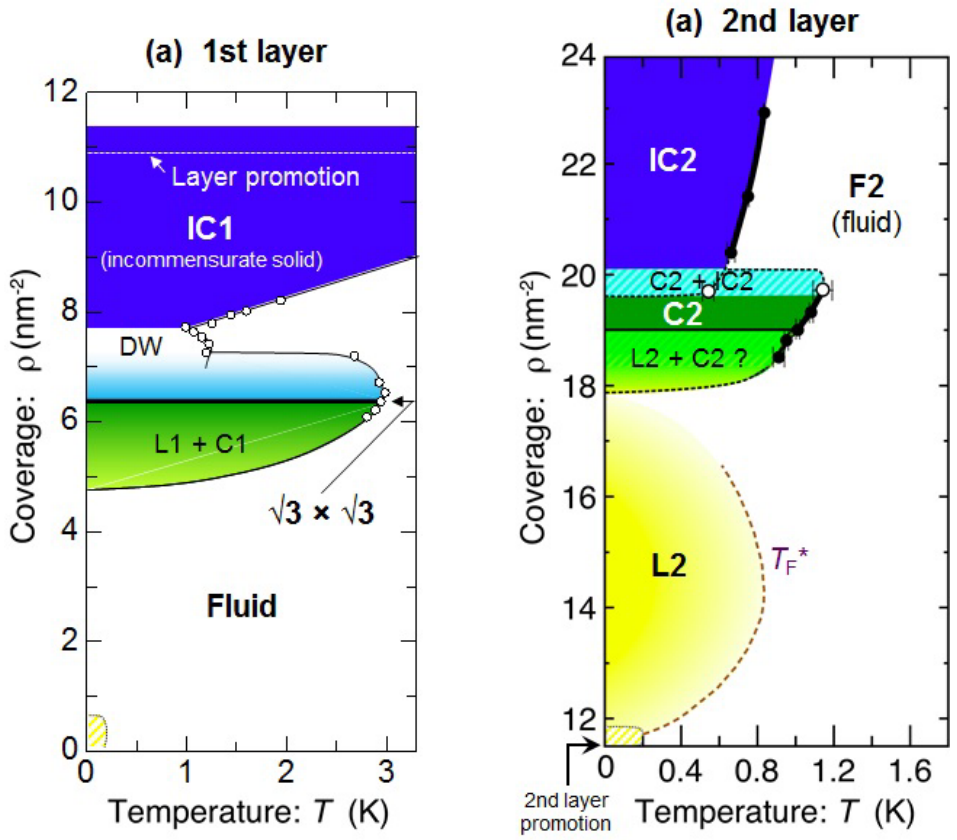

Fig. 2.7: Phase diagrams of (a) the 1st layer [23, 24] and (b) the 2nd layer ^{3}He films on graphite [16, 23, 25]. L, F, C, DW, and IC denote liquid, fluid, commensurate solid, domain wall, and incommensurate solid, respectively. A + B denotes two phase coexistence region.

The fraction of the solid phase increases with increasing density, and formation of the commensurate solid phase is completed at 6.37 nm^{-2}. This commensurate solid phase is called "$\sqrt{3} \times \sqrt{3}$ phase" in which ^{3}He atoms occupy on one third of the central sites of the hexagonal lattice of graphite, as depicted in Fig.2.8. This structure is interpreted by the three state Potts model [29]. The model predicts the critical exponent of heat capacity of 1/3, and the value is experimentally observed [30]. The commensurate solid appears only in the 2D phase diagram because this phase is stabilized by the potential corrugation of the graphite substrate. The $\sqrt{3} \times \sqrt{3}$ structure melts above 3.0 K [30]. The $\sqrt{3} \times \sqrt{3}$ solid can accommodate 2 % of vacancies but collapses easily by adding ^{3}He [31]. The structure between 6.37 and 7.8 nm^{-2} is considered to be the striped domain wall phase like H_2 or D_2 monolayers on graphite [32, 33]. At $\rho > 7.8$ nm^{-2}, the ^{3}He layer forms the incommensurate (IC1) solid. In this solid ^{3}He atoms form a triangular lattice but the lattice is not registered to the lattice of graphite substrate [34]. A promotion to the 2nd layer occurs at 10.9 nm^{-2}. A neutron diffraction measurement demonstrated that the density of the 1st layer increases by 5 % even after the layer promotion [35], because of additional pressure applied by the 2nd ^{3}He layer.

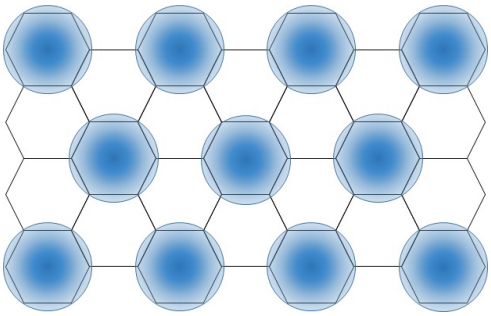

Fig. 2.8: Structure of the $\sqrt{3} \times \sqrt{3}$ commensurate phase of adsorbent (circle) in the submonolayer. the honeycomb lattice of the top graphite surface is also shown. The adsorbent atoms occupy 1/3 of the hollow site of the hexagonal lattice.

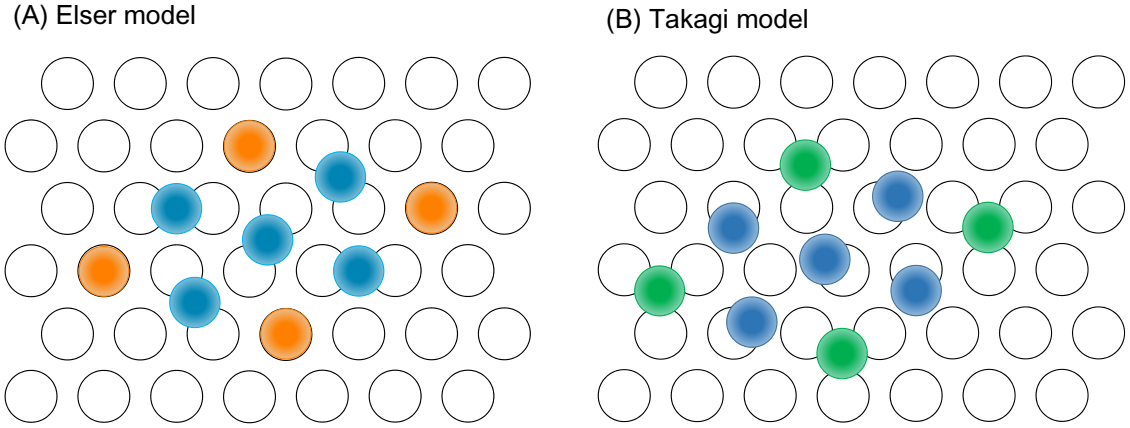

Fig. 2.9: Two different structures for the 4/7 commensurate phase proposed by (a) Elser (Ref.[26]) and (b) Takagi (Ref.[27]). The black open circles and colored ones are the 1st and 2nd layer particles. Symbols with different colors represent the different types of adsorption sites.

2.2.2 2nd layer of ^{3}He on graphite (^{3}He/^{3}He/gr and ^{3}He/^{4}He/gr)

Figure.2.7(b) shows the 2nd layer phase diagram [16]. The vertical axis represents the total density of ^{3}He including the 1st layer. This phase diagram is qualitatively similar to that of the 1st layer.

At $0 < \rho < 0.6$ nm^{-2}, the self-condensed liquid appears like the 1st layer. At higher densities the ^{3}He film forms Fermi liquid phase spreading over the whole surface of the substrate. As the density increase, the effective mass of the ^{3}He quasiparticles m^* diverges, which indicate the Mott-Hubbard transition [25, 36]. What follows after this effective mass enhancement is still controversial. A study on the ^{3}He/^{3}He/gr system indicated that solidification is 1st order [25], but an intensive study on ^{3}He/^{4}He/gr system dieplayed that the transition cannot be explained by such a simple picture [36].

The formation of the C2 phase is completed at 6.4 nm^{-2} for ^{3}He/^{3}He/gr [25], and 6.8 nm^{-2} for ^{3}He/^{4}He/gr [20, 36]. The density of each system is 4/7 of that of underlayer. This phase is believed to be a commensurate phase The melting temperature of the C2 phase is 1.0 – 1.1 K, lower than that of the $\sqrt{3} \times \sqrt{3}$ phase [16], which means the stability of the C2 phase is suppressed compared to the $\sqrt{3} \times \sqrt{3}$ phase. From the density ratio of the 2nd to the 1st layer, or its lattice structure, the C2 phase is called the 4/7 or $\sqrt{7} \times \sqrt{7}$ phase. Two types of lattice structures of the 4/7 phase were proposed by different authors

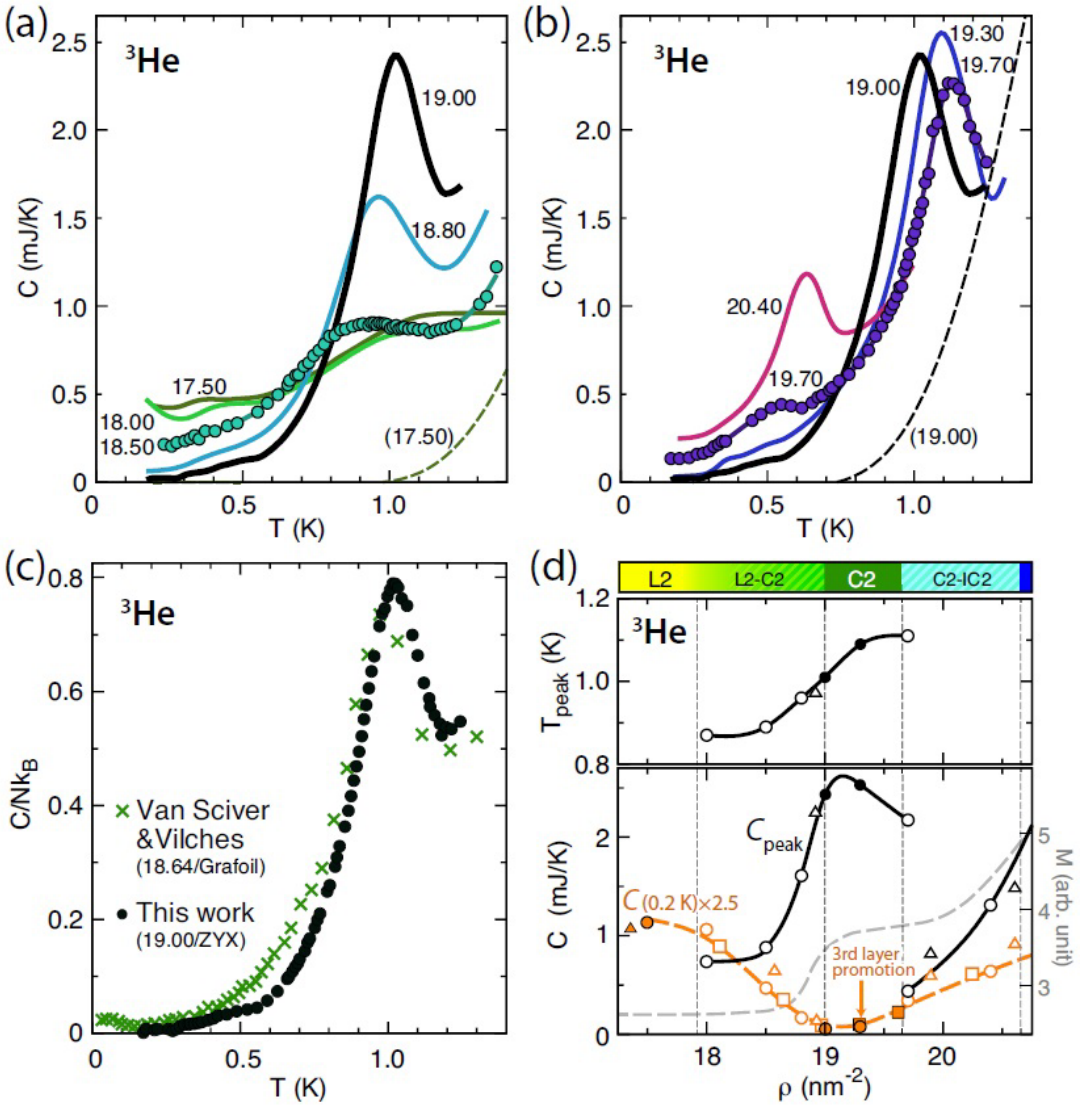

Fig. 2.10: Heat capacities of a bilayer of ^{3}He on ZYX graphite substrate [16] in two-phase coexistence regions between (a) liquid-C2, and (b) C2-IC2 phases. (c) The melting peaks of the C2 phases on ZYX and Grafoil substrates. (d) The C2 peak temperature $T_{\rm peak}$ and height $C_{\rm peak}$. At the top of the panel, $T = 0$ phase diagram is shown.

as shown in Fig.2.9. (a) is by Elser *et al.* [26] and (b) is by Takagi [27]. Both structures have two different adsorption sites. However, a direct observation of the lattice structure by neutron diffraction measurements has not been successful.

Recent melting heat capacity measurements on bilayers of ^{3}He and ^{4}He on ZYX graphite substrate by Nakamura *et al.* were inconsistent with the traditional picture of the 4/7 commensurate phase. heat capacities of the bilayer of ^{3}He is shown in Fig.2.10. The C2 peak exists over wide range of areal density ($\Delta\rho_{C2}/\rho_{C2} \approx 0.08 - 0.09$), but narrow density range is expected for the commensurate solid. This result suggests that the C2 phase is not the commensurate solid with totally broken symmetry but a new kind of state "quantum liquid crystal" in which rotational and/or translational symmetries are

partially broken.

At the highest densities ($\rho > 9.5$ nm^{-2}), the incommensurate solid (IC2) phase is formed like the 1st layer. This solid has a triangular lattice which is not commensurate to the triangular lattice of the 1st layer IC solid [34]. The phase transition between the C2 and IC2 phases is the 1st order [16, 37].

2.2.3 ^{3}He monolayer on graphite preplated with a bilayer of Hydrogen (^{3}He/H_2/H_2/gr and ^{3}He/HD/HD/gr)

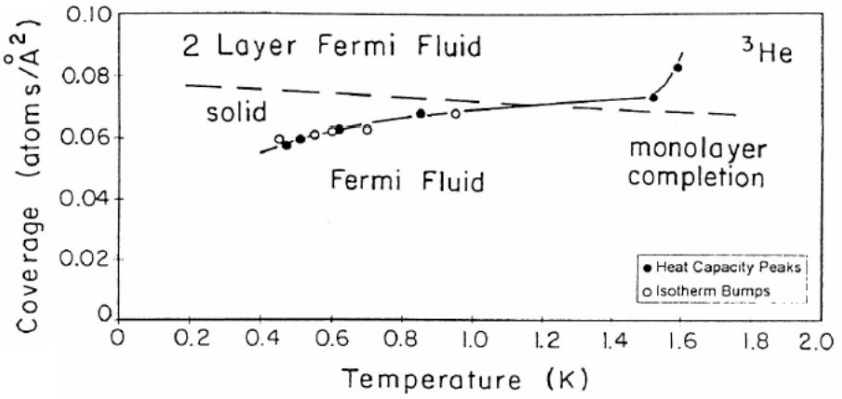

Fig. 2.11: High-T phase diagram of the ^{3}He monolayer adsorbed on Grafoil preplated with a 2.15 layer of H_2, determined by heat capacity measurements (Ref.[38]) Note that the reduction of the surface area to 85 % of the total area due to the excess H_2 is taken into account to determine the ^{3}He densities. The solid line corresponds to the melting line of a solid phase.

Compared with the bilayer ^{3}He systems (^{3}He/^{3}He/gr and ^{3}He/^{4}He/gr), the phase diagram of the ^{3}He monolayer on a bilayer of hydrogen is less investigated.

The phase diagram of the ^{3}He monolayer on a 2.15 layer of H_2 at $T > 0.2$ K is studied by Ramos *et al.* through heat capacity measurements [38]. Their results are shown in Fig.2.11. Although the low density commensurate phase was reported in the ^{4}He/H_2/H_2/gr system [38] at around 6 nm^{-2}, there were no sign of such a phase in ^{3}He at least down to 5.8 nm^{-2} [38]. Note that the reduction of the surface area by 15 % due to the excess H_2 was considered to calculate the ^{3}He densities.

The ^{3}He/HD/HD/gr system was studied for $T < 60$ mK. At $1 \leq \rho \leq 5$ nm^{-2}, the Fermi liquid behavior was observed [39]. The divergence of the quasiparticle effective mass m^* with increasing density up to $m^*/m \approx 13$ indicated the Mott-Hubbard transition towards the critical density of $n_c = 5.1$ nm^{-2}. The solidification was reported as weakly the 1st order transition [39]. A NMR measurements by Siqueira *et al.* observed that the solidification was completed at 5.2 nm^{-2} [21], but a heat capacity study by the same group reported that the ^{3}He layer solidified at 5.4 - 5.5 nm^{-2} [18]. A NMR study by Ikegami *et al.* observed the remnant liquid contribution at 5.2 nm^{-2} [17]. At 6.8 nm^{-2}

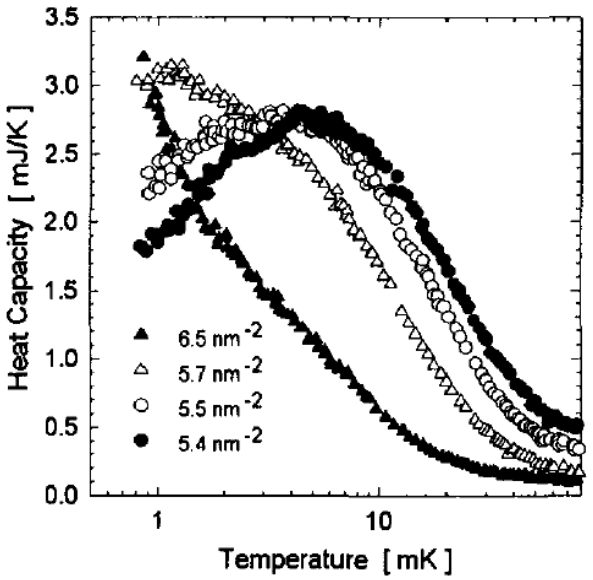

Fig. 2.12: Heat capacities of the ^{3}He monolayers for the ^{3}He/HD/HD/gr system in the solid phase (Ref.[18]).

the layer promotion to the 2nd ^{3}He layer (or 4th layer including the HD layers) occurs [18]. At $6.8 < \rho < 7.5$ nm^{-2}, ^{3}He in the 2nd layer forms the self-condensed liquid.

There was an NMR study of the ^{3}He film on a trilayer of HD (^{3}He/HD/HD/HD/gr) in order to make the quantum solid with even smaller densities [40]. However the results agreed excellently with the bilayer HD system. This means that the potential corrugations of a bilayer and trilayer of HD is almost the same.

2.2.4 Amorphous ^{3}He

In this thesis we study ^{3}He monoatomic layer adsorbed on atomically flat surfaces of the graphite substrate. However, in reality, not all ^{3}He introduced is adsorbed on flat surfaces, but a part of ^{3}He is adsorbed on the surface heterogeneities such as platelet edges. In the case of Grafoil, which is used in this work, 10 - 15 % of the total surface area is the heterogeneities [12]. ^{3}He adsorbed on the surface heterogeneities is believed to be in the amorphous solid state because of the surface roughness. Hereafter this kind of solid ^{3}He is called "amorphous ^{3}He". The existence of amorphous ^{3}He is pointed out by a number of experimental studies on ^{3}He adsorbed on graphite [17, 23, 25, 39, 41]. It is believed that physical properties of the amorphous ^{3}He can be explained by a model proposed by Golov and Pobell [42]. Their model is originally built to explain the weak temperature dependence of heat capacities of ^{3}He on vycor glass, and is thought to be valid for ^{3}He adsorbed on rough surfaces.

The Golov-Pobell model assumes the random distribution of ^{3}He interatomic distances which results in the broad distribution of interatomic exchange J, and J fulfill

$$\frac{dN(J)}{d\ln J} = const., \tag{2.2}$$

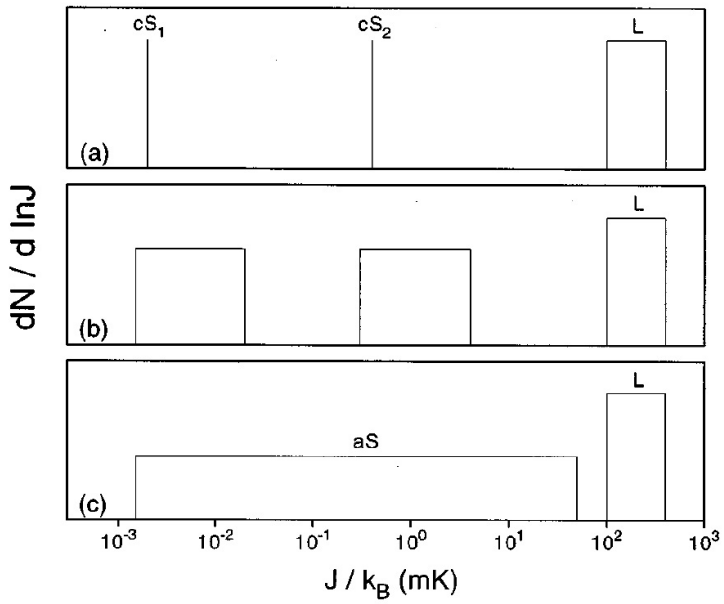

Fig. 2.13: Schematic representation of the distribution of exchange parameter $dN/d\ln J$ on homogeneous (a), moderately inhomogeneous (b), and extremely inhomogeneous (c) substrates (Ref.[42], marked are the phases: L, liquid; cS_i, crystalline solid in the 1st and 2nd layers; aS, amorphous solid).

where $N(J)$ is the distribution of spins with exchange interaction J. Since the entropy change due to ΔN spins with $S = 1/2$ can be written as $\Delta S = \Delta N k_{\rm B} \ln 2$, the magnetic heat capacity is expressed as

$$C(T) = \frac{TdS}{dT} = k_{\rm B} \ln 2 \frac{dN(T)}{d\ln T}, \tag{2.3}$$

where $N(T)$ is the effective number of disordered spins at temperature T. By assuming that the spins ordered at the ordering temperature $T \approx J/K_{\rm B}$ do not interact with other spins below the temperature, Eq. (2.2) become

$$\frac{dN(T)}{d\ln T} = const. \tag{2.4}$$

From Eqs.(2.3) and (2.4), the heat capacity is independent of the temperature. If the range of the distribution is from T_l to T_h, the magnitude of heat capacity C_0 is

$$C_0 = k_{\rm B} \ln 2 \frac{N_0}{\ln(T_h/T_l)}. \tag{2.5}$$

The J distribution described as Eq.(2.2) also yield the magnetic susceptibility χ_0 as follows,

$$\chi_0(T) = \frac{c_0}{T} \frac{\ln(T/T_l)}{\ln(T_h/T_l)}, \tag{2.6}$$

where c_0 is the curie constant.

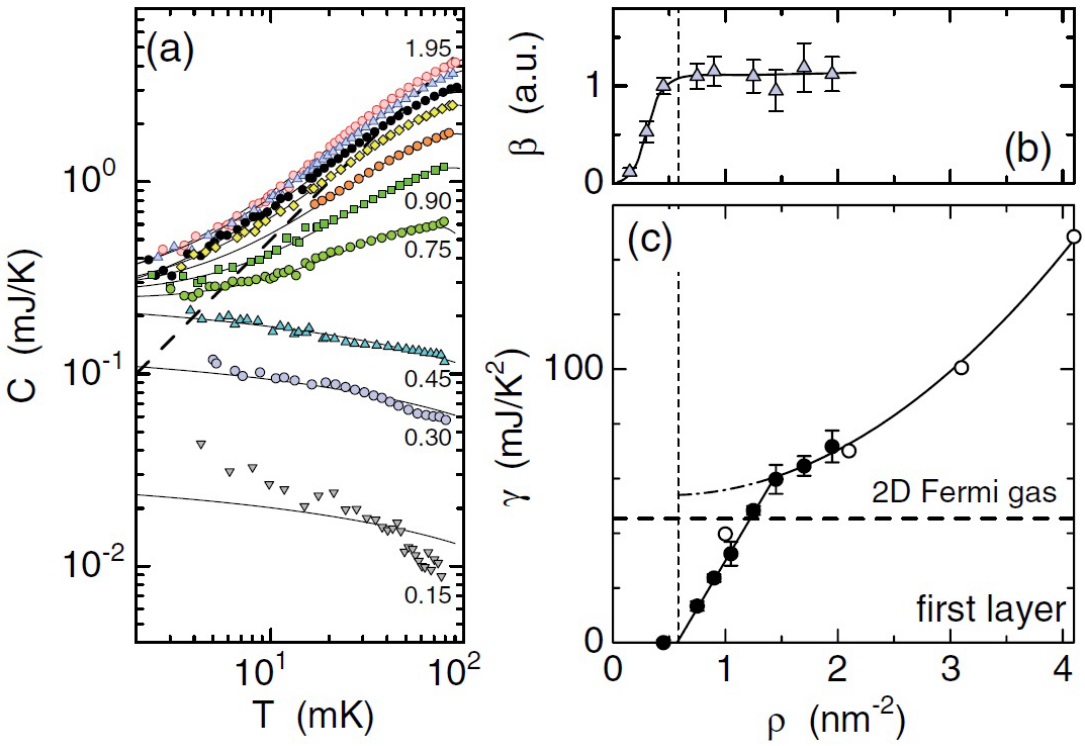

Fig. 2.14: Behavior of low density ^{3}He layer directly adsorbed on an exfoliated graphite (Grafoil) surface (Ref.[23]). (a) Heat capacities of the 1st layer of ^{3}He at densities from 0.15 to 1.95 nm^{-2} from bottom to top. The solid lines are fittings to Eq(.2.7). The dashed line is a heat capacity expected for the degenerated Fermi gas covering the whole surface of the substrate. (b) Density dependence of the amount of amorphous ^{3}He. (c) Density dependence of the γ coefficients of the T-linear term. The open circles are from another study [43]. The horizontal dashed line represents the value of the noninteracting Fermi gas.

Most previous studies on the ^{3}He monolayer on graphite adopted theGolov-Pobell model and assume the amorphous ^{3}He having the temperature independent term of heat capacity or magnetic susceptibility described as Eq.(2.6) [17, 25, 39]. Morishita *et al.* reported that the temperature dependence of the amorphous ^{3}He from heat capacity measurements of the liquid phases of the 1st and 2nd (^{3}He/^{3}He/gr) layers on Grafoil [41, 44]. They also reported that the amorphous ^{3}He has the layer structure. Sato *et al.* measured the 1st ^{3}He layer on Grafoil at very low densities ($\rho < 2$ nm^{-2}, Fig.2.14(a)) and they directly observed the amorphous heat capacity [23]. The heat capacity data up to 0.45 nm^{-2} slightly decrease with increasing temperature but have no feature characteristic to the Fermi liquid ($C \propto T$). The weak T dependence of the heat capacity is roughly consistent with the Golov-Pobell model. Sato *et al.* assumed that the heat capacity at 0.45 nm^{-2} is a typical behavior of the amorphous ^{3}He, and demonstrated that the total heat capacity of ^{3}He monolayer at $\rho < 2$ nm^{-2} is well fitted to

$$C(T) = \gamma T - \alpha T^2 + \beta C_{0.45}(T). \tag{2.7}$$

Therefore, the heat capacity of ^{3}He adsorbed on the flat surfaces of the substrate can be extracted when the amorphous contribution is properly evaluated and subtracted from the total heat capacity. Figure 2.14 (b) and (c) show the density dependence of the amorphous and 2D liquid ^{3}He contributions. These figures indicate that the amorphous ^{3}He component grows prior to ^{3}He on the flat surfaces and is almost density independent after the growth is completed at 0.6 nm^{-2}. Low density ^{3}He submonolayer in ^{3}He/^{4}He/gr system is also studied [23]. This system does not show the amorphous heat capacity unlike ^{3}He/gr or ^{3}He/^{3}He/gr systems [41, 44]. The absence of the amorphous component is thought to be because ^{4}He, instead of ^{3}He, is adsorbed on the surface heterogeneities. The heat capacity and magnetization measurements on ^{3}He/HD/HD/gr display the contribution from the amorphous ^{3}He [17, 18, 39], which means that HD do not reduce the surface heterogeneities unlike ^{4}He. The density dependence of the amorphous amount of ^{3}He/HD/HD/gr system is estimated from the fitting assuming Eqs.(2.5) and (2.6). The susceptibility measurements [17] indicated that approximately 10 % of the total ^{3}He forms the amorphous solid whose amount has the weak density dependence. However, the heat capacity measurements [45] suggested that the amount of amorphous ^{3}He increases by a factor of ≈ 3 over the density range measured (1.0 – 5.0 nm^{-2}).

2.3 Frustrated nuclear magnetism of solid ^{3}He on graphite

2.3.1 Nuclear magnetism of bulk solid ^{3}He

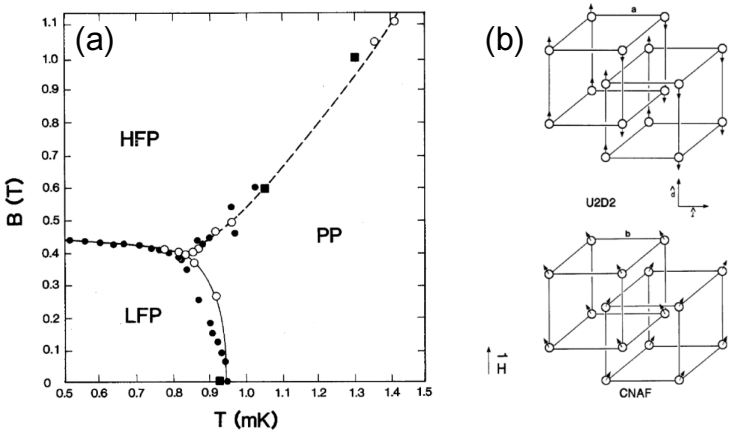

Fig. 2.15: (a) Magnetic phase diagram of bulk ^{3}He of molar volume V = 24.2 cc/mol. PP, LFP, and HFP are the paramagnetic, low field, and high field phases respectively. The filled circles are from the NMR measurements (Ref.[46]), the open circles from the melting pressure measurements (Ref.[47]), and the filled squares from the heat capacity measurements(Ref.[48]). (b) Spin lattice structure of the U2D2 and CNAF phases, correspond to the LFP and HFP respectively(Ref.[49]).

As mentioned in Sec.2.1, the atomic exchanges among ^{3}He atoms occur even in the

solid phase. The typical exchange frequency is of the order of 10^7 Hz which is far smaller than the Debye frequency of the order of 10^{11} Hz. This atomic exchanges cause the interactions between the nuclear spins of ^{3}He atoms. The nuclear spin system of the solid ^{3}He has the unique magnetism which cannot be explained by the simple Heisenberg model

$$H = J \sum_{<i,j>} \mathbf{S}_i \cdot \mathbf{S}_i, \tag{2.8}$$

where $\sum_{<i,j>}$ is the sum of the nearest neighbor spin pairs.

Figure 2.15 shows the magnetic phase diagram of the b.c.c. solid ^{3}He of the molar volume $V = 24.2$ cc/mol [49]. In zero magnetic field the phase transition between the high T paramagnetic phase (PP) and the low T antiferromagnetically ordered phase (LFP) occur at $T \approx 1$ mK. The transition is the first order [50], which is against the Heisenberg model which predicts the second order phase transition. The LFP is not the antiferromagnetic state with two simple cubic sublattices predicted by the Heisenberg model. The NMR measurements on the single crystal b.c.c. ^{3}He by Osheroff *et al.* show the large zero field resonance frequency of ≈ 780 kHz [49]. It is the evidence of lacking the cubic symmetry in the LFP. The high field phase (HFP) is not expected from the Heisenberg model, neither. The spin structures of the LFP and HFP is known as the U2D2 and CNAF (Canted Normal AntiFerromagnetic) state as shown in Fig.2.15(b).

The key to the unique nuclear magnetism of the bulk solid ^{3}He is the Multiple Spin Exchange (MSE) interactions [51, 52]. Because the zero-point motion of a ^{3}He atom is quite large, the interatomic exchanges occur even in the solid phase. When two atoms exchange, the hard core potential between ^{3}He atoms inevitably pushes out the surrounding atoms from their equilibrium positions. The effect on the surrounding atoms can be reduced by the cyclic exchange among three or more atoms at a same time. The MSE Hamiltonian is expressed as follows;

$$H = -\sum_n J_n (-1)^n P_n \tag{2.9}$$

where J_n (> 0) is the exchange interaction of the n-th order, P_n is the permutation operator of n spins. Even number permutations favor antiferromagnetism and odd number permutations ferromagnetism. Competence among the MSE interactions cause strong magnetic frustration resulting in the fascinating nuclear magnetism of ^{3}He.

2.3.2 Multiple spin exchange in 2D

The MSE interactions are important not only for the bulk solid ^{3}He but also the solid ^{3}He monolayer.

Figure 2.16 shows the PIMC (Path Integral Monte Carlo) calculation of each J_n of the 2D ^{3}He system as a function of areal density ρ [53], up to the 6th order. In this calculation the substrate potential is ignored. Each J_n has strong ρ dependence and decreases exponentially with the density. The Grüneisen constant $\alpha_{\rm P}$ of each MSE parameter is different. Basically the higher order exchange has the larger exponent, but J_3, not J_2, has the smallest exponent. This means that at higher density J_3 is dominant and therefore the ferromagnetic nature is stronger. On the other hand, at lower density the competition among MSE interactions are enhanced and the system is strongly frustrated.

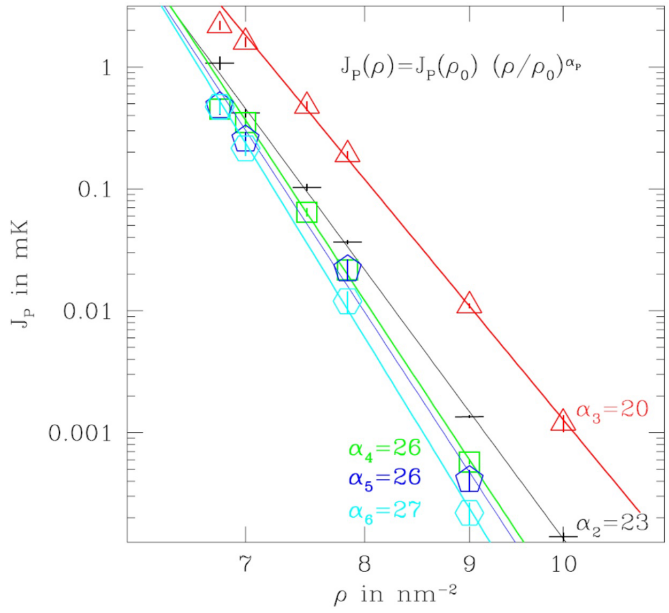

Fig. 2.16: Density dependence of the MSE interactions J_n of the 2D ^{3}He system from the PIMC calculation (Ref.[53]). These parameters changes exponentially with ρ, but the exponents α_P are different. At low densities the system is highly frustrated, but at high density J_3 becomes dominant because of the smallest α_P.

To obtain the MSE parameters from the experimental results, the high temperature series expansion (HTSE) analysis is useful. Roger calculated the HTSE parameters for the logarithm of partition function $\ln(Z)$ with the MSE Hamiltonian including up to the six-particle exchange term [54]. The partition function $\ln(Z)$ is expressed as

$$\frac{\ln(Z)}{N} = \sum a_{n,\lambda,\mu,\nu} \left[\frac{J}{2}\right]^{n-\lambda-\mu-\nu} \left[\frac{J_4}{8}\right]^{\lambda} \left[\frac{J_5}{16}\right]^{\mu} \left[\frac{J_6}{32}\right]^{\nu} \frac{\beta^n}{n!}, \tag{2.10}$$

where $J = J_2 - 2J_3$ is an effective two spin exchange. He calculated $a_{n,\lambda,\mu,\nu}$ up to the fifth order and $a_{n,\lambda,0,\nu}$ up to the sixth order. The HTSE of heat capacity is deduced from Eq.(2.10) the following relations,

$$\begin{aligned} C &= -T\frac{\partial}{\partial T}\left(\frac{\partial F}{\partial T}\right) \\ &= -T\frac{\partial}{\partial T}\left[\frac{\partial}{\partial T}\{-T\ln(Z)\}\right]. \end{aligned} \tag{2.11}$$

The leading terms of the HTSE of the heat capacity and magnetic susceptibility are written as

$$C = \frac{9}{4}Nk_B\left(\frac{J_C}{T}\right)^2, \tag{2.12}$$

$$\chi = \frac{c}{T-\theta} \approx \frac{c\theta}{T}, \frac{3cJ_\chi}{T} \tag{2.13}$$

$$J_\chi = \theta/3, \tag{2.14}$$

where N is the number of spins, k_B is the Boltzmann constant, c is the Curie constant, and θ is the Curie-Weiss temperature. The expressions of J_C and J_χ by J_n are as follows

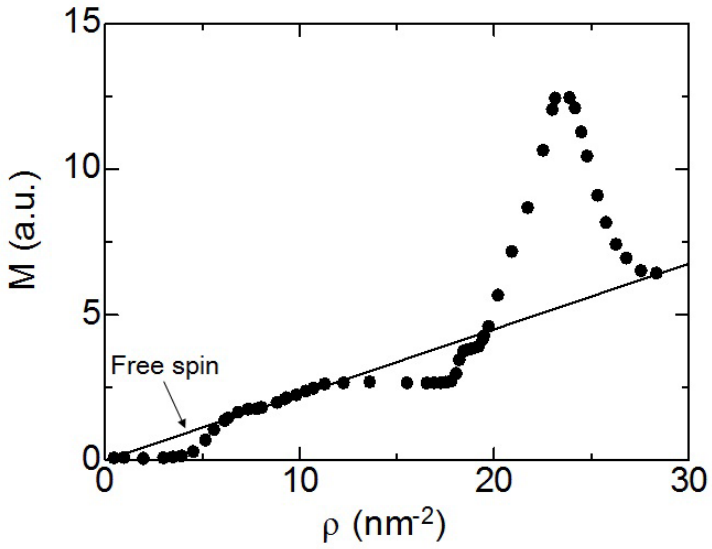

Fig. 2.17: Density dependence of the magnetization M of the ^{3}He film on graphite at $T = 4.6$ mK (Ref.[56]). The promotion to the 2nd layer occur at $\rho = 10.9$ nm^{-2}. The solid line is M of free spins. At $11 \lesssim \rho \lesssim 17$ nm^{-2} M is a constant because the 2nd layer ^{3}He is in the liquid. A narrow plateau around the C2 phase ($\rho \approx 18$ nm^{-2}) below the solid line means that the interactions are antiferromagnetic. At higher density M steeply increases, and the interactions become ferromagnetic.

[55]

$$J_{\rm C} = \left(J + \frac{5}{2}J_4 - \frac{7}{2}J_5 + \frac{1}{4}J_6\right)^2 + 2\left(J_4 - 2J_5 + \frac{1}{16}J_6\right)^2 + \frac{23}{8}J_5^2 - J_5J_6 + \frac{359}{384}J_6^2 \quad (2.15)$$

$$J_\chi = J + 3J_4 - 5J_5 + \frac{5}{8}J_6. \quad (2.16)$$

2.3.3 previous experiments

Density variation of magnetization

Figure 2.17 shows the magnetization M of a ^{3}He film on graphite at $T = 4.6$ mK as a function of the total ^{3}He density [56]. The promotion to the 2nd layer occurs at $\rho = 10.9$ nm^{-2}. M is independent of the density at $11 < \rho < 17$ nm $^{-2}$, because the 2nd layer ^{3}He is in the Fermi liquid phase. Slightly below the C2 density ($\rho = 17.8$ nm^{-2}), M increases and there is a narrow plateau around $\rho = 18$ nm^{-2}. Here M is still smaller than the expected value for free spins, shown as the solid line in Fig.2.17, and therefore the interactions are antiferromagnetic. At $\rho \gtrsim 19$ nm^{-2} M increases drastically and shows a ferromagnetic peak. In this density range the ^{3}He film is in the IC2 phase. The density dependence of M is qualitatively consistent with the theoretical calculation mentioned above, which predicts the ferromagnetic nature is stronger at higher densities [53].

IC2 phase

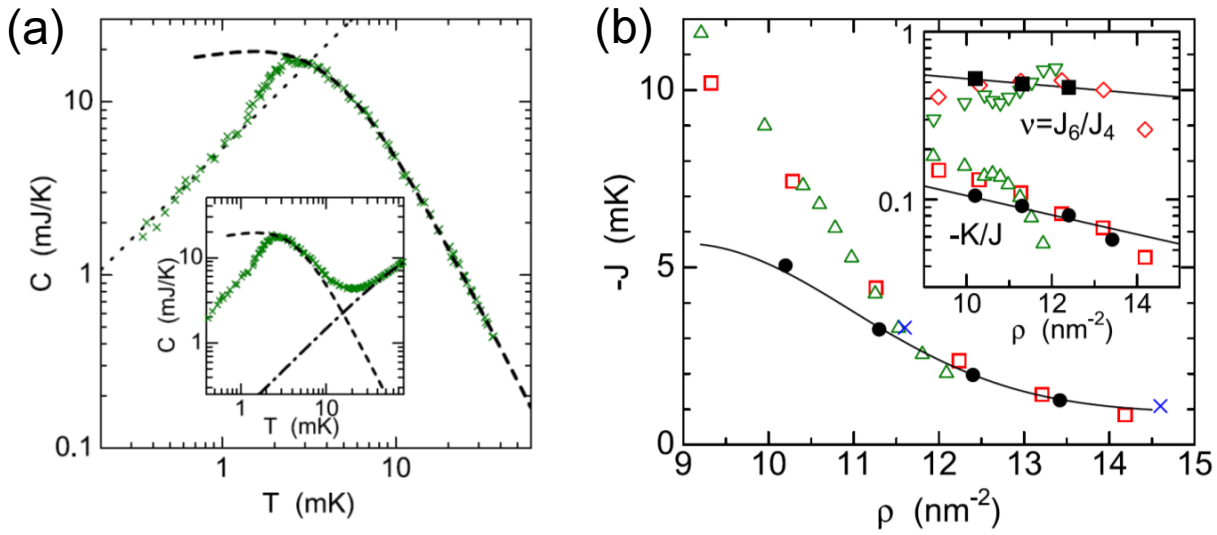

Fig. 2.18: (a) The magnetic heat capacity data of the IC2 solid ^{3}He on ^{4}He plated Grafoil at $\rho = 11.30$ nm^{-2}, after subtracting the overlayer liquid contribution shown as the dashed-dotted line in the inset (Ref.[37]). At $T \ll T_{\rm peak}$ the data follow $C \propto T$ (the dotted line), indicating 2D ferromagnetic spin wave excitations. The dashed line is the HTSE fitting of the MSE hamiltonian. (b) An effective two spin exchange $J = J_2 - 2J_3$ as a function of the total ^{3}He density. The inset shows the higher order exchanges $K/J = (J_4 - 2J_5)/J$ and $\nu = J_6/J_4$. The filled circles are deduced from the heat capacity data of ^{3}He/^{4}He/gr [37]. The crosses (Ref.[6]) and the open squares/diamonds (Ref.[57]) are from the heat capacity data of ^{3}He/^{3}He/gr. The open triangles (Ref.[57]) are from the magnetic susceptibility data of ^{3}He/^{3}He/gr.

The specific heat measurements of the IC2 phases in ^{3}He/^{3}He/gr [6, 57] and ^{3}He/^{4}He/gr [37, 58] are quantitatively consistent with the PIMC calculation of the MSE model [53]. Fig.2.18 (a) shows the magnetic heat capacity of the IC2 phase at $\rho = 11.30$ nm^{-2} on Grafoil preplated with a ^{4}He monolayer of 12.0 nm^{-2}. There is the third layer liquid ^{3}He, but its contribution is already subtracted. The total heat capacity is shown in the inset of Fig.2.18 (a). The $C \propto T$ behavior, guided by the dotted line in Fig.2.18(a), at $T \ll T_{\rm peak}$ is consistent with 2D ferromagnetic spin wave excitation. The MSE parameters deduced from the HTSE fitting of the heat capacity data (the dashed line in Fig2.18(a)) are shown in Fig.2.18(b). Here, $J = J_2 - 2J_3$ is the effective two particle exchange. The higher order MSE parameters, $K/J = (J_4 - 2J_5)/J$ and $\nu = J_6/J_4$, are also shown in the inset of Fig.2.18 (b). As the density increases J_4, J_5, and J_6 decrease faster than J. Therefore finally the effect of J is dominant and J is negative (ferromagnetic interactions). As the density increase, the temperature dependence of the heat capacity of the IC2 phase is similar to that of Heisenberg model with ferromagnet interactions on a Triangular lattice (HFT model) [58]. This similarity indicates that the IC2 phase is hardly affected by potential corrugation of the 1st layer. The Grüneisen parameter α of each J_n deduced

from the experimental data [58] agrees well with the value predicted by the MSE model ignoring the substrate potential [53].

C2 phase

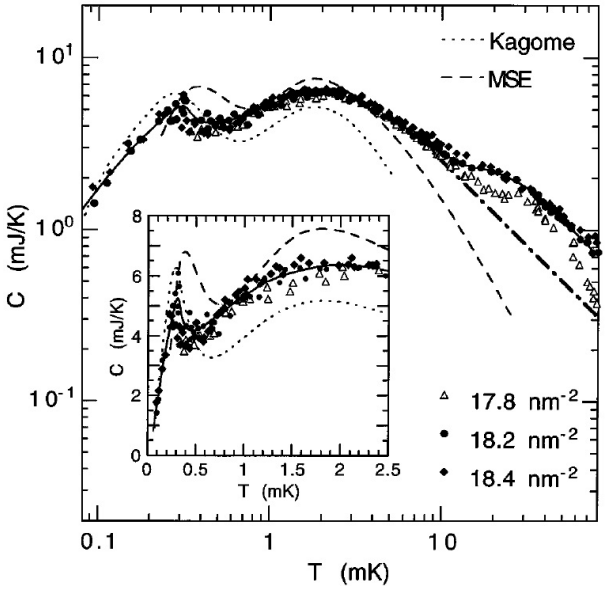

Fig. 2.19: Magnetic heat capacity of bilayer ^{3}He films at densities near the C2 phase (Ref.[6]). The total areal densities are given in the figure. A characteristic broad double-peak structure is observed; a high-T peak around $T = 1.8$ mK, and a low-T peak around 0.3 mK. Below the low-T peak the heat capacity is proportional to T.

In the C2 phase, the total exchange interactions are antiferromagnetic as shown in Fig.2.17. Due to the low density, this phase is expected to have the strongly magnetic frustration. Nuclear spin system of the C2 phase actually displays anomalous magnetic properties.

The heat capacities of the C2 phase of ^{3}He/^{3}He/gr have a characteristic broad double peak structure [6]. A rounded high-T peak at around 1.8 mK indicates short range spin ordering. At $T \approx 0.3$ mK the low-T peak appears. Below the low-T peak, the heat capacity decreases and the temperature dependence seems to satisfy $C \propto T$ down to 90 μK. This behavior indicates the gapless elementary excitations. The C2 phase of ^{3}He/^{3}He/gr also has the heat capacity with the double peak structure [20, 36]. These features are totally inconsistent with the Heisenberg model with antiferromagnetic interactions on a triangular lattice (HAFT model) which predicts the $C \propto T^2$ behavior at low T and a broad single peak [59]. The heat capacity of the solid ^{3}He monolayer of the ^{3}He/HD/HD/gr system has a broad peak around $T = 5$ mK [18]. For this system, the double peak or $C \propto T$ behavior is not observed down to 0.8 mK.

The previous magnetization measurements on the C2 phase of ^{3}He/^{4}He/gr are shown in Fig.2.20 [7]. Above 10 mK, the data satisfied the Curie-Weiss law $M \propto T^{-1}$. The Curie-Weiss temperature θ was -0.9 mK. Below 10 mK the temperature dependence of

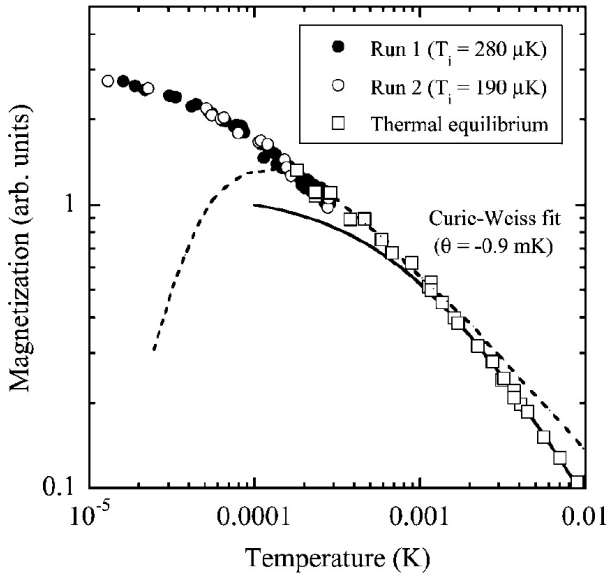

Fig. 2.20: Magnetization measurements on the ^{3}He monolayer in the C2 phase of the ^{3}He/^{4}He/gr system (Ref.[7]). There is no anomalies indicating finite-T magnetic phase transitions or a spin gap down to 10 μK. The solid line represents a Curie-Weiss behavior with the Weiss temperature of -0.9 mK. The dotted line is an expected behavior if the magnetic ground state has a spin gap of 80 μK (Ref.[60]).

M was weaker. No anomalies indicating finite temperature magnetic phase transition were observed down to $T/|\theta| \approx 0.01$. The data was clearly inconsistent with the behavior if the magnetic ground state has a spin gap of 80 μK, shown as the dotted line in Fig.2.20 [60]. The magnetization data of ^{3}He/HD/HD/gr, shown in Fig.2.21 also had no anomalies related to phase transition or a spin gap down to 10 μK [7, 17].

These experimental results strongly suggest that the magnetic ground state of the C2 phases is the QSL state with zero or an extremely small (< 10 μK) spin gap.

UUUD phase under magnetic field

Figure 2.22 shows the magnetization of the C2 phase of ^{3}He/^{4}He/gr as a function of the applied magnetic field parallel to the graphite substrate at $T = 0.7$ mK. Before M fully saturates at H_0 =10 T, a narrow plateau of $M = 1/2M_{\rm saturate}$ appears between 1.2 and 2.2 T. This 1/2 plateau is evidence of the UUUD phase. The structure of this phase is shown in Fig.2.22. The unit cell is an parallelogram in which three spins are up and one is down. The UUUD phase is predicted by two theories in the frame of the MSE model. One considers up to 4-spin exchanges [62] and the other considers up to 6-spin exchanges [61]. The experiment and theories are inconsistent in the width of the plateau and the saturation field. The difference is attributed to the difference in J_6.

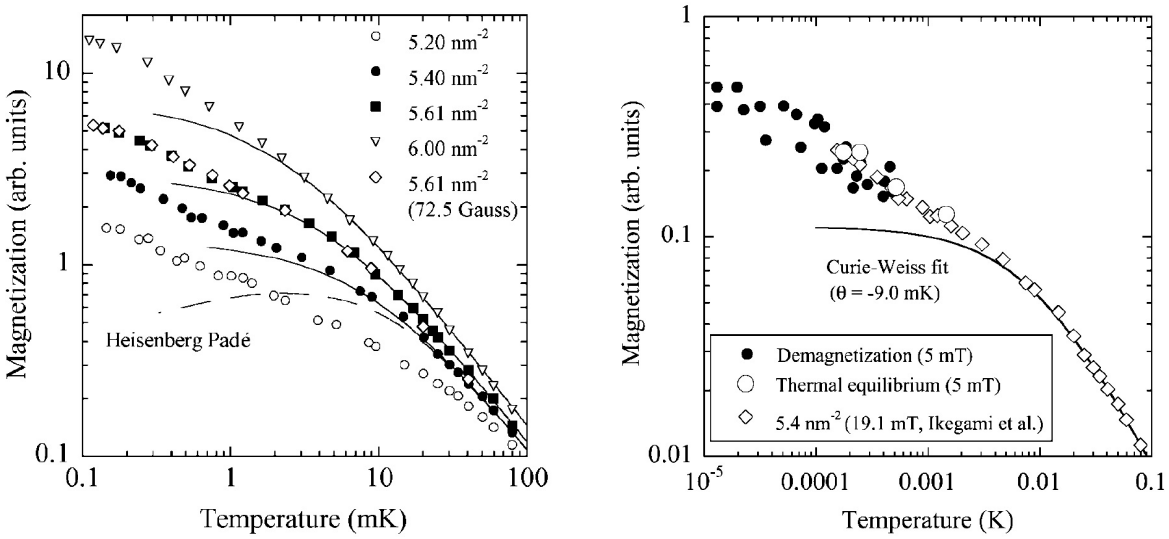

Fig. 2.21: Magnetization measurements on ^{3}He monolayers of the ^{3}He/HD/HD/gr system from Ref.[17] (left) and Ref.[7] (right).There is no anomalies indicating finite-T magnetic phase transitions or a spin gap were down to 10 μK.

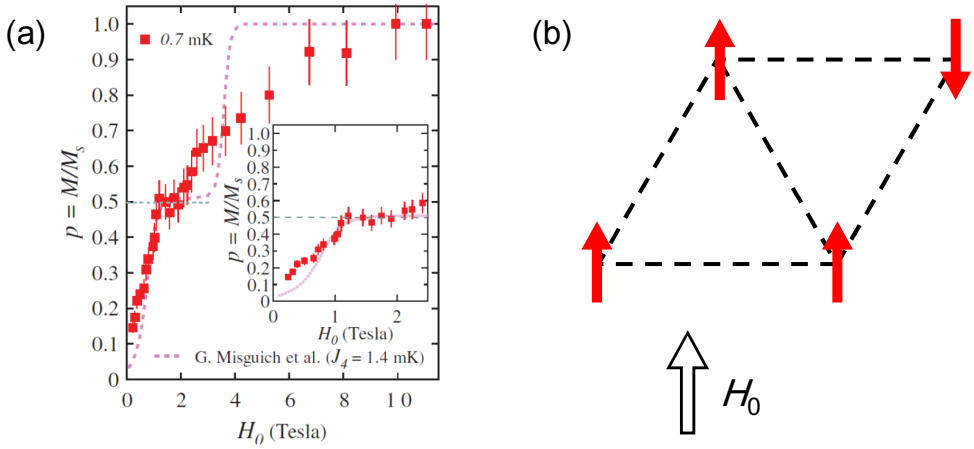

Fig. 2.22: (a) Magnetization curve of the C2 phase of ^{3}He/^{4}He/gr at 0.7 mK. The $M = 1/2$ plateau between 1.2 and 2.2 T is the evidence of the UUUD phase, predicted by the MSE model. The pink dotted line is the theoretical calculation of the MSE model considering up to 6-particle exchange [61]. (b) Spin lattice structure of the UUUD phase. The white arrow indicates the direction of the external magnetic field.

Theories for the QSL state of the C2 phase

The exact diagonalization studies of MSE Hamiltonian up to six-spin exchanges by Misguich *et al.* predicts the QSL ground state [61, 63]. However, the QSL state predicted by these caoculations has a spin gap of the order of $J_4/2$, which contradicts the experimental observations of the C2 phase.

Motrunich *et al.* proposed another QSL state in their Variational Monte Carlo studies on the MSE hamiltonian with up to 4-spin exchanges assuming the antiferromagnetic effective 2-spin interactions [65]. They found the U(1) QSL state at $J_4/J_2 \gtrsim 0.14$. In this QSL state, fermionic spinons form a Fermi surface, and therefore have gapless excitations. This state has finite spin susceptibility at $T \to 0$, and has an unusual behavior of the specific heat satisfying $C \propto T^{2/3}$ because the spinons are coupled to the U(1) gauge field. However, this QSL state does not explain the properties of the C2 phase.

Though the MSE interactions are essentially important to understand the nuclear magnetism of ^{3}He monolayer systems, as seen in the IC phase and UUUD phase in the magnetic field, the magnetism of the C2 phase is not fully explained by the MSE model. In order to overcome the disagreement, some theories consider not only the MSE interactions but also some additional effects. For example, the bond inequality of the 4/7 structure [66], the hole doping (t-J-K model) [67], or the layer promotion [68]. Another possible effect is the lattice disorder of the C2 phase, if it is not the solid but the QLC state with partially broken symmetry (see Sec.2.2.2). The effect of the lattice imperfection may explain the discrepancy. For example, an exact diagonalization study on the HAFT model with randomness in exchange interactions J yields the QSL state having T-linear specific heat [69]. This calculation assumed that the bond-independent uniform distribution in the nearest neighbor couplings in $[(1-\Delta)J, (1+\Delta)J]$, .

2.4 Normal Fermi liquid phase of ^{3}He monolayer on graphite

2.4.1 Landau Fermi liquid in two dimensions

A low density ^{3}He submonolayer adsorbed on graphite is well described by the 2D Fermi liquid theory. In the noninteracting Fermi gas, the heat capacity below the Fermi temperature $T_{\rm F}$ follows,

$$C = \frac{\partial E}{\partial T} = \frac{\pi^2}{3} D k_{\rm B}^2 T, \tag{2.17}$$

where D is the density of state. In the case of the 2D free fermion system, D is expressed as $D = mA/\pi\hbar^2$, where m is mass of a particle and A is the system surface area. Therefore D is independent of the number of the particles. The heat capacity of the 2D free fermion system is written as

$$C = \frac{\pi k_{\rm B}^2 mA}{3\hbar^2} T \equiv \gamma_0 T, \tag{2.18}$$

where γ_0 is called the Sommerfeld constant, and $T_{\rm F}$ is,

$$T_F(K) = \frac{\pi\hbar^2}{mk_B}\rho = 0.504\rho \quad (\mathrm{nm}^{-2}). \tag{2.19}$$

In the Landau Fermi liquid theory, the interatomic exchange interactions are added to the degenerate Fermi gas in adiabatic conditions. The elementary excitations of the Fermi liquid are called quasiparticles. The number of the quasiparticles and that of the bare particles have one to one correspondence. The effect of the interaction is expressed as the enhancement of the quasiparticle effective mass m^*. The Fermi temperature is modified to be

$$T_F^* = \frac{\pi\hbar^2}{m^* k_B}\rho = \frac{m}{m^*} T_F, \tag{2.20}$$

and the heat capacity at $T \ll T_{\rm F}^*$ is,

$$C(T) = \gamma T, \quad \gamma = \frac{\pi k_B^2 m^* A}{3\hbar^2} = \frac{m^*}{m}\gamma_0. \tag{2.21}$$

The heat capacity of the 2D Fermi liquid is determined by two parameters, that is, the effective mass enhancement m^*/m and the surface area A. Experimentally, the heat capacity of the ^{3}He layer in the Fermi liquid phase is known to follow

$$C(T)_{\rm FL} = \gamma T - \alpha T^2, \tag{2.22}$$

where the T^2 term comes from the spin fluctuations [70].

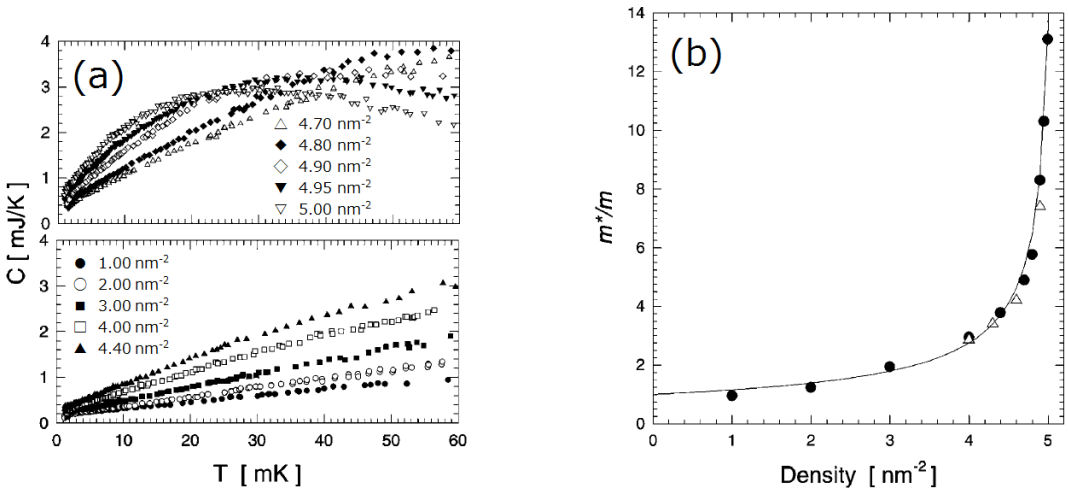

Fig. 2.23: (a): Heat capacities data of the Fermi liquid phase in ^{3}He monolayers on a bilayer of HD (Ref.[39]). They satisfy $C \propto T$ at low T. The slope is enhanced at higher densities. (b): The effective mass enhancement of ^{3}He quasiparticles m^*/m as a function of the density. The closed and open circles are from the heat capacity magnetization measurements assuming the Landau parameter F_a^0 of $-3/4$, respectively. The m^*/m tends to diverge towards the critical density $\rho_c = 5.1$ nm^{-2}.

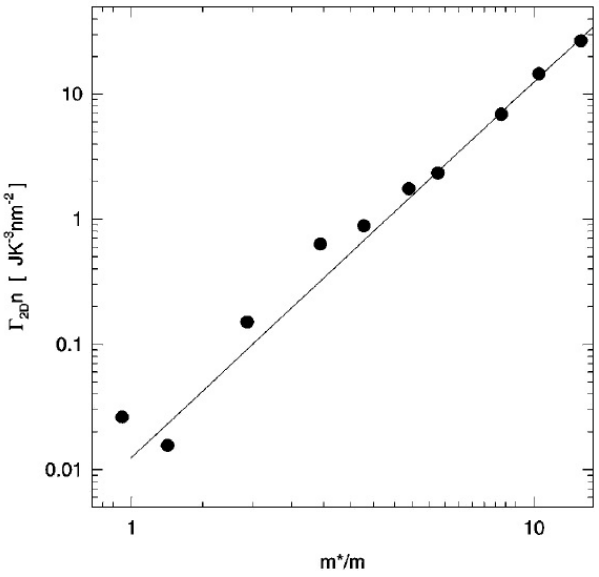

Fig. 2.24: $\Gamma_{2D}n$ vs. m^*/m, where Γ_{2D} is the coefficient of T^2 term of the heat capacity (Ref.[39]), and n is the areal density. Note that n and Γ_{2D} are denoted by ρ and α in the present thesis, respectively. The solid line is a relation $\Gamma_{2D}n \propto (m^*/m)^3$ which is expected from the Mott Hubbard transition there.

2.4.2 Previous experiments

Previous heat capacity measurements of ^{3}He/HD/HD/gr by Casey *et al.* observed a $C \propto T$ dependence at $\rho \leq 5.$ nm^{-2}. The behavior is characteristic to the Fermi liquid (Fig.2.23 (a))[39]. If the Fermi liquid covers the whole surface of the substrate, A is constant and γ is simply proportional to the effective mass enhancement m^*/m. As shown in Fig.2.23 (b), the increase of m^*/m with increasing density was observed by the heat capacity and magnetization measurements [39]. The value of m^*/m cannot be deduced by the magnetization data only because the magnetization is determined not only by m^*/m but also an antisymmetric Landau parameter of zeroth order F_0^a. They assumed the almost localized model [71] which gives $F_0^a = -3/4$ to calculate m^*/m. The maximum mass enhancement observed in the study was $m^*/m = 13$ at $\rho = 5.0$ nm^{-2}. The critical density of $\rho_c = 5.1$ nm^{-2} was obtained by fitting the data to

$$\frac{m^*}{m} = \left(1 - \frac{\rho}{\rho_c}\right)^{-\nu} \tag{2.23}$$

where ν is the critical exponent. The critical behavior of a α coefficient of T^2 term was observed as well [39]. Equation (2.22) can be expressed using Eq.(2.21) as follows

$$C = \frac{1}{3}\pi^2 N_3 k_{\mathrm{B}} \left(\frac{T}{T_{\mathrm{F}}^*} - \eta \left(\frac{T}{T_{\mathrm{F}}^*} \right)^2 \right), \tag{2.24}$$

where η is a dimensionless parameter related to α in the following way

$$\alpha\rho \propto \left(\frac{m^*}{m}\right)^2 A\eta. \tag{2.25}$$

Figure 2.24 shows that $\alpha\rho$ is proportional to $(m^*/m)^3$. The coefficient of T^2 term $\Gamma_{2\mathrm{D}}$ and the density n in the figure correspond to α and ρ in this thesis, respectively. They introduced a characteristic temperature

$$T_0 = \frac{T_F^*}{\eta}, \tag{2.26}$$

below which the Fermi liquid is well defined. Their results correspond to $T_0 \propto T_F^{*2} \propto (m^*/m)^{-2}$. If solidification of the Fermi liquid is modeled by the filling control metal-insulator transition, and the commensurate phase can be considered to be the Mott localized state, the "doping" δ is written as $\delta = (1 - \rho/\rho_c)$, where ρ_c is the density of the commensurate phase. In the critical behaviors of the filling controlled metal-insulator transition are given by Ref.[72] as

$$\gamma \propto \frac{m^*}{m} \propto \delta^{(d-z)/d} \tag{2.27}$$

$$T_0 \propto \delta^{z/d}, \tag{2.28}$$

where z is the critical exponent and d is the dimension of the system. In the case of ^{3}He monolayers, of course, $d = 2$. Their data imply $\gamma \propto \delta^{-1}$ and $T_0 \propto (m^*/m)^{-2} \propto \delta^2$. These are correspond to $z = 4$ and the value satisfies the Mott transition regime $z > 2$.

2.5 Self-condensation of low density liquid ^{3}He monolayers

Even after Kamerlingh Onnes successfully liquified ^{4}He, ^{3}He had long been thought to be a permanent gas which cannot be liquefied at $T = 0$, because the lighter mass and Pauli principle enhance the kinetic energy which prevent the system from liquefaction. However, in 1949 the condensation of ^{3}He was discovered [73]. Then, how about ^{3}He in 2D? By lowering the dimension the coordination number decreases. This reduces the energy gain from the potentials by surrounding atoms and prevent liquefaction further. A variational Monte Carlo study by Miller found that 2D ^{4}He can be liquefied but 2D ^{3}He cannot be [74]. A diffusion Monte Carlo study by Grau also concluded that 2D ^{3}He cannot condense even though 2D mass-3 bosons does condense[75].

Despite these negative theoretical predictions, experimental evidence of condensation of the ^{3}He monolayer was first reported in 1982. Bhattcharyya *et al.* measured the heat capacity of ^{3}He submonolayers on a superfluid ^{4}He thin film of 10 Å and 12.3 Å thickness adsrobed on a nuclepole substrate [76]. In the very low density region ($x = \rho/6.4\ \mathrm{nm}^{-2} \leq 0.163$), the $C = \gamma T$ dependence was observed below 100 – 120 mK and the γ coefficient was smaller than γ_0, the value of the degenerated Fermi gas. Since the γ coefficient is determined by two parameters m^*/m and A, as discussed in Sec.2.4, and the effective mass enhancement m^*/m cannot be less than unity, $\gamma < \gamma_0$ is explained exclusively by the reduction of the surface area A. Therefore this is clear evidence of the self-condensed liquid (liquid puddle).

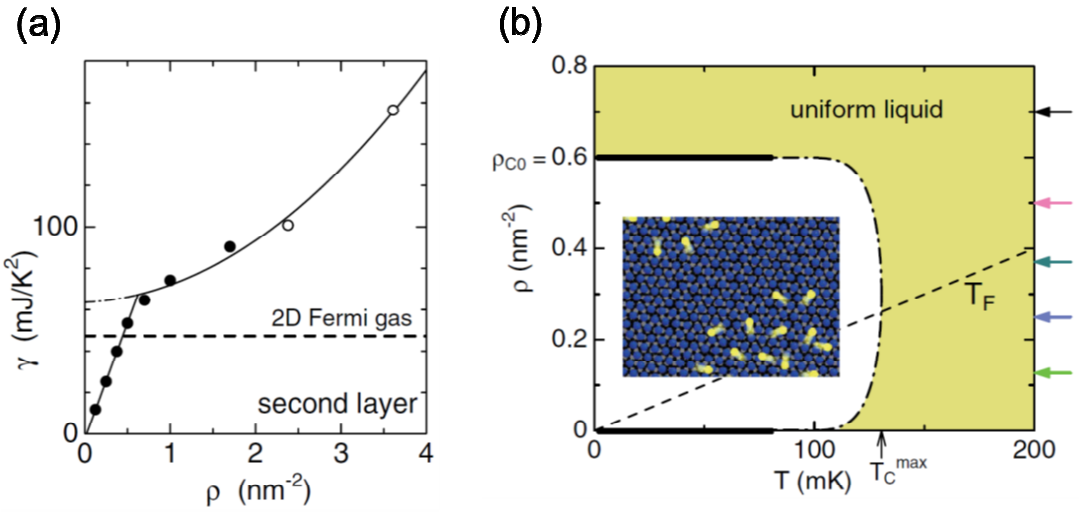

Fig. 2.25: (a) Areal density dependence of a γ coefficient of the ^{3}He/^{4}He/gr system[23]. Below a clear kink is at $\rho \approx 0.6\ \mathrm{nm}^{-2}$, γ become smaller than γ_0. (b) Phase diagram of ^{3}He/^{4}He/gr in the lowest density region. The dashed line represents the Fermi temperature calculated by Eq.(2.19). The inset shows the schematic picture of the self-condensed liquid.

Recent experiments on ^{3}He monoatomic layers on (plated) Grafoil substrate also demonstrated the liquid puddle formation. Sato *et al.* measured heat capacities of low

density ($\rho < 1$ nm^{-2}) ^{3}He submonolayers for three different systems (^{3}He/gr, ^{3}He/^{4}He/gr, and ^{3}He/^{3}He/^{4}He/gr) and observed the self-condensed liquid for all of these systems. The density dependence of the γ coefficient of ^{3}He/^{4}He/gr, shown in Fig.2.25, had a clear kink at $\rho \approx 0.6$ nm^{-2}. Below this critical density the γ coefficient changed linearly with the density and was smaller than γ_0. This was clear evidence of the self-condensed liquid. The γ coefficients of ^{3}He/gr and ^{3}He/^{3}He/^{4}He/gr also displayed the similar behavior and, despite large difference in the potential corrugations from the underlayers, the critical densities are very similar: 0.8 nm^{-2} for ^{3}He/gr and 0.9 nm^{-2} for ^{3}He/^{3}He/^{4}He/gr. Therefore Sato *et al.* concluded that the self-condensed liquid is the intrinsic property of 2D ^{3}He and is not stabilized by the potential from the underlayer.

Rrecent Quantum Monte Carlo studies, however, indicated that the potential from the underlayers, especially its corrugations, plays an crucial role to stabilize the self-condensed liquid of the ^{3}He monolayers [77, 78]. In the case of ^{3}He/^{4}He/gr, the energy per particle has a minimum value at 0.7 nm^{-2} when the realistic potential from a monolayer of ^{4}He and graphite are taken into account. However, when one assumes the laterally averaged potential there is no energy minimum at finite density potential [77, 79]. Calculations for ^{3}He/gr with the corrugated potential also predicts the gas-liquid (G-L) transition, but it disagree with the experimental results in the density range. The experimental results observed the G-L transition from zero density, while the theory predicted the transition from 0.6 nm^{-2}. The effect of the substrate potential on stabilizing the self-condensed liquid is yet fully understood.

2.6 Quantum spin liquid candidates in electronic spin systems

2.6.1 Quantum spin liquid

Spin systems usually become ordered states as the ground states. The kind of order depends on the structures and interactions of the systems. However, if there are competing interactions the formation of order is prevented. This situation is called the magnetic frustration. One of the simplest example of the magnetic frustration is Ising spins with the antiferromagnetic nearest neighbor interactions on three vertices of a triangle. When one spin is in the up state, another spin favors the down state due to the antiferromagnetic interactions. However, The antiferromagnetic interaction cannot be fully satisfied no matter which state the other spin choose. Similar to the example above, many frustrated spin systems have triangular lattices or lattices based on triangles, such as the kagome or pyrochlore lattices. The geometry is not the only factor which gives the magnetic frustration to the spin systems. For example, the next nearest neighbor interactions or the coexistence of both ferromagnetic and antiferromagnetic interactions.

Spin systems with very strong magnetic frustrations are expected to have the ground state without long range order. This state is named the quantum spin liquid (QSL) state, because the spins are not "frozen". Here, we define the QSL state in this thesis as the state which does not have the long range order or finite expectation value of a spin at each site at $T = 0$. The concept of the QSL was first proposed by Anderson in 1973 [80]. He claimed that the ground state of the HAFT model is the resonating valence bond (RVB)

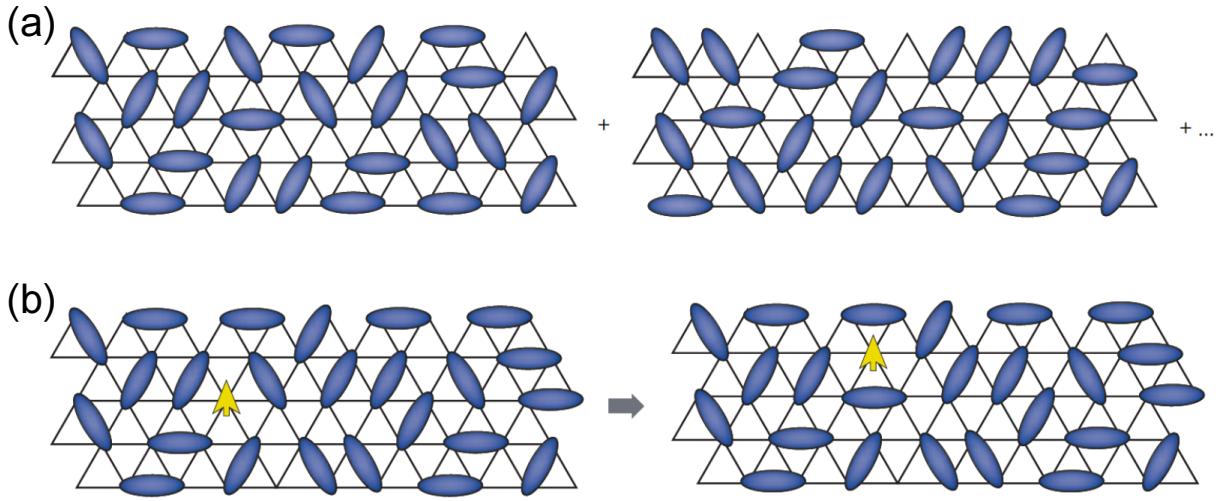

Fig. 2.26: (a) Schematic picture of a RVB state. In the two triangular lattices valence bonds (blue ovals) are distributed in different patterns. The RVB state is expressed by linear combinations of many different distributions, and does not break lattice symmetries. (b) A spinon excitation of in the RVB. A spinon is an unpaired spin moving in the sea of valence bonds.

state. A building block of a RVB state is a singlet pair $(1/\sqrt{2})(|\uparrow\downarrow\rangle - |\downarrow\uparrow\rangle)$ whose total spin is zero. There are numerous patterns of arranging singlet bonds on the lattice and all these patterns have the same energy. The ground state of this system is the linear combinations of all these arrangements of singlet bonds. In this state, there is no long range magnetic order. A schematic picture of the RVB state is shown in Fig.2.26 (a). The results of the numerical studies on the HAFT model after Anderson did not agree with him and the ground state of the HAFT model is now believed to be the three-sublattice 120° Néel ordered state [81, 82]. However, the QSL state have been energetically studied through both theoretical and experimental approaches [83, 84]. The elementary excitations of the RVB ground state is thought to be spinons which are originally considered in the regime of the 1D spin liquid. A spinon is a decoupled free spin moving in the sea of resonating valence bonds as depicted in Fig.2.26 (b). Because spinons are generated by decoupling a singlet bond, two spinons must be excited at a same time. This elemental excitation carries a spin 1/2 but no charge.

A number of theoretical studies were conducted after Anderson, but the experimental realization of the QSL state had not been achieved for a long time. In 1997, the first experimental evidence of the QSL state was reported in heat capacity measurements on the nuclear spin system of the ^{3}He C2 phase [6]. In 2003, the QSL material of the electron spin system was reported in the NMR study on the layered organic Mott insulator κ-(BEDT-TTF)$_2$Cu$_2$(CN)$_2$ with the triangular lattice [85]. After these discoveries, a number of the QSL candidates have been reported and they have a variety of lattice structures such as a Kagome lattice [86, 87], 3D hyperkagome network [88], and a honeycomb lattice [89].

2.6.2 QSL candidates with triangular lattices

We introduce previous studies on the QSL materials focusing on the ones with triangular lattices. The first reported QSL candidate material with the 2D electron system is layerd organic Mott insulator κ-(BEDT-TTF)$_2$Cu$_2$(CN)$_2$. In this material, a dimer of BEDT-TTF (bis(ethylenedithio)-tetrathiafulvalene) molecules is regarded as one electron site and these dimers form $S = 1/2$ triangular lattice with small anisotropy. The NMR measurements displayed no magnetic phase transition down to 32 mK [85]. Another QSL candidate material with similar structure is EtMe$_3$Sb[Pd(dmit)$_2$]$_2$. This material also shows no sign of magnetic ordering or phase transition down to 19.4 mK [90]. Both materials have the T-linear specific heat as shown in the left panel of Fig.2.27, indicating gapless excitations. From the NMR and specific heat results, one can calculate the Wilson ratio $R_{\rm W}$ expressed as

$$R_{\rm W} = \frac{\chi/\chi_0}{C/C_0}, \tag{2.29}$$

where χ is the magnetic susceptibility and C is the specific heat. The subscript 0 means the value of the ideal Fermi gas. The values of κ-(BEDT-TTF)$_2$Cu$_2$ and EtMe$_3$Sb[Pd(dmit)$_2$]$_2$ are both close to unity, so elemental excitations (spinons) behave like electrons in normal metal. It is difficult for these materials to discuss the specific heat of the electron spins at low T limit because of a steep increase of the Schottky type contributions from Cu^{2+} nuclear spins. To avoid the effect of Cu^{2+} nuclear spins the thermal conductivity measurements were conducted. The results of these two materials were inconsistent as shown in the right panel of Fig.2.27. The specific heat of EtMe$_3$Sb[Pd(dmit)$_2$]$_2$ had the T-linear term but that of κ-(BEDT-TTF)$_2$Cu$_2$(CN)$_2$ did not. Therefore, it is believed that the QSL state of κ-(BEDT-TTF)$_2$Cu$_2$(CN)$_2$ has a small energy gap of $\Delta \approx 0.45$ K, and that of EtMe$_3$Sb[Pd(dmit)$_2$]$_2$ is gapless. Recently, another organic material κ-H$_3$(Cat-EDT-TTF)$_2$ was reported as the new QSL candidate [91]. From the SQUID and magnetic torque measurements the ground state of this material is the QSL with gapless excitations. Some inorganic materials with triangular lattices were also reported as good candidate of the QSL materials. For example, Ba$_3$CuSb$_2$O$_9$ has an isotropic triangular lattice of Cu^{2+} ions with $S = 1/2$, and the magnetic susceptibility and neutron scattering measurements did not observe spin ordering down to 0.2 K [94]. The specific heat of this material satisfied the $C \approx T$ dependence below 1.4 K, indicating gapless excitations.

YbMgGaO$_4$ was reported as a new QSL candidate [112]. In this material Yb^{3+} ions form the triangular lattice with no site mixing and no antisymmetric Dzyaloshinsky-Moriya interaction. Because the ground state of Yb^{3+} is a Kramers doublet and there is a large energy gap of 38 meV between the ground state and the first excited state, this magnet can be regarded as the spin system with $S = 1/2$. The heat capacity satisfied the power law behavior $C \propto T^{\nu}$ at $T < 2$ K. The power $\nu \approx 0.7$ under zero external field. This value is close to $\nu = 2/3$ expected for the U(1) spin liquid [65]. The spin entropy obtained by integrating the specific heat asymptote to $Nk_{\rm B} \ln 2$, unlike other QSL candidates having the residual entropy even at $T = 0$. The magnetic susceptibility satisfied $\chi \propto T^{-1/3}$ from 4 K down to 0.4 K, which is inconsistent with the T-independent behavior expected for the U(1) spin liquid, but the muon spin resonance measurements down to 0.048 K show the temperature-independent spin relaxation rate which is proportional to the dynamic

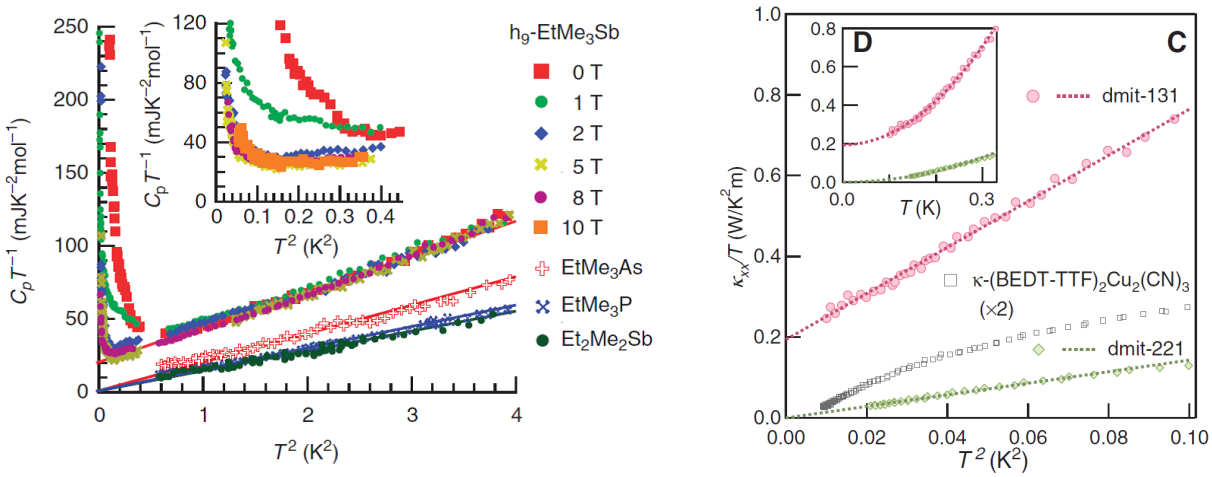

Fig. 2.27: left: Specific heat over the temperature C/T of $EtMe_3Sb[Pd(dmit)_2]_2$ (Ref.[92]), compared with that of $EtMe_3As[Pd(dmit)_2]_2$, $EtMe_3P[Pd(dmit)_2]_2$, and $Et_2Me_2Sb[Pd(dmit)_2]_2$. These three materials have the magnetically ordered ground state. The finite value of C/T at $T = 0$ means there is the T-linear term in the specific hear. right: Thermal conductivity over the temperature κ/T of $EtMe_3Sb[Pd(dmit)_2]_2$ (dmit-131), κ-$(BEDT\text{-}TTF)_2Cu_2(CN)_3$, and $Et_2Me_2Sb[Pd(dmit)_2]_2$ (dmit-221). The finite y-intercept of $EtMe_3Pd[Pd(dmit)_2]_2$ data indicates the T-linear term in the thermal conductivity, but the data of κ-$(BEDT\text{-}TTF)_2Cu_2(CN)_3$ and $Et_2Me_2Sb[Pd(dmit)_2]_2$ go to zero as $T \to 0$ [93]

correlation function of Yb^{3+}, at $T < 0.4$ K [95]. From these results, the ground state of this material is believed to be the U(1) spin liquid. What makes the magnetic frustration of $YbMgGaO_4$ stronger than the HAFT model is thought to be the next nearest neighbor interactions J_{NN} from the results of a neutron scattering measurements [96].

Chapter 3

Experimental apparatus and methods

In this chapter the experimental setup and heat capacity measurement techniques used in this study are described. The details are shown in Refs.[36, 97].

3.1 Nuclear demagnetization refrigerator

Figure 3.1 shows the schematic view of the whole setup of the refrigerator used in this study. This system can roughly be divided into three parts: a ^{3}He-^{4}He dilution refrigerator, a sample cell stage, and a Cu nuclear stage. For nuclear demagnetization refrigeration, 36 mol oxygen-free copper with a residual resistance ratio (RRR) of 5000 is used as the nuclear stage. Up to 8 Tesla can be applied to this nuclear stage by a superconducting magnet surrounding it. The lowest achievable temperature by demagnetization cooling is 51 μ K. The mixing chamber of the dilution refrigerator is thermally connected to the Cu nuclear stage via an Al superconducting heat switch (HSW), and the Cu stage and the sample cell stage are connected via a Zn superconducting HSW. The thermometers mounted on each stage are the following: a RuO_2 resistance thermometer (> 10 mK) on the mixing chamber, two Pt NMR thermometers (< 100 mK) on the nuclear stage and the sample cell stage, and a carbon resistance thermometer on the sample cell stage.

3.2 Thermometers

3.2.1 ^{3}He melting curve thermometer

The melting pressure of ^{3}He has a large temperature dependence below 1 K. A ^{3}He melting curve thermometer (MCT) is a thermometer that utilizes this relation for precise determination of the temperature. A mixture of solid and liquid ^{3}He is contained in a pressure cell and the pressure is measured by a capacitance diaphragm. We adopt the (T, P) relation proposed by Greywall [98] for calibration. There are four fixed points on the ^{3}He melting curve which can be used for pressure calibration for a MCT. In this study, the M point, a fixed point where the pressure reaches the minimum value, and the A point, a fixed point where normal liquid ^{3}He become a superfluid A phase, are used for

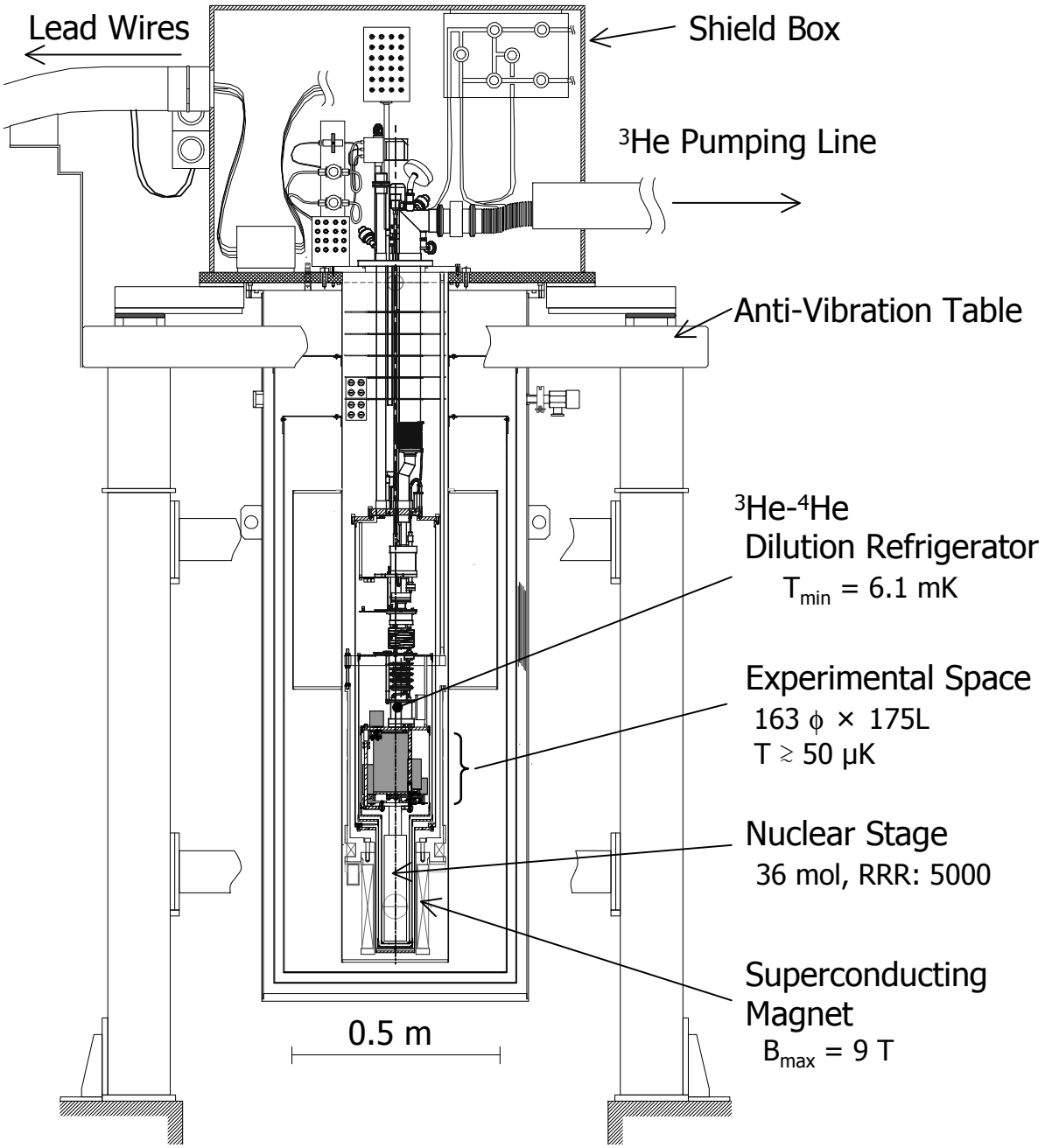

Fig. 3.1: Schematic view of the Cu nuclear adiabatic demagnetization refrigerator used in this work (Ref.[36])

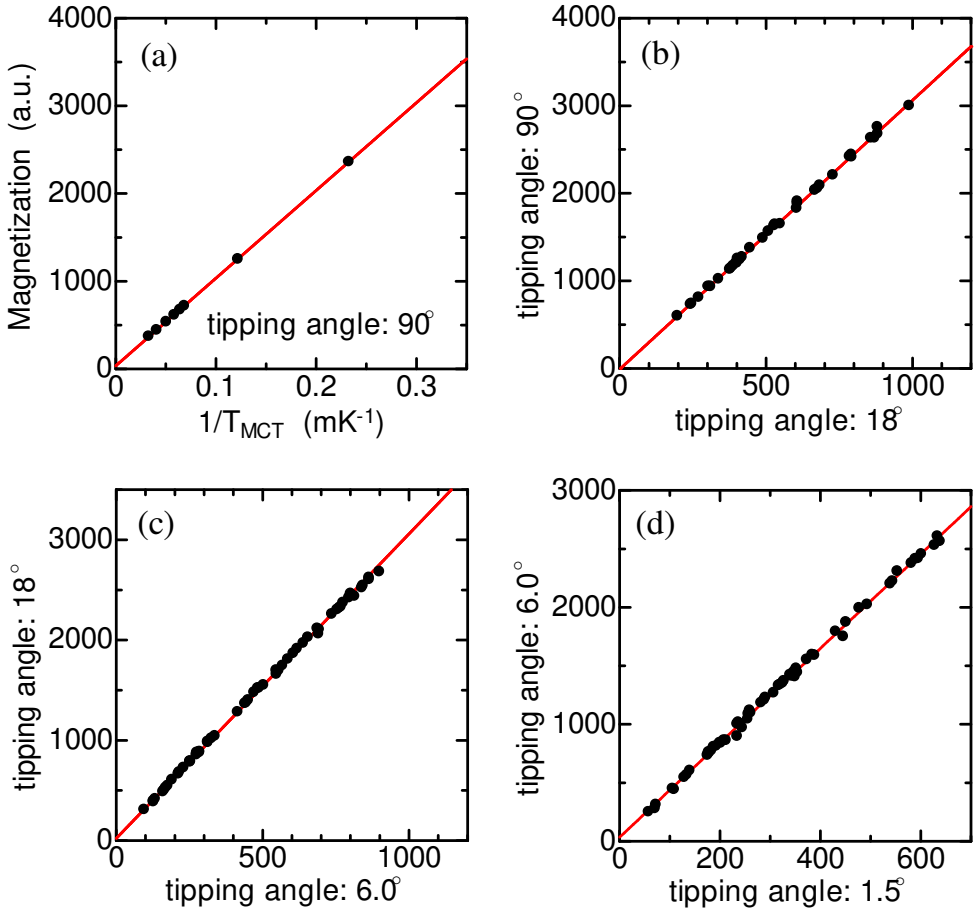

Fig. 3.2: Calibration of the Pt NMR thermometer which is thermally connected to the sample cell stage. (a) Calibration of the signal after a 90° pulse to a MCT. (b) (c) (d) Calibrations between signals after pulses of different tipping angles.

calibration.

3.2.2 Pt NMR thermometer

Nuclear magnetization of Pt^{195}, whose natural abundance is about 34 %, follows the Curie law well down to 10 μK so it can be used as a thermometer at ultra low temperature. As described in Sec.3.1, we have two Pt thermometers. One is mounted on the nuclear stage and the other on the sample cell stage. A Pt thermometer can be used from the lowest temperature of our refrigerator ($\leq$ 100 μK) to about 100 mK, but for heat capacity measurements this thermometer is used up to 30 mK because of the bad S/N ratio. Magnetization of Pt is measured by a pulsed NMR method. We adopted several different tipping angles for pulsed NMR measurements because the magnetization signal obtained by applying a 90° pulse is so large that a preamplifier is saturated. 90°, 7.2°, and 1.8° for the Pt thermometer on the nuclear stage, and 90°, 18°, 6°, and 1.5° for the Pt thermometer on the cell stage depending on the temperature of each stage. Tipping angles are controlled by changing the width of the rf pulse and a resonant frequency is

fixed at 250 kHz (H = 28.5 mT). The time interval between rf pulses τ must be large enough compared with the spin-lattice relaxation time T_1. T_1 can be derived from the Korringa relation $T_1 \cdot T = \kappa$, where κ is Korringa constant. In the case of Pt, κ = 30 s·mK. τ is chosen to be $\tau \approx 3T_1$ during heat capacity measurements by heat pulse method, and $\tau \approx 0.5T_1$ for the thermal relaxation method. Magnetization signals using 90° pulses are calibrated to the MCT, and signals after other tipping angles are calibrated to those after the larger tipping angle as shown in Fig.3.2. A typical value of a heat leak into the sample cell per one 90° pulse is ≈ 110 nJ. A heat leak per a pulse with another tipping angle θ_t can be estimated to be $\approx 110 \times \theta_t/90$ nJ.

3.2.3 Carbon resistance thermometer

We have a carbon resistance thermometer (CRT) on the sample cell stage, which is used for heat capacity measurements at $T > 17$ mK. This thermometer is also calibrated to the MCT. Resistance of the CRT shows a small jump of $\Delta T = 30\ \Omega$ at 53.6 mK. The jump of the resistance was reported in previous studies using the same experimental setup [58] It is probably because a material used in a part of electrodes become superconductive at this temperature. This jump is highly reproducible, so the calibration formula is determined by fitting the data to Eq.(3.1) after the data at $T \geq 53.6$ mK are shifted by 30 Ω.

$$\frac{1}{T} = \sum_{n=-2}^{2} a_n (\ln R)^n. \tag{3.1}$$

3.3 Heat capacity measurements

3.3.1 Sample cell

Figure.3.3 shows a schematic view of the sample cell for heat capacity measurements [36]. In this sample cell, exfoliated graphite Grafoil (GTA grade, 127 μm thick) [11] is used as an adsorption substrate. Grafoil sheets are sandwiched between pure Ag foils and they are diffusive bonded to get better thermal connection over the whole substrate. The surface area of the substrate $A = 562.5 \pm 2.3$ m^2, obtained from a N_2 adsorption isotherm at 77 K as shown in Fig.3.4. The thermal connectivity between the sample cell stage and the Cu nuclear stage is controlled by the Zn HSW.

3.3.2 Adiabatic heat pulse method

We adopted two methods for heat capacity measurements, depending on the sample temperature. In the temperature region of $T \geq 0.3$ mK, the adiabatic heat pulse method was adopted. In this method, temperature change ΔT was measured after a heat pulse $\dot{Q}$ was applied to the sample cell which was thermally isolated by opening the Zn HSW. Then the sample heat capacity can be calculated using the relation $C = \dot{Q}/\Delta T$. The power of the heat pulse was chosen to keep $\Delta T/T$ around 10 – 20 %. Measured heat capacities includes not only the ^{3}He sample but also the Grafoil substrate and other parts of the sample cell stage, so the contribution from the empty cell (hereafter we call it "addendum") must be subtracted from the total heat capacity. The addendum heat capacity will be discussed

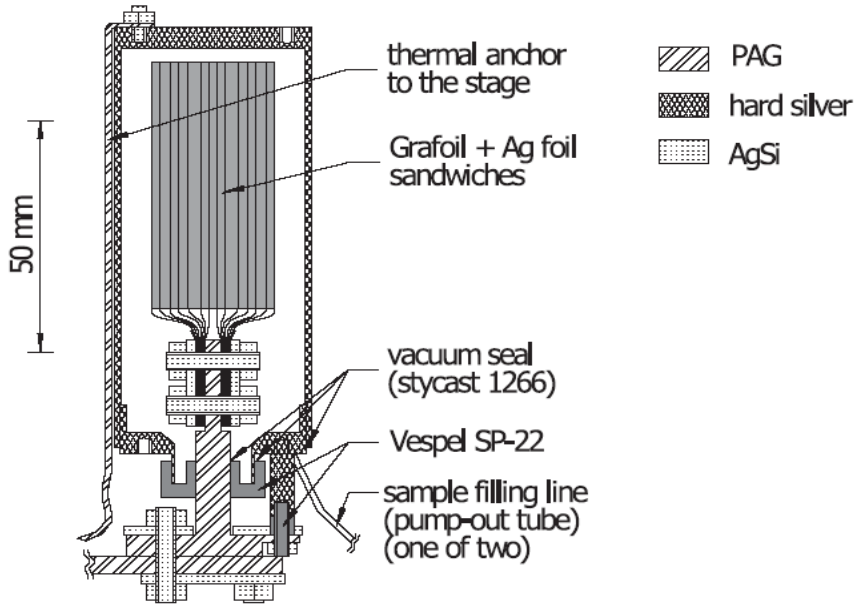

Fig. 3.3: left: Schematic drawing of the Pt pulsed-NMR thermometer (Ref.[36]). right: Schematic drawing of the sample cell for heat capacity measurements (Ref.[36]).

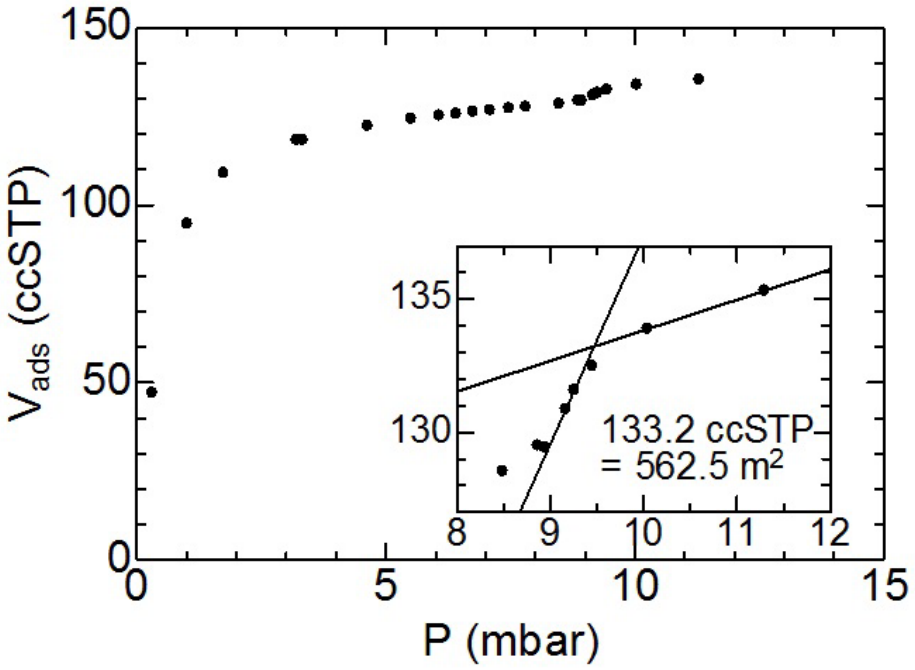

Fig. 3.4: N_2 pressure isotherm at $T = 77$ K. The small substep near $P = 9$ mbar corresponds to the formation of the $\sqrt{3}\times\sqrt{3}$ commensurate structure with $\rho = 6.37$ nm^{-2}. The inset is a close-up around the substep.

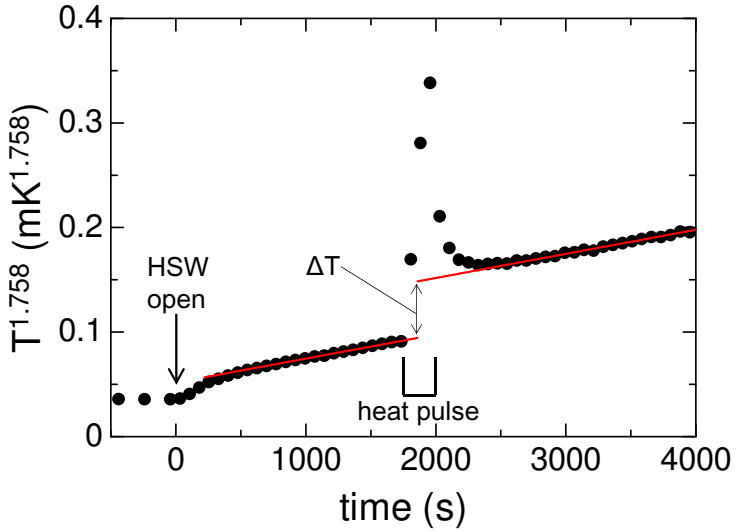

Fig. 3.5: Typical time evolution of the temperature T of the cell containing a ^{3}He film of 5.92 nm^{-2} measured by the Pt NMR thermometer during a heat capacity measurement by the adiabatic heat pulse method. At $t = 0$ the HSW was opened. At $t = 1859$ s, a heat pulse of 3.35 nW $\times$ 199 s was applied. The red solid lines are interpolations of the data to $t = 1859$ s by fitting the data to Eq.(3.4).

later. The temperature rose before the first heat pulse, due to latent heat of the Zn HSW and an ambient heat leak to the cell. The highest measuring temperature was $T \approx 90$mK above which the thermal conductivity of the Zn HSW increased steeply.

An example of heat capacity measurements by the adiabatic heat pulse method is shown in Fig.3.5. The applied heat Q was determined by the following relation

$$Q = IV\Delta t \tag{3.2}$$

where I and V are applied current and voltage, and Δt is the width of the heat pulse. To determine ΔT, time evolutions of the temperature before and after the heat pulse are extrapolated to the pulse center time, but the temperature data just after the heat pulse should not be used because of the overshooting. The data after the thermal equilibrium in the cell was achieved must be used. If the heat capacity can be approximated to be a constant over wide range of time before and after a heat pulse, the temperature changes linearly with time. However, it is not the case for the actual measurements. Therefore we assumed that the heat capacity C follows $C = AT^\alpha$. Then the time evolution of the temperature during natural warming up can be written as

$$\frac{\mathrm{d}T}{\mathrm{d}t} = \frac{1}{C}\frac{\mathrm{d}q}{\mathrm{d}t} = \frac{\dot{q}}{C}, \tag{3.3}$$

where $\dot{q}$ is a heat leak into the call during natural warming up. By integrating Eq.(3.3) assuming a constant heat leak, we obtain

$$t = \begin{cases} \frac{(\alpha+1)A}{\dot{q}} T^{\alpha+1} & (\alpha \neq -1) \\ \frac{A}{\dot{q}} \log T & (\alpha = -1). \end{cases} \tag{3.4}$$

Therefore T can be fitted to a power function. Typical α value is 1 ± 1 at $T < 1$ mK, and 0 ± 1 at $1 < T < 20$mK. At higher temperatures α change drastically from ≈ 10 to ≈ -10. One can calculate the heat leak into the sample cell when the Zn HSW is opened from the temperature change of the sample cell. The heat leak estimated using the data in Fig.3.5 is 0.16 ± 0.01 μJ is approximately 3 % of the total latent heat of Zn (5.3 μJ). It is useful to measure the natural warm up curve when the HSW is opened in advance because one can estimate when the overshoot finishes by comparing the time evolution of the temperature after the pulse and that in natural warm up by the ambient heat leak. In addition, the ambient heat leak into the sample cell stage can be estimated from the natural warming up and the value was typically about 0.5 nW. The heat leak was 5 – 10 nW when thermometry was done with the Pt NMR thermometer with 90° pulses, because of the large heat generated by the pulses. At $T > 30$ mK the heat leak became negative because the temperature of the cell stage was higher than that of the mixing chamber stage of the dilution refrigerator.

3.3.3 Addendum heat capacity

As mentioned in Sec.3.3.2, the adiabatic heat pulse method measures the total heat capacity including not only ^{3}He samples but the Grafoil substrate and other parts of the sample cell stage. Therefore, it is necessary to measure the heat capacity of the addendum in advance and subtract the addendum contribution from the raw data to extract the heat capacity of ^{3}He. In our case, the contribution from a bilayer of HD must also be subtracted. The heat capacity of the addendum and the HD was measured twice. The first measurements were conducted just after the HD film was made and before making the first ^{3}He sample (4.74 nm^{-2}). The second measurements were after evacuating the ^{3}He sample (see Sec.4.1.2). Both of these data are plotted in Fig.3.6 and agree well with previous measurements of the addendum heat capacity which are shown as the crosses in Fig.3.6 [36]. This means that the heat capacity of a bilayer if HD is negligible in this temperature range. The addendum heat capacity displayed characteristic temperature dependence. The T-linear behavior at $T > 10$ mK can be explained by the electron heat capacity of Ag. The amount of Ag contained in the cell stage is $\approx$400 g, and the calculated heat capacity of Ag electrons is shown as the dashed line in the Fig.3.6. The low T behavior is believed to be the contribution from the Grafoil substrate.

The heat capacity at $T < 10$ mK is not fully understood, it is qualitatively explained by a sum of Schottky type specific heat of C^{13} atoms contained in Grafoil substrate. Local internal field in graphite can be induced at the edges or by magnetic impurities such as Fe. We made a simple estimation of a heat capacity of C^{13} atoms in the following consideration. For simplicity we assume a square lattice with lattice constant $a_C = 0.142$ nm and all electron spins at platelet edges are ferromagnetically ordered. Under this assumption, the internal field B at a site separated from the edge by distance r is expressed as

$$B(r) = \frac{\mu_0 \mu_e}{2\pi r^2 \sqrt{3} a_C}, \tag{3.5}$$

where μ_e is the electron magnetic moment. It causes the Zeeman splitting of the C^{13} nuclear spin at the site $\Delta E = 2\mu_{^{13}C} B(r)$, where $\mu_{^{13}C}$ is the nuclear magnetic moment of

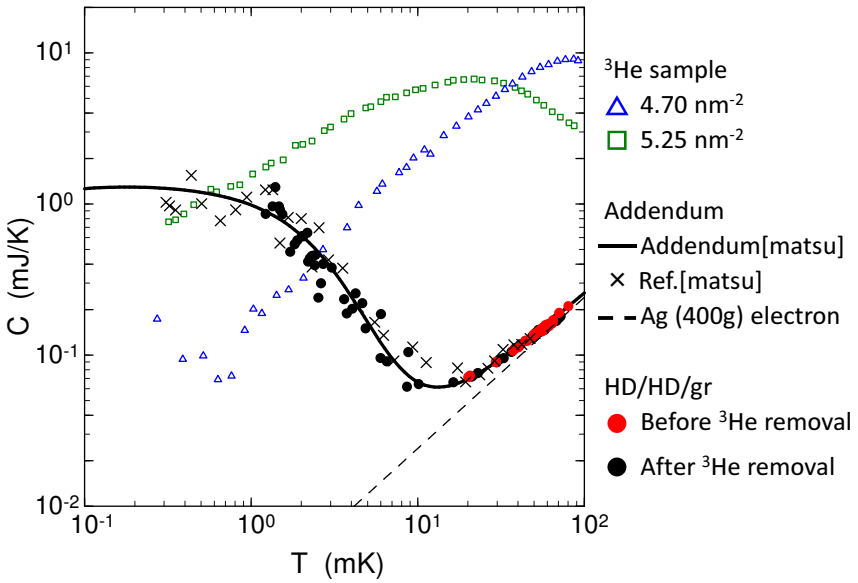

Fig. 3.6: The solid line is the addendum heat capacity determined in Ref.[36]. The red filled circles are the addendum heat capacity data in the series 1A (see Table.4.1 in Sec.4.3) obtained just after the HD preparation. The black filled circles are the data in the series 1B obtained just after evacuating the ^{3}He sample as described in Sec.4.1.2. The crosses are the data obtained in previous workers [36]. The dashed line is electron heat capacity of Ag contained in the cell (400 g). Heat capacities of ^{3}He samples of two densities are also plotted by the triangles (4.18 nm^{-2}) and squares (4.74 nm^{-2}).

C^{13}. Therefore the specific heat of the C^{13} atom is

$$C(r) = k_{\rm B}\left(\frac{\Delta E}{k_{\rm B}T}\right)^2 \frac{1}{\cosh^2(\Delta E/k_{\rm B}T)}, \tag{3.6}$$

$$= k_{\rm B}\left(\frac{2\mu_{^{13}{\rm C}}B(r)}{k_{\rm B}T}\right)^2 \frac{1}{\cosh^2(2\mu_{^{13}{\rm C}}B(r)/k_{\rm B}T)}, \tag{3.7}$$

$$= \frac{1.32\times10^{-62}}{r^4T^2}\frac{1}{\cosh^2(9.66\times10^{-22}/r^2T)}. \tag{3.8}$$

The number of platelets and the number of C^{13} atoms per platelet in the cell used in this work can be deduced from the adsorption surface area $A = 562.5$ m^2 and the typical platelet size 50×50 nm^2 [12]. Using these values and the natural abundance of C^{13} (1.1 %), the number of C^{13} atoms at the sites separated from the edge by $na_{\rm C}$ ($n = 0, 1, 2, \cdots$) is estimated as $\approx 3\times10^{18}$. When the contribution from C^{13} at an edge is calculated using $r = a_{\rm B}$ (Bohr radius), a summation of Eq.(3.8) roughly reproduce the temperature dependence of the addendum heat capacity at $T < 10$ mK, but the magnitude is two orders of magnitude smaller than the measurements. Note that this simple estimation ignores magnetic impurities and the thickness of the platelets (≈ 10 graphene sheets), which may compensate the difference.

3.3.4 Thermal relaxation method

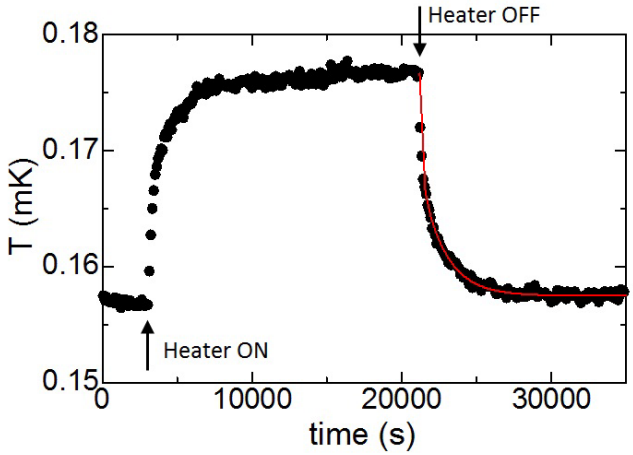

Fig. 3.7: Typical time evolution of the temperature T of the sample cell containing a ^{3}He film of 6.33 nm^{-2} measured by the Pt NMR thermometer during a heat capacity measurement by the thermal relaxation method. The heater power of 162 nW was turned on and off at time indicated by the arrows. The solid line is a fitting of the data to Eq.(3.9).

In the temperature region of $T \leq 0.6$ mK, the thermal relaxation method was adopted. The consistency between this method and the adiabatic heat pulse method was checked in the overlapping temperature. In this method, we applied constant heat q into the sample cell which had weak thermal connection to the Cu stage (heat bath). The thermal conductance between them was $K_{\rm b}$. Then we observed the thermal relaxation process. If the thermal relaxation time in the cell is negligible compared with that between the cell and the Cu stage, the relaxation process satisfies $T(t) = \Delta T e^{-t}$, where ΔT is the difference between the temperatures before and after the heater is turned on/off. In this case, the heat capacity C is deduced as $C = q/K_{\rm b}$. However, we measured more complicated relaxation processes in this experiment.

A typical thermal relaxation curve obtained in this study is shown in Fig.3.7. In this example a relaxation curve after the heater is turned off is analyzed. As shown in Fig.3.8, the relaxation curve was not fitted well by a single exponential but by a double exponential fashion

$$T = A_1 \exp(-t/\tau_1) + A_2 \exp(-t/\tau_2). \tag{3.9}$$

The fitted curve is also drawn in Fig.3.7 as the solid line. This behavior can be explained by the three-bath model [99] because the thermal conductance between the sample and the addendum ($K_{\rm a}$) cannot be ignored compared with $K_{\rm b}$. The schematic picture of this model is shown in Fig.3.9. Here, the short relaxation represents that between the addendum and Cu stage, and the long relaxation between the sample and addendum. Using this model, the heat capacities of the sample $C_{\rm sample}$ and the addendum $C_{\rm add}$, K_a,

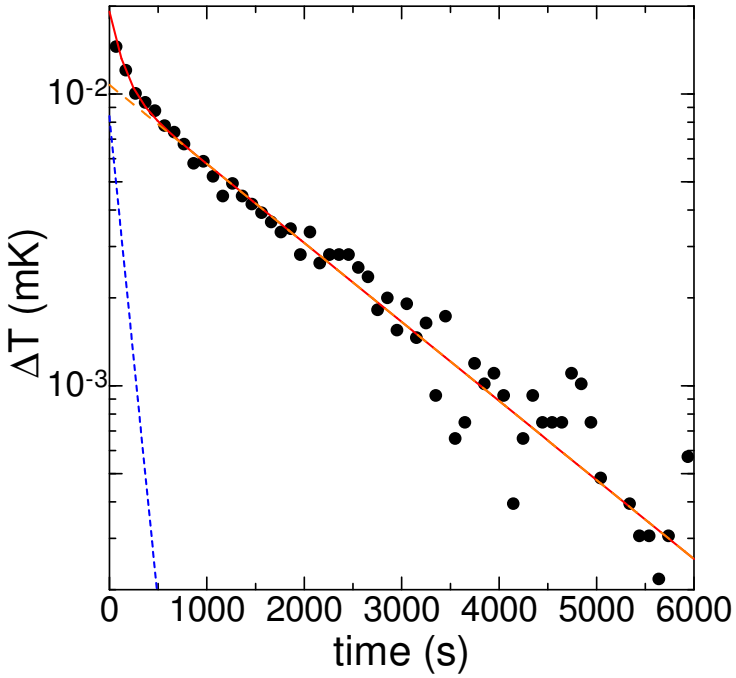

Fig. 3.8: Semi-log plot of the temperature change after the heater power was turned off shown in Fig.3.5. The solid line is a fitting of the data to the double exponential function (Eq.(3.9)). The dotted and dashed lines are two exponential components in the equation.

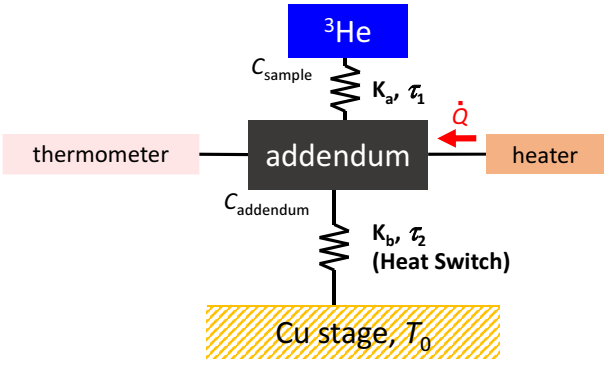

Fig. 3.9: Schematic diagram of the three bath model (Ref.[99]).

and K_b were deduced from fitted parameters A_1, A_2, τ_1, and τ_2 by following the relations [99],

$$K_b = \dot{Q}/\Delta T = \dot{Q}/(A_1 + A_2), \tag{3.10}$$

$$C_{\rm sample} + C_{\rm add} = K_b(A_1\tau_1 + A_2\tau_2)/(A_1 + A_2), \tag{3.11}$$

$$\tau_{\rm sample}\tau_{\rm add} = \tau_1\tau_2, \tag{3.12}$$

$$\tau_{\rm sample} \equiv C_{\rm sample}/K_a = (A_2\tau_1 + A_1\tau_2)/(A_1 + A_2), \tag{3.13}$$

$$\tau_{\rm add} \equiv C_{\rm add}/K_b, \tag{3.14}$$

where $\dot{Q}$ is heat flow into the sample cell, deduced from I and V of the heater. K_b can

be controled by changing the applied field to the Zn HSW. When the applied field to the HSW is fixed at the value, K_b satisfied $K_b \propto T$, because a normal part of Zn obey the Wiedemann-Franz law. This T dependence is confirmed by the measurements. Using this relation the number of fitting parameter is reduced and the accuracy of the analysis is improved [36]. The relaxation curve is first analyzed in which K_b is treated as a fitting paramter, and the T dependence of K_b is fitted to $K_b = aT$. This result can be used as a constraint condition starting from the next analysis as long as the applied field to the Zn HSW is unchanged.

Chapter 4

Sample preparation

4.1 Preparations for bilayer of HD and monolayer of ^{3}He

4.1.1 Fabrication of HD and ^{3}He films

The gas handling system (GHS) used for sample preparation is shown in Fig.4.1. HD (3 % impurity of H_2 and D_2) and ^{3}He (99.9 % purity) gases were introduced into the sample cell through a CuNi capillary after the amount of them were measured using a standard volume (V_{STD} = 50.5 cc). There was a N_2 cold trap between the GHS and the cryostat in order to remove impurity gases.

What should be done to fabricate the atomic/molecular film was to introduce gases into the sample cell and cool it down. At low temperatures the atoms/molecules in the cell were adsorbed on the graphite surfaces because of the strong binding potential. The nominal areal density ρ_{nominal} of a sample was determined as the number of atoms N divided by the surface area of the Grafoil substrate A (= 562.5 m^2). N was calculated from the pressure, temperature, and V_{STD} before introduction.

The HD gas was introduced while the refrigerator was cooled down from 77 to 4.2 K. We made the HD films of 18.50 nm^{-2} and the density corresponds to 2.03 layers [21]. The

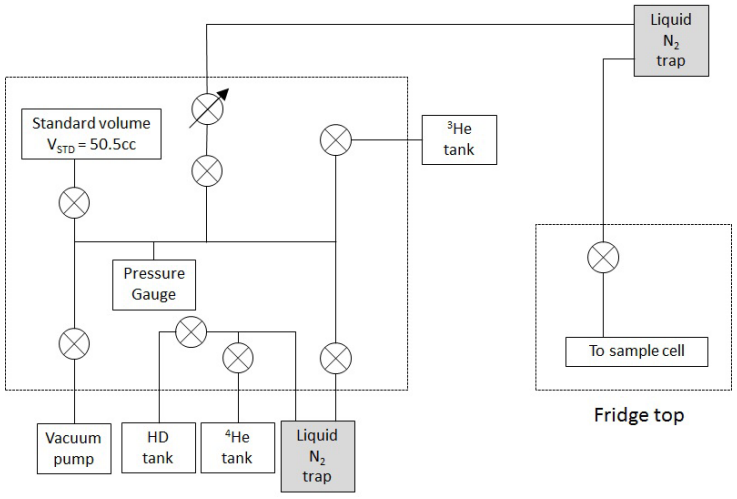

Fig. 4.1: Gas handling system used for ^{3}He and HD sample preparation.

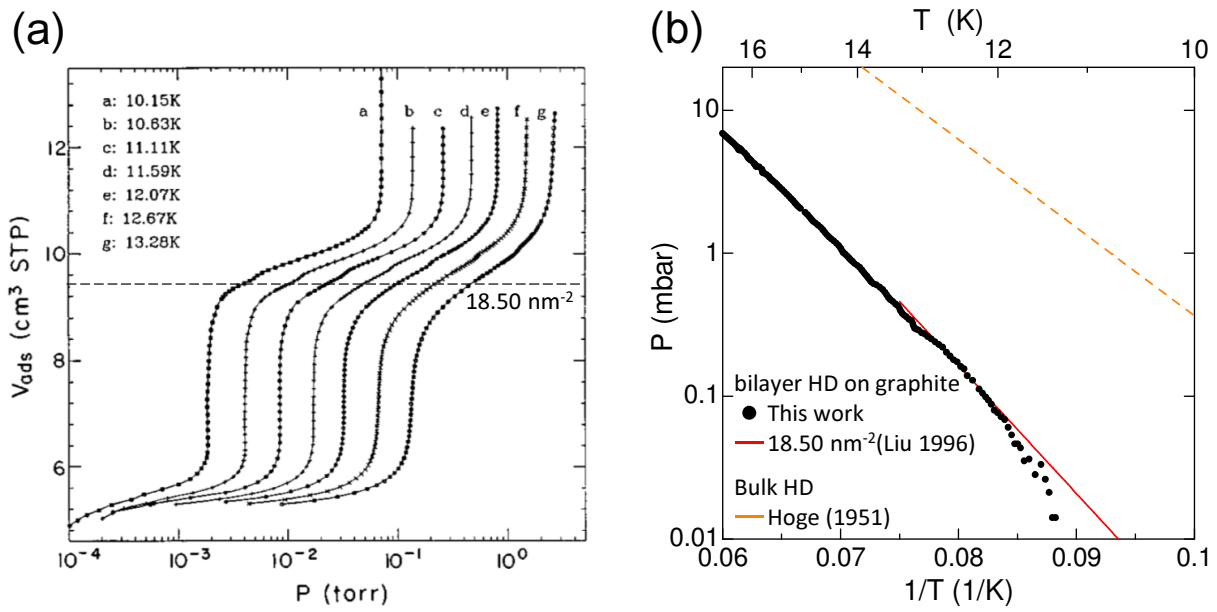

Fig. 4.2: (a) Pressure isotherms of HD films on Grafoil (Ref.[100]). The horizontal dashed line represents $\rho = 18.50$ nm^{-2}. (b) The temperature dependence of measured pressure of a bilayer of HD after introducing 387 ccSTP of HD gas to the sample cell in Run1. The red solid and orange dashed lines represents the vapor pressure of a HD film of 18.50 nm^{-2}(Ref.[100]), and of the bulk HD (Ref.[101]), respectively.

amount of the introduced gas was determined according to the previous vapor pressure measurements of HD films on Grafoil shown in Fig.4.2 [100]. We monitored the vapor pressure in the sample cell while cooling the refrigerator in order to check whether the bilayer was properly made by comparing the data to the results of previous adsorption isotherms [100] (red line in Fig.4.2). After introduction of the proper amount of HD, we had to take care to avoid the capillary blocking by condensation of HD. Because we used the small capillary (i.d. 0.6 mm, o.d. 0.8 mm), it is easily blocked by the high vapor pressure or quick temperature decrease. The triple point of HD is $T = 16.6$ K and $P = 0.122$ bar [101], so we tried to keep the pressure below this value. After introduction of HD, we cooled down the refrigerator at 2 K/hour monitoring the pressure in the cell. The orange dashed line in Fig.4.2 represents the vapor pressure of bulk HD [101]. Measured pressure in the cell is less than this line. This is the proof that the capillary condensation do not occur in this experiment. It was desired to take an adsorption isotherm of HD, but we were not able because the refrigerator used in this work did not have the system to keep constant temperature at $T > 10$ K. We had to control the temperature of the refrigerator by changing the power of a heater mounted on the dewer and the flow rate of liquid ^{4}He into the dewer. After cooling the refrigerator to 4.2 K, we warmed it up again to anneal the HD layers at 12.5 ± 0.5 K for more than 10 hours to make the film smooth.

The ^{3}He gas was introduced at 2.33 K. To check the reproducibility of the sample we took the adsorption isotherms at this temperature as shown in Fig.4.3. In this work, we did two series of the measurements (Run1 and Run2). Between Run1 and Run2,

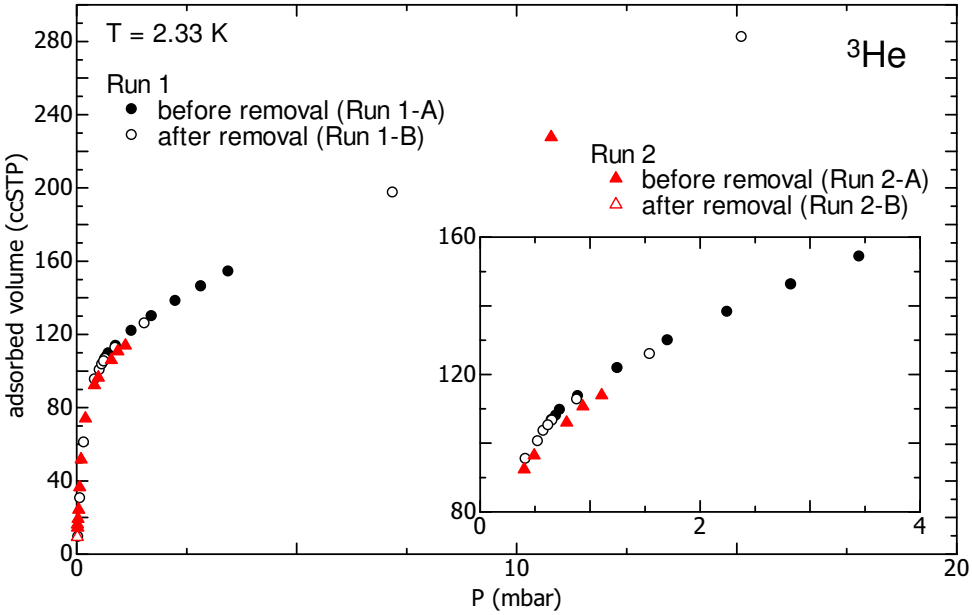

Fig. 4.3: The adsorption isotherms of ^{3}He films on the Grafoil substrate preplated with the HD films of 18.50 nm^{-2} at $T = 2.33$ K. The filled black circles are data obtained before evacuating the ^{3}He sample (see Sec.4.1.2), and the open black circles are those after the evacuation in Run1. The filled red triangles are the data obtained before the ^{3}He sample removal (see Sec.4.1.2), and the open red triangle is taken after the evacuation in Run2. The remnant ^{3}He coverage after the removal is estimated to be less than 0.005 nm^{-2}.

we evacuated the HD film and made the new one. Although we tried to make the HD film by the same method as in both runs, the qualities of these two HD films were not the same. The run to run dependence can be seen in the ^{3}He adsorption isotherms as shown in Fig.4.4. Because the vapor pressure in the cell was measured by a pressure gauge at room temperature which were connected through the thin capillary, measured pressure was tend to be higher than the actual value in the cell due to an effect called the thermomolecular pressure difference. The ratio of the high-T pressure and the low T pressure $p_{\rm low}/p_{\rm high}$ depends only on an product of the radius of the capillary r and the high T pressure $r \cdot p_{\rm high}$. The data plotted in Fig.4.4 are the corrected pressure using the data in Ref.[102] and $r = 0.85$ nm. The vapor pressure in Run2 was higher than the value in Run1 at the same introduction amount of ^{3}He. This difference was supposed to come from the difference in the amount of the amorphous ^{3}He. The amorphous ^{3}He is adsorbed on the surface heterogeneities whose binding potential is deeper than the potential of the flat surfaces, so the vapor pressure depends only on the amount of ^{3}He on the flat surfaces. This means that the y-intercept of the adsorption isotherm correspond to the amount of the amorphous ^{3}He. The difference in the y-intercept between the isotherms indicated that the quality of the HD film in Run2 was better than that in Run1. What caused the difference in the qualities of the HD films was the difference in the cooling processes after annealing the HD films from $T \approx 12$ K. We tried to cool down the refrigerator slowly, but in Run1 accidentally the temperature dropped quickly from 11.5 to 4.2 K at ≈ 8 K/hour.

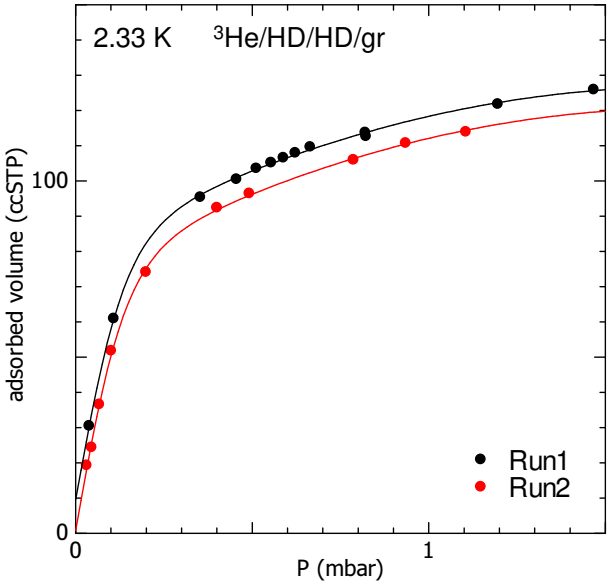

Fig. 4.4: Adsorption isotherms of the ^{3}He samples in the low pressure region. The black symbols are the data in Run1 and the red ones are in Run2. The black solid lines represents the Eq.(4.1). The red solid line is the fitting of the data in Run2 to Eq.(4.2).

On the other hand, in Run2 we cooled down the refrigerator at ≈ 1 K/hour from 12 K to 10 K, and then cooled down to 4.2 K quickly.

Since the amount of the amorphous ^{3}He was different, the same nominal density in Run1 and Run2 did not mean the same ^{3}He density on the flat surfaces of the substrate. Therefore we corrected the difference in the density scale between the Run1 and Run2 in the following way. First, the adsorption isotherm of Run1 at $0.03 < P < 1.5$ mbar was fitted to obtain

$$V_{\rm run1}(P)[{\rm ccSTP}] = 7.01 \tanh\left(\frac{P}{0.139}\right) + 54.4P + 15.7P^2 + 9.56, \tag{4.1}$$

where, the last term is the y-intercept corresponding to the amount of amorphous ^{3}He. This function is not based on a certain physical model but just for fitting the data smoothly. By assuming that the density correction is expressed by a linear function, we fitted the data in Run2 to

$$V_{\rm Run2}(P)[{\rm ccSTP}] = aV_{\rm Run1}(P) + b, \tag{4.2}$$

where the fitting parameter a and b correspond to the difference in the surface area and amount of the amorphous ^{3}He, respectively. This fitting yielded $a = 1.026$ and $b = -9.29$ ccSTP, which means that the effective surface area increased by 2.6% in Run2 thanks to the reduction of the amorphous component. From these values the average density of the amorphous ^{3}He was estimated as $\rho = 17.2$ nm^{-2}, 1.5 times larger than the 1st layer completion density of 11.6 nm^{-2} [16]. The density correction formula was deduced by dividing both sides of Eq.(4.2) by the surface area of the substrate. Finally, the formula was given as

$$\rho_{\rm Run2}[{\rm nm}^{-2}] = 1.026\rho_{\rm Run1}[{\rm nm}^{-2}] - 0.445, \tag{4.3}$$

where $\rho_{\rm run1}$ and $\rho_{\rm run2}$ are the nominal densities of Run1 and Run2, respectively.

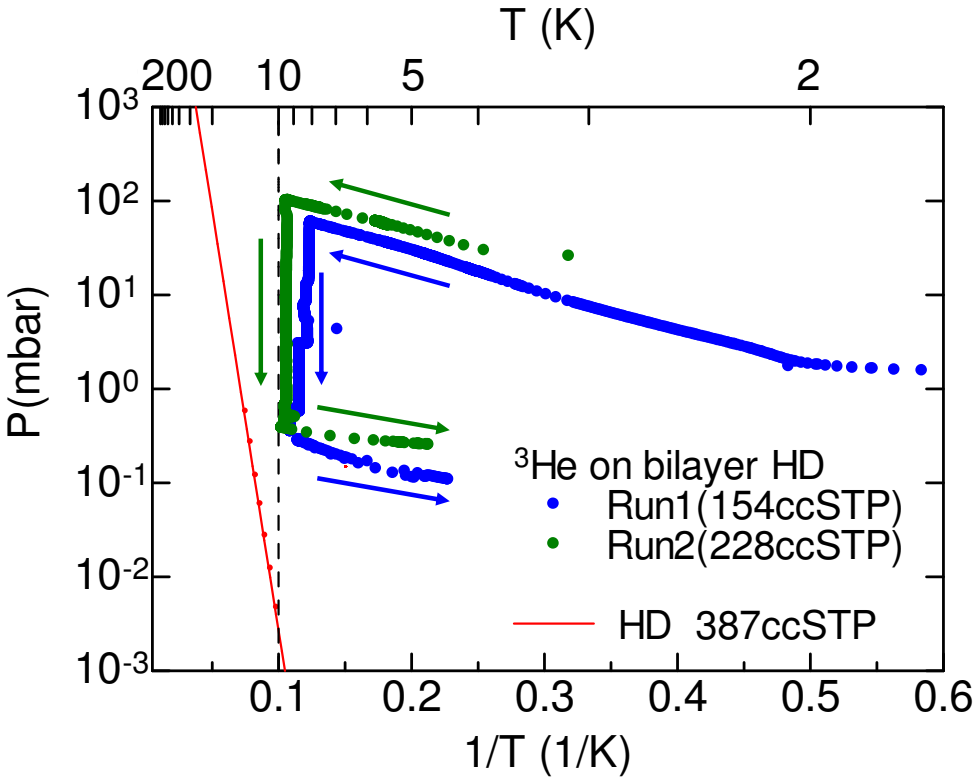

Fig. 4.5: The ^{3}He pressure change while the evacuation of ^{3}He from the cell in Run1 (the blue circles) and in Run2 (the green symbols). The arrows indicate the direction of time evolution. The red line is the vapor pressure of a bilayer of HD (Ref.[100]). The ^{3}He evacuation was carried out at temperatures just below 10 K indicated by the vertical dashed line where the vapor pressure of the HD film is sufficiently low not to change the preplating coverage and the pressure of ^{3}He film is reasonably high so that the selective evacuation of ^{3}He is possible.

4.1.2 ^{3}He removal

Due to the method of fabricating ^{3}He samples described above, it is easy to increase the areal density by simply introducing the additional ^{3}He gas into the cell. However, it is difficult to reduce the density. We tried to pump out the ^{3}He sample keeping the HD film undamaged. This is possible at the temperature where the vapor pressure of the ^{3}He film is high enough to be pumped out but that of HD is negligibly small. Figure 4.5 shows the vapor pressure as a function of the inverse temperature of the sample cell. The ^{3}He sample was pumped for 60 hours in between 8 and 10 K. The adsorption isotherms of the ^{3}He samples before and after the ^{3}He removal (hereafter series A and B), shown in Fig.4.3, agreed very well in both runs. The remnant ^{3}He density estimated from the adsorption isotherm is smaller than 0.005 nm^{-2}.

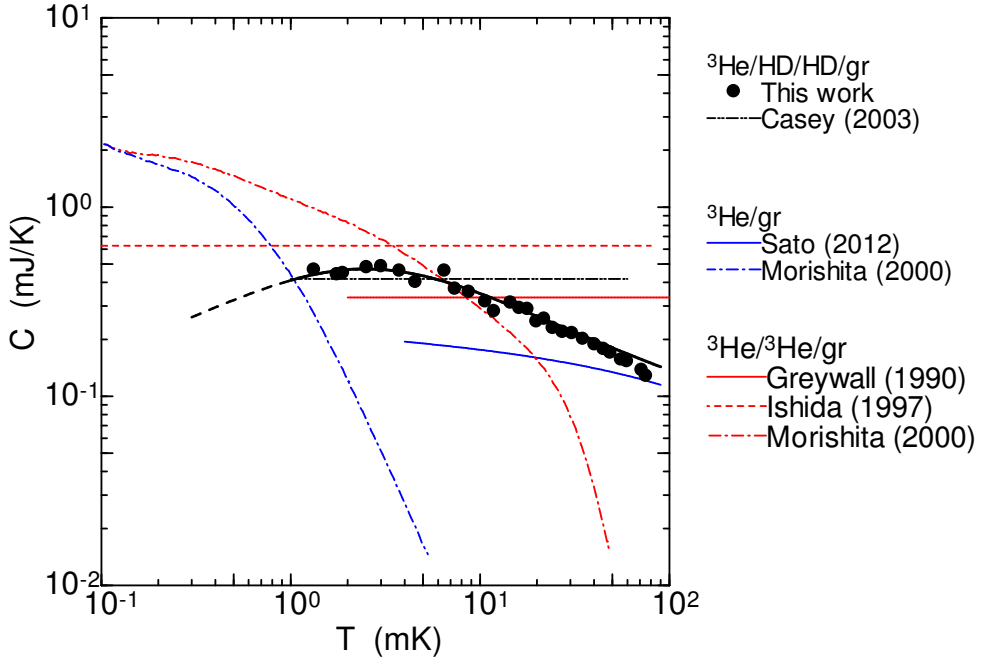

Fig. 4.6: Heat capacity data of monolayer of ^{3}He at $\rho_{\mathrm{Run1}} = 0.46$ nm^{-2}. Note that at such a low density most of ^{3}He atoms are trapped not at a flat surface but at substrate heterogeneities forming the amorphous phase with effectively much higher densities. The amorphous heat capacities used in the previous works are also shown for comparison. The thick black line is a fitting of the data in this work to Eq.(4.4). The black dashed line is the extrapolation of it. The thin black dashed double-dotted line is the amorphous heat capacity of ^{3}He/HD/HD/gr (Ref.[39]). The blue lines are the amorphous heat capacities of ^{3}He/gr reported in Ref.[23] (the solid line) and Ref.[41] (the dashed-dotted line). The red lines are those of ^{3}He/^{3}He/gr reported in Ref.[24] (the solid line), Ref[6] (the dashed line), and Ref.[41] (the dashed-dotted line). The temperature ranges of these lines correspond to those of the heat capacity measurements.

4.2 Heat capacity of amorphous ^{3}He

Heat capacities (C) of the ^{3}He sample at $\rho_{\mathrm{Run1}} = 0.46$ nm^{-2} in Run1 are shown in Fig.4.6. The heat capacity of ^{3}He monolayer on a bilayer HD at such a low density was investigated for the first time The previous heat capacity measurements on this system were performed at densities from 1.00 nm^{-2} [39]. The C data at $\rho_{\mathrm{Run1}} = 0.46$ nm^{-2} increases gradually with decreasing temperature. In this figure, the amorphous heat capacity of other ^{3}He monolayer systems are also shown for comparison. The black dashed double-dotted line is the amorphous of ^{3}He/HD/HD/gr [39], the blue lines are the amorphous of ^{3}He/gr [23, 41], and the red lines are the amorphous of ^{3}He/^{3}He/gr [6, 24, 41]. Note that in Ref.[39] the amorphous heat capacity is not explicitly reported, so the value in the figure is the estimated by fitting their raw data by ourselves. The detail of the fitting is described in Appendix A. Similar gradual T-dependences have been observed in low density ^{3}He

films adsorbed directly on the same Grafoil substrate as that used in the present work [23].

As discussed in Sec.2.2.4, ^{3}He atoms are adsorbed preferentially on the substrate heterogeneities, rather than the flat surfaces, forming the amorphous structure. The weak temperature dependencies observed at $\rho_{\mathrm{Run1}} = 0.46$ nm^{-2} in this work and even lower densities in Ref.[23] are roughly consistent with the constant heat capacity predicted by the Golov-Pobell model [42]. The heat capacity data for $\rho_{\mathrm{Run1}} = 0.46$ nm^{-2} are larger by a factor of two to three compared with that of the amorphous ^{3}He adsorbed directly on the Grafoil substrate [23] at $\rho_{\mathrm{nominal}} = 0.45$, shown by the blue solid line in Fig.4.6.

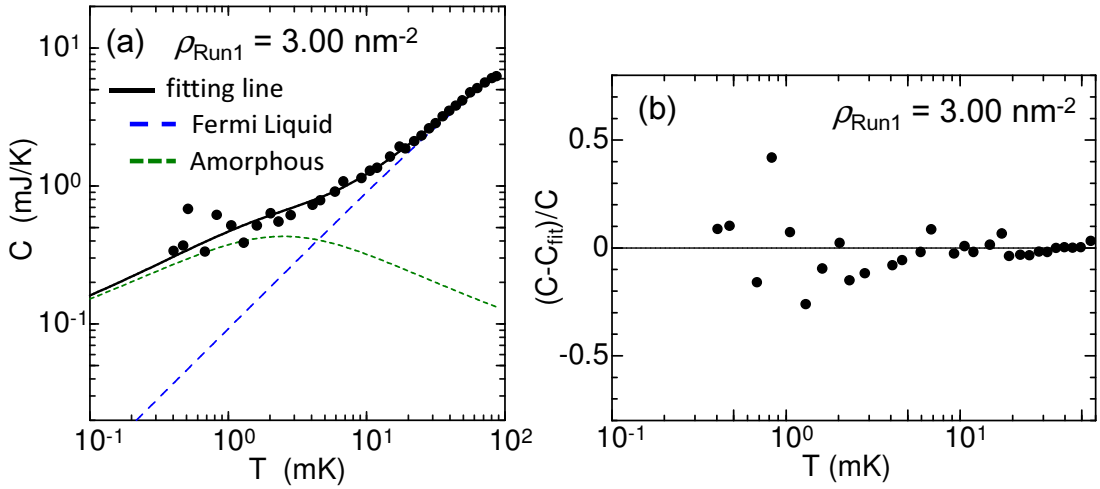

Fig. 4.7: (a)Heat capacity data at $\rho_{\mathrm{Run1}} = 3.00$ nm^{-2} and the fitting to Eq.(4.5) (solid line). The blue dashed and green dotted lines are a contribution from a 2D Fermi liquid and amorphous ^{3}He, respectively. (b) Deviation of the $\rho_{\mathrm{Run1}} = 3.00$ nm^{-2} data from the fitting function given in Eq.(4.5).

We assume the temperature dependence of the heat capacity at $\rho_{\mathrm{Run1}} = 0.46$ nm^{-2} as a typical heat capacity of the amorphous ^{3}He, C_{amor}, of ^{3}He/HD/HD/gr. We determine the T dependence of C_{amor} as the following form,

$$C_{\mathrm{amor}}(T) = \frac{0.9585}{1.96\log(1.3T)^2 - 2.0\log(1.3T) + 2.555} + 0.00231, \tag{4.4}$$

which is shown as the black solid line in Fig.4.6. The dashed line is the extrapolation. Note that this function is not based on a certain physical model but just for reproducing the plots. To determine the T dependence of C_{amor} at low T ($T \lesssim 1$ mK) is difficult from the C data at 0.46 nm^{-2}, Therefore we estimated the low T behavior of C_{amor} from the C data in the Fermi liquid region where the heat capacity of the ^{3}He film on the flat surfaces are expressed as Eq.(2.22). To separate the contribution of the amorphous ^{3}He from that of the ^{3}He monolayer adsorbed on the flat surfaces of the substrate, we fitted the data to

$$C = \underbrace{\gamma T - \alpha T^2}_{\text{Fermiliquid}} + \underbrace{\eta C_{\mathrm{amor}}(T)}_{\text{amorphous}}, \tag{4.5}$$

where γ, α, and η are fitting parameters. An example of the fitted curve at $\rho_{\mathrm{Run1}} = 3.00$ nm^{-2} is shown in Fig.4.7(a), and deviation of the data from the fitting function is shown in Fig.4.7(b). The fitting quality is not largely different for other densities. In Run2, we did not directly measure C_{amor} because of better quality of the HD film. The lowest measuring density in Run2 was $\rho_{\mathrm{Run2}} = 0.30$ nm^{-2}, but the C data displayed the Fermi liquid type heat capacity of the $C \propto T$ dependence and the behavior did not disappear by adding ^{3}He. Therefore the temperature dependence is assumed to be the same as that in Run1. The density evolution of the amount of the amorphous ^{3}He N_{amor} deduced from the fitted parameter η in Eq.(4.5) are shown in Fig.4.8. Once the formation of the amorphous ^{3}He is completed, N_{amor} is almost density independent up to $\rho_{\mathrm{Run2}} = 4.2$ nm^{-2}. A similar behavior of N_{amor} was observed observed in the ^{3}He/gr system [23]. In Run2, N_{amor} is smaller than that in Run1. This is consistent with the larger y-intercept of the adsorption isotherm in Run1 (see Fig.4.4). The weak density dependence of N_{amor} obtained from the previous NMR measurements of ^{3}He/HD/HD/gr [17], shown as the crosses in Fig.4.8, is roughly consistent with the data in Run1. Note that the data of previous studies are plotted as a function of the nominal density ρ_{nominal}. We alto plot N_{amor} from the previous heat capacity measurements [39] deduced by the reanalysis using $C_{\mathrm{amor}}(T)$ obtained in this work, as the open circles in Fig.4.8. It also shows the weak density dependence up to $\rho_{\mathrm{nominal}} = 4.4$ nm^{-2}. The detail of the reanalysis is described in Appendix A.

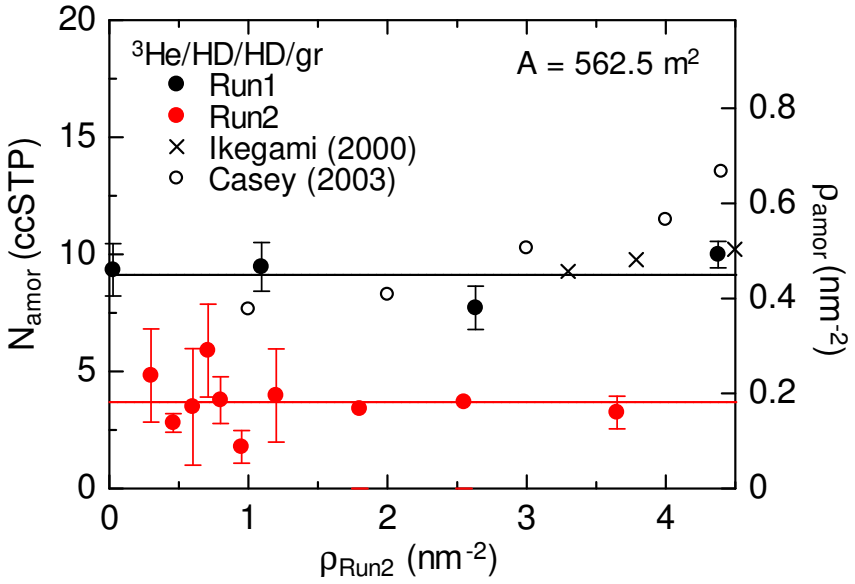

Fig. 4.8: The density evolution of the amount of ^{3}He in the amorphous state N_{amor}. Also shown are N_{amor} from the previous NMR measurements ($\times$, Ref.[17]) and heat capacity measurements reanalyzed using $C_{\mathrm{amor}}(T)$ obtained by this work ($\circ$, Ref.[39], see Appendix A for the detail of the reanalysis).

In the later chapters, we focus on the heat capacity of the ^{3}He samples on the flat surfaces of the substrate. Therefore the data in the later chapters are those after subtracting the contribution of the amorphous ^{3}He discussed in this section. The heat capacity of the

^{3}He film on flat surfaces is expressed as

$$C(T) = \begin{cases} C_{\rm total}(T) - C_{\rm addendum}(T) - \eta C_{\rm amor}(T) & (\text{heat pulse method}), \\ C_{\rm sample}(T) - \eta C_{\rm amor}(T) & (\text{relaxation method}), \end{cases} \tag{4.6}$$

where $C_{\rm total}$ is the measured heat capacity and $C_{\rm addendum}$ is the addendum heat capacity shown in Fig.3.6. Note that in the thermal relaxation method the heat capacities of the ^{3}He sample and the addendum are separately deduced. At $\rho < 4.2$ nm^{-2}, η is deduced by fitting the data to Eq.(4.5). At $\rho > 4.2$ nm^{-2}, we assume the temperature independent amorphous fraction $\eta = 0.922$ for the data taken in Run1 and $\eta = 0.373$ in Run2, which correspond to the solid lines in Fig.4.8. Also, in the later chapters, when we calculate the specific heat $C/Nk_{\rm B}$ or the normalized spin entropy $S/Nk_{\rm B}\ln 2$, the number of spin N do not include that of ^{3}He atoms in the amorphous solid.

4.3 ^{3}He sample densities

Table 4.1 show all the sample densities of the ^{3}He films measured in this work. In this table ρ denotes the density of ^{3}He on the flat surfaces of the substrate. The amorphous density in Run2 was determined using the density dependence of the γ coefficient of the T-linear term of the heat capacity of the Fermi liquid. As mentioned in Sec.2.5, at extremely low densities γ changes linearly with the density. Therefore we estimated the amorphous density as the x-intercept of the linear fit of γ at the densities below a kink (see Sec.8.1) and obtain 0.20 ± 0.03 nm^{-2}. The value is consistent with 0.18 ± 0.02 nm^{-2} estimated from the η coefficients obtained by fitting the data to Eq.(4.5), shown as the red solid in Fig.4.8. Finally, ρ is

$$\rho = \rho_{\rm Run2} - 0.20, \tag{4.7}$$

$$= 1.026\rho_{\rm Run1} - 0.645. \tag{4.8}$$

The table also shows that each ^{3}He sample was measured in which run. Label A and B represent whether the sample was fabricated before or after the ^{3}He removal. The ρ coefficient of the data at $\rho_{\rm Run1} = 0.46$ in Run1 is not written because the corrected density by Eq.(4.7) is negative ($\rho = -0.17$ nm^{-2}). This correspond to the heat capacity data at this density which show only amorphous feature.

ρ (nm^{-2})	-	0.10	0.26	0.40	0.51	0.60	0.75	0.89	1.00	1.60
ρ_{nominal}	0.46	0.30	0.46	0.60	0.71	0.80	0.95	1.50	1.20	1.80
Run	1B	2A	2B	2A	2A	2A	2A	1B	2A	2A
ρ (nm^{-2})	2.35	2.43	3.45	4.18	4.35	4.43	4.55	4.59	4.67	4.74
ρ_{nominal}	2.55	3.00	3.65	4.70	4.55	4.95	4.75	5.10	5.18	5.25
Run	2A	1B	2A	1B	2A	1B	2A	1B	1B	1A, 1B
ρ (nm^{-2})	4.81	4.90	5.05	5.25	5.41	5.51	5.72	5.92	6.33	6.74
ρ_{nominal}	5.32	5.40	5.55	5.45	5.61	6.00	6.20	6.40	6.80	7.20
Run	1A	1A	1B	2A	2A	1A	1B	1A	1A	1A
ρ (nm^{-2})	7.15	9.33	11.01	13.63						
ρ_{nominal}	7.60	9.72	11.21	13.91						
Run	1A	1B	2A	1B						

Table 4.1: The ^{3}He sample densities at which heat capacity measurements were done in the present work. ρ denotes the density of ^{3}He on the flat surfaces of the substrate and ρ_{nominal} is the nominal density obtained by simply calculating N/A. The series A samples were first measured in order of density, and then the series B samples were measured after evacuating the ^{3}He samples of series A completely.

Chapter 5

Frustrated magnetism of compressible quantum phases

In this chapter, we discuss the results of heat capacity measurements on the ^{3}He/HD/HD/gr system at $\rho \geq 5$ nm^{-2}, shown as the colored region in Fig.5.1.

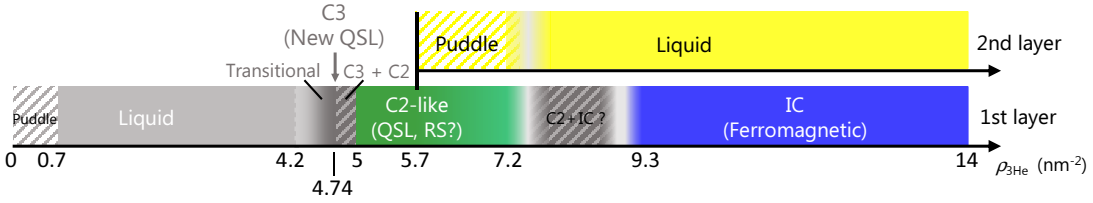

Fig. 5.1: Phase diagram of ^{3}He/HD/HD/gr. The shaded region is discussed in this chapter.

5.1 Compressible C2-like phase ($5.05 \leq \rho \leq 7.15$ nm^{-2})

Figure 5.2 shows the heat capacity data of the ^{3}He/HD/HD/gr system at $5.05 \leq \rho \leq 7.15$ nm^{-2}. At $5.05 \leq \rho \leq 5.92$ nm^{-2}, the heat capacities have very broad peaks and $C \sim \gamma T$ at low temperatures. As the density increases, the heat capacity peak shifts to lower temperatures without changing the entire shape of the heat capacity, as shown in Fig.5.2 (a). At $\rho > 5.92$ nm^{-2} this shift is slowed down, whereas the heat capacities for $T < 5$ mK and that at $T > 10$ mK increase, as shown in Fig.5.2 (b).

Scaling behavior

Firstly we focus on the heat capacity data at $5.05 \leq \rho \leq 5.92$ nm^{-2}.

The data at 5.05 and 5.25 satisfy $C \propto T$ at $T \ll T_{\rm peak}$, where $T_{\rm peak}$ is the peak temperature. The heat capacity decay at $T \gg T_{\rm peak}$ is slower than T^{-2} which is expected for localized spin systems. Above $T = 50$ mK the heat capacity decay becomes even slower. The slow down of the heat capacity decay is likely due to the effect of the heat capacity of 2D phonons which satisfy $C \propto T^2$. To extract the contribution of the nuclear

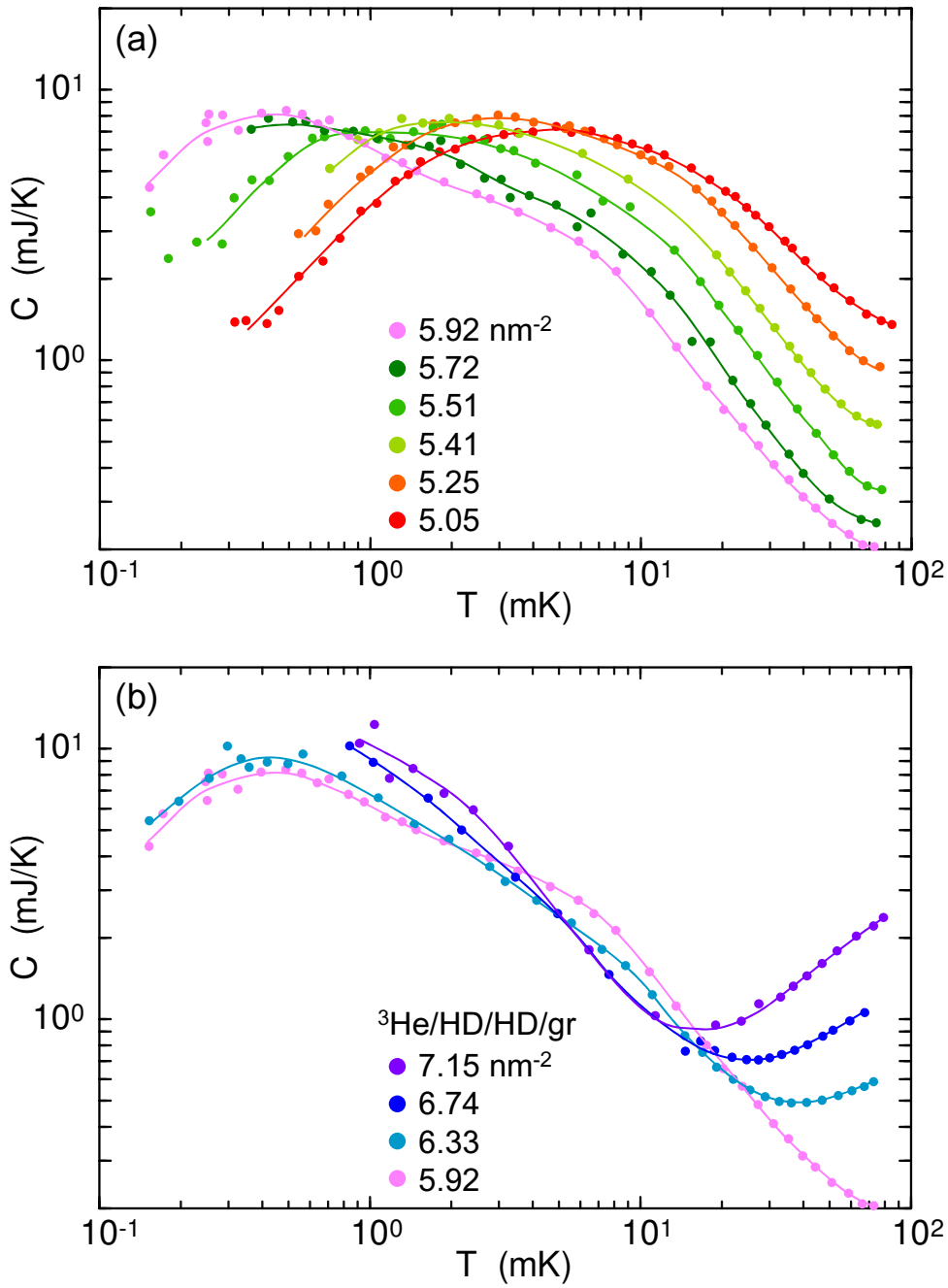

Fig. 5.2: (a) Heat capacity data of the ^{3}He/HD/HD/gr system at 5.05, 5.25, 5.41, 5.51, 5.72, and 5.92 nm^{-2}. As the density increases the heat capacity shifts to a low temperature without changing the shape of the curve. (b) The heat capacity data at 5.92, 6.33, 6.74, and 7.15 nm^{-2}. Clear increases in the heat capacity at $T \leq 5$ and $T \geq 10$ mK were observed. The solid lines are guides to the eye.

spins, the heat capacity data are fitted to

$$C = N_1 k_B P[2,2] + a_2 T^2, \tag{5.1}$$

where the T^2 term comes from the 2D phonons. $P[2,2]$ is the [2, 2] Padé approximation

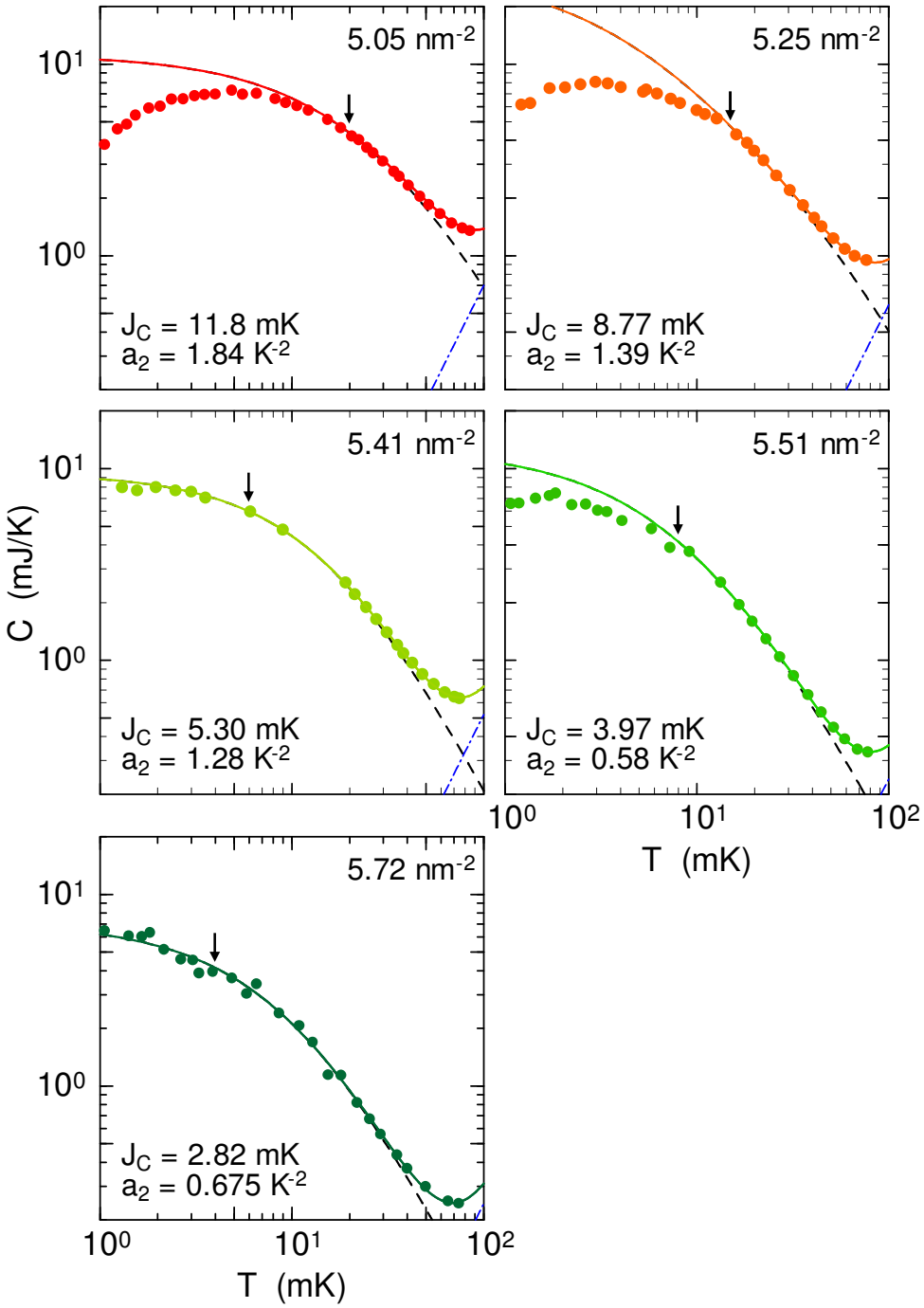

Fig. 5.3: The heat capacity data at 5.05, 5.25, 5.41, 5.51, and 5.72 nm^{-2} and the fitted curve using Eq.(5.1) for $T > T'$, where T' is the temperature indicated by the arrows. The black dashed and blue dashed-dotted lines represent the magnetic and 2D phonon contributions, respectively.

after the Euler transform $\beta' = \beta/(1+\beta)$, where $\beta = 1/k_{\mathrm{B}}T$. A $[L, M]$ Padé approximation is given by

$$A(\beta)_{L+M} = \frac{P_L}{Q_M} + O(\beta^{L+M+1}), \tag{5.2}$$

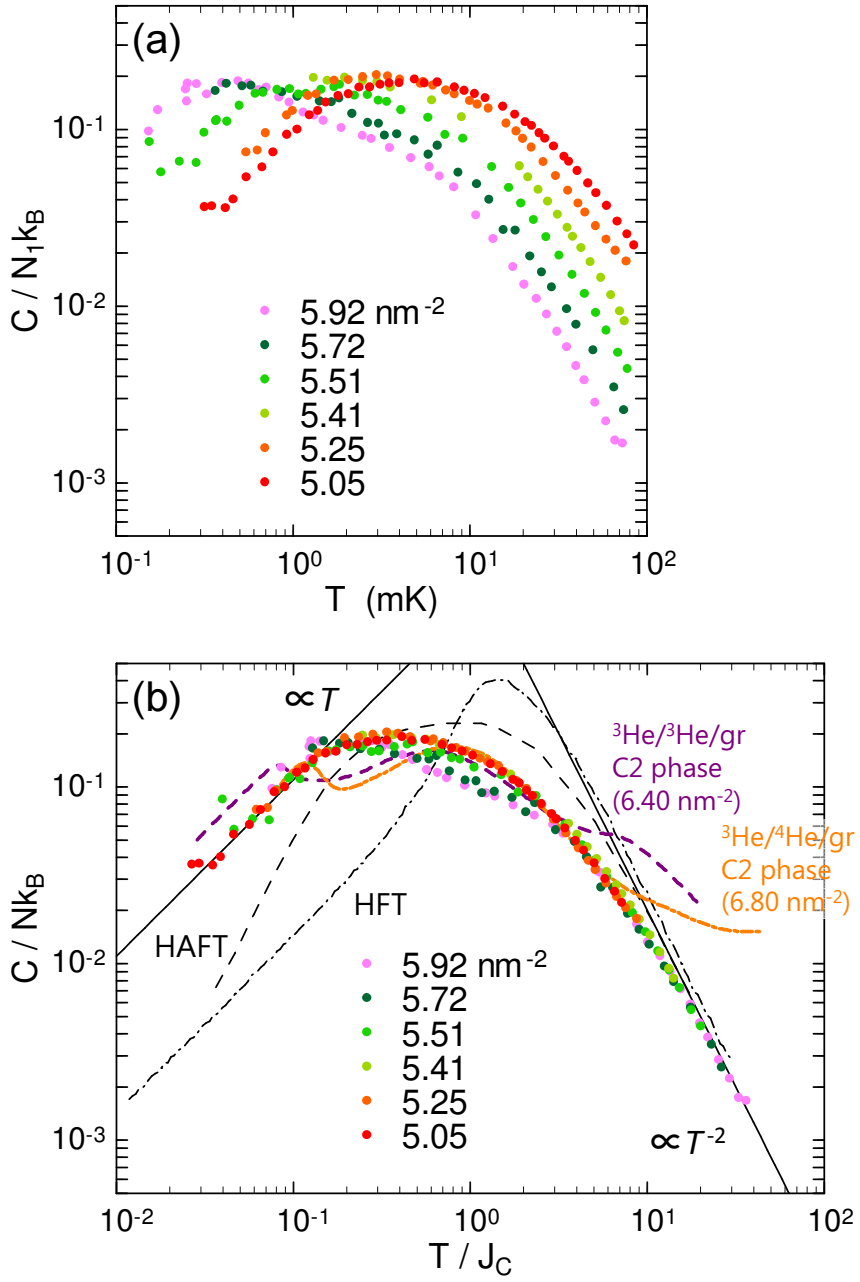

Fig. 5.4: (a) Temperature dependence of magnetic specific heat C/N_1K_B (N_1 is the number of ^{3}He atoms in the 1st layer on the HD) at $5.05 \leq \rho \leq 5.92$ nm^{-2} after subtracting the phonon or overlayer liquid contribution. (b) C/N_1K_B after subtracting the contribution from the 2D phonons as a function of temperature normalized by J_C., which has a $C \propto T$ dependence at $T/J_C < 0.15$, and $C \propto T^{-2}$ at $TJ_C > 20$. The temperature dependence of this universal curve is clearly different from that of the Heisenberg antiferromagnet on or ferromagnet on a triangular lattice [59]. The normalized specific heats of the C2 phases for ^{3}He/^{3}He/gr[6] and ^{3}He/^{4}He/gr[20] are also plotted for comparison.

where P_L and Q_M are polynomials and the subscripts represent the order of these polynomials. The fitted results are shown in Fig.5.3. The temperature range used for the fitted curves is $T > T'$, where T' is the temperature indicated by arrows. From these results and Eq.(2.12) we obtained the exchange interaction J_C; however, the MSE parameters cannot be reliably determined. We ploted the specific heat C/N_1k_B at $5.05 \leq \rho \leq 5.92$ nm^{-2} after subtracting the contribution from the 2D phonons or the overlayer liquid, where N_1 is the number of ^{3}He atoms in the 1st ^{3}He layer, in Fig.5.4 (a). All the data follow a universal curve when the specific heat data are plotted as a function of the normalized temperature T/J_C as shown in Fig.5.4 (b). The data at 5.92 nm^{-2} are well fitted to Eq.(5.3) rather than Eq.(5.1), so the fitted results of this data is described in Fig.5.7. The universal curve has a broad peak around $T/J_C \approx 0.4$ and $C \propto T$ behavior for $T/J_C < 0.1$. Especially, the data at 5.05, 5.25, and 5.41 nm^{-2} show good agreement with each other. The shape of the specific heat peak gradually changes at $\rho \geq 5.51$ nm^{-2}. The specific heat starts to decrease around $T/J_C \approx 1$, but at $T/J_C \leq 0.2$ it follows the universal curve again. Such a universal behavior is also reported by the previous magnetic susceptibility measurements on ^{3}He/HD/HD/gr at $5.02 \leq \rho' \leq 5.23$ nm^{-2} by Ikegami *et al.* [17]. They also reported this universal behavior changes between $\rho' = 5.23$ and 5.62 nm^{-2}, where ρ' is the corrected density obtained by considering the effect of the amorphous ^{3}He, so ρ' is not the same as the density reported in their original paper. The detail of the correction of the density scale is described in Appendix A.

The normalized specific heat of ^{3}He/HD/HD/gr is clearly different from the behaviors calculated from the HAFT and HFT models [59] shown as the dashed and dashed-dotted lines in Fig.5.4 (b), respectively. We also ploted the normalized specific heats of the C2 phases of ^{3}He/^{3}He/gr [6] (purple dashed line) and ^{3}He/^{4}He/gr [20, 36] (orange dashed-dotted line) in Fig.5.4 (b) for comparison. These data share some common features with ours, that is, the broad peak structure and the $C \propto T$ behavior below the peak. However the double peak structure of the C2 phases of the bilayer ^{3}He systems are different from the broad single peak of ^{3}He on a bilayer HD. The universality indicates that the ^{3}He film forms the uniform phase with substantial compressibility (at least $\Delta\rho/\rho = (5.92 - 5.05)/5.05 \approx 17\%$) larger than that of the C2 phase $\Delta\rho/\rho_{C2} \approx 9\%$ of ^{3}He/^{3}He/gr [16].

From the comparisons discussed above, we found common features between the specific heat of ^{3}He/HD/HD/gr at $5.05 \leq \rho \leq 5.92$ nm^{-2} and that of the C2 phases in the bilayer ^{3}He systems: The large compressibility and very broad peak structure. However, there is not clear evidence that the structure of the ^{3}He film on the HD in this density range is the same as that of the C2 phase. Therefore we call this phase the C2-like phase.

The large compressibility of the C2(-like) phase indicates that its structure is that of a QLC state with partially broken symmetry. One candidate is the hexatic phase which breaks the translational order but keeps the sixfold symmetry [103]. To detect such a structure, a neutron diffraction study is required. If the C2(-like) phase is truly the QLC state, its nuclear magnetism is not necessarily described by the localized spin models with crystalline structures. Although the MSE interactions are still important, due to the 1/2 magnetization plateau of the C2 phase of ^{3}He/^{4}He/gr in a magnetic field characteristic of the UUUD phase [104], the effect of the structural imperfection of the QLC state may explain the discrepancy between the MSE model and the C2(-like) phase. For example, if we assume the hexatic state, the interatomic distance has a distribution resulting in the

distribution of the exchange interactions. An exact diagonalization study of the random HAFT model in which the exchange interaction J at each bond is randomly distributed between $[J-\Delta, J+\Delta]$ gives the QSL state with $C \propto T$ behavior at low T [69].

entropy

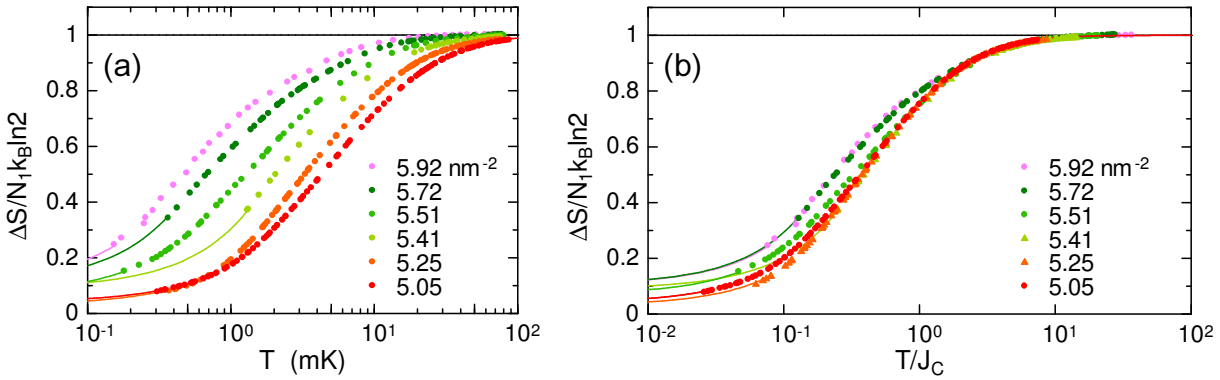

Fig. 5.5: (a) Entropy change calculated from the heat capacity data of the ^{3}He film in the C2-like phase. The data are normalized by the total spin entropy $N_1 k_{\rm B} \ln 2$. The solid lines are the extrapolation of the data assuming $C \propto T$ below the lowest measured temperature for all of the densities. (b) The entropy as a function of the normalized temperature $T/J_{\rm C}$. The data at 5.05 and 5.25 nm^{-2} release almost all of the total spin entropy (> 95 %), but at a higher density the entropy is not fully released within the temperature range of the measurements.

Figure 5.5 (a) shows the entropy change ΔS of the ^{3}He film deduced from the heat capacity data. The solid lines are the extrapolation of the data below the lowest temperature of the measurements assuming $C \propto T$ for all samples. At 5.05, 5.25 nm^{-2} ΔS is close to the total spin entropy $N_1 k_B \ln 2$. At densities greater than 5.41 nm^{-2}, the ΔS decreases slightly. At these densities the low temperature behavior may not be fully observed within the temperature region of the measurements because the specific heat shifts to low temperature as the density increase. The entropy as a function of normalized temperature $T/J_{\rm C}$ is also plotted in Fig.5.5 (b). The data at 5.04, 5.25, and 5.41 nm^{-2} fall onto the same curve, but at $\rho \geq 5.51$ nm^{-2} the data deviate from the curve.

2D phonon

Figure 5.6 shows the a_2 coefficients of the T^2 term in Eq.(5.1) for ^{3}He/HD/HD/gr, with those of the 1st layer incommensurate solid (IC1) phases of ^{3}He/gr [105] and ^{4}He/gr [105, 106], and the C2 phases of ^{3}He/^{3}He/gr and ^{4}He/^{4}He/gr [16]. The a_2 coefficients of the 1st layer systems have a strong density dependence and its Grüneisen parameters agree with those of the bulk solid ^{3}He when its effective areal density is expressed as $\rho_{\rm eff} = V^{2/3}$, where V is the volume of the bulk solid. The solid lines in Fig.5.6 are the power law fittings of the data of the IC1 phases of ^{3}He/gr and ^{4}He/gr produced by Hering [105]. The a_2 coefficient of the C2-like phase of ^{3}He/HD/HD/gr is smaller than the

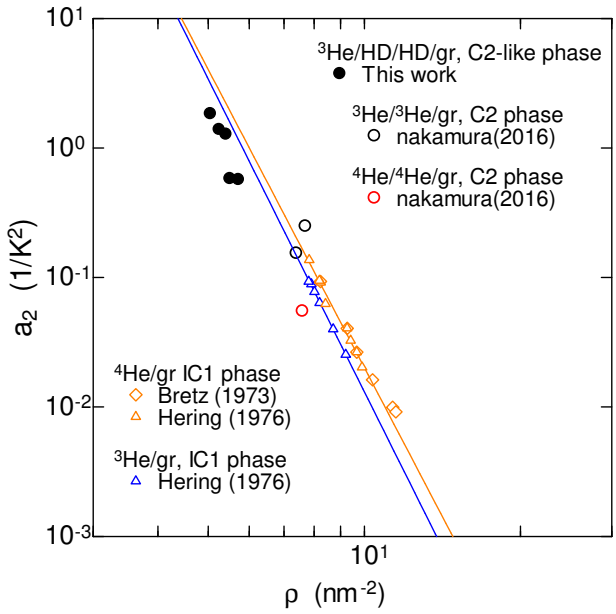

Fig. 5.6: The a_2 coefficient of the $C \propto T^2$ term in Eq.(5.1) of helium films on graphite as a function of the density ρ. The black solid circles are the data of the C2-like phase in this work. The black and red open circles are the data of the C2 phases of ^{3}He/^{3}He/gr and ^{4}He/^{4}He/gr , respectively [16]. The orange triangles[105] and diamonds [106] are the IC solids of ^{3}He/gr, and the blue triangles are the IC solid of ^{4}He/gr [105]. The solid lines are the power law fitting of the data from Ref.[105].

extrapolation of these solid lines. When the a_2 coefficients of the C2-like and C2 phases of ^{3}He/^{3}He/gr are assumed to be in the same phase, they have a weaker density dependence than the 1st layer cases. Such a reduction is possible in the QLC state, because the partial order may reduce the number of the phonon modes.

C2-like phase after layer promotion

The heat capacity data at $5.92 < \rho < 7.15$ nm^{-2} will now be discussed. At $\rho \geq 5.92$ nm^{-2} the heat capacity at $T \gtrsim 10$ mK demonstrates a clear increase and satisfies the $C \propto T$ dependence. This increase is clear evidence of the promotion to the 2nd layer (or 4th layer including HD layers) and the T-linear heat capacity is the contribution from the liquid ^{3}He on the topmost layer. Therefore we fitted the data to

$$C = Nk_{\mathrm{B}}P[2,2] + \gamma T - \alpha T^2, \tag{5.3}$$

where the last two terms in the right hand side represent the contribution from the liquid ^{3}He in the 2nd layer on the HD. The fitted results are shown in Fig.5.7. The temperature range used for the fit is described in the same way as in Fig.5.3. The black dashed and blue dashed-dotted lines represent the magnetic and liquid contributions. The density where the layer promotion occur ($\rho_{\mathrm{promotion}}$) is estimated at 5.7 nm^{-2}, which is smaller than that of ^{3}He/^{3}He/gr and ^{3}He/^{4}He/gr ($\rho_{\mathrm{promotion}} \approx 6.8$ nm^{-2}). The difference can be explained by the difference in the average confinement potential of the ^{3}He/HD/HD/gr and ^{3}He/^{3}He/gr

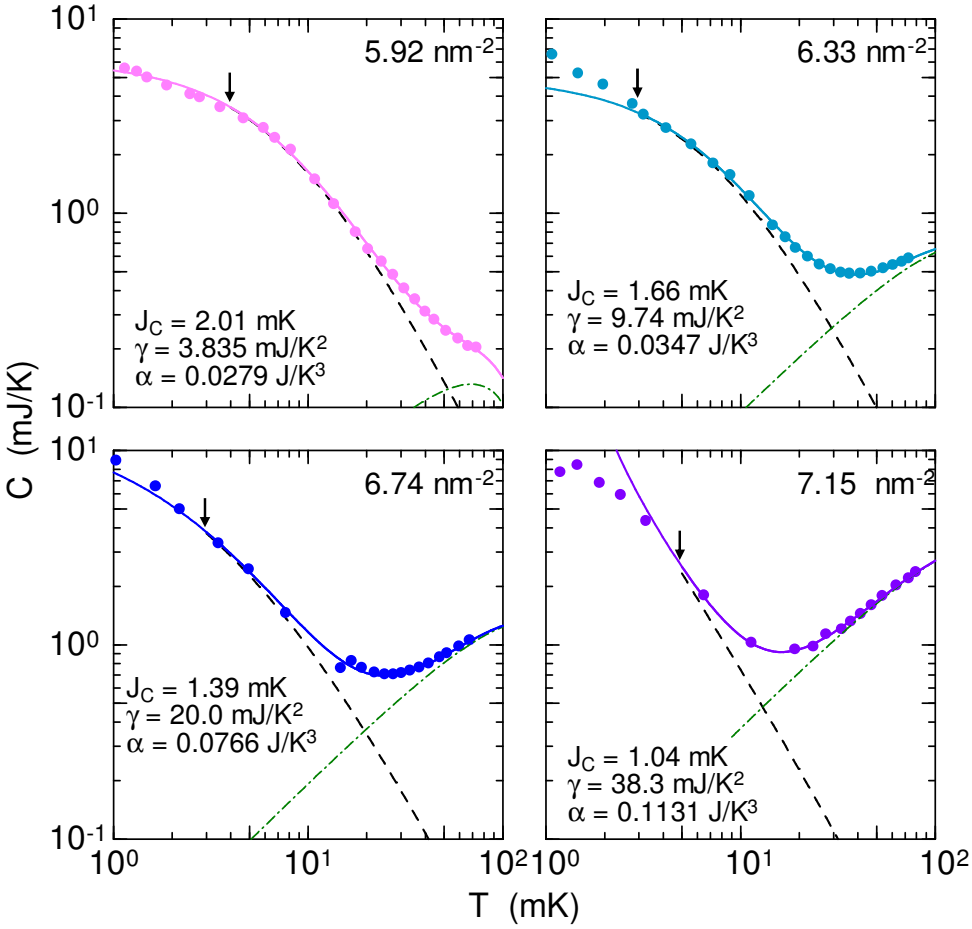

Fig. 5.7: Heat capacity data at 5.92, 6.33, 6.74, and 7.15 nm^{-2} and the fitted curve using Eq.(5.3). The T ranges used for the fit are described in the same way as in Fig.5.3. The black dashed and blue dashed-dotted lines represent the magnetic and overlayer liquid (puddle) contributions, respectively.

system [22]. Since the confinement potential is smaller for ^{3}He/HD/HD/gr, the layer promotion is easier.

Growth of the ferromagnetic peak

After the layer promotion occurred, the high T heat capacity started to increase, although the heat capacity in the mid T region ($5 \leq T \leq 10$ mK) did not significantly change. The latter behavior indicates that the C2-like phase is nearly fully compressed, so the former behavior should not be understood as the contribution from the C2-like phase. The increase of the heat capacity at low T after the layer promotion is also observed in ^{3}He/^{4}He/gr system [58], which may be explained by an emergent ferromagnetic component. The heat capacity data at $6.33 \leq \rho \leq 7.15$ nm^{-2} after subtracting the heat capacity at 5.92 nm^{-2} are shown in Fig.5.8 (a). The coincidence of the growth of the ferromagnetic component and the layer promotion indicates that this ferromagnetism is caused by the indirect RKKY type interactions between the 1st layer localized ^{3}He and

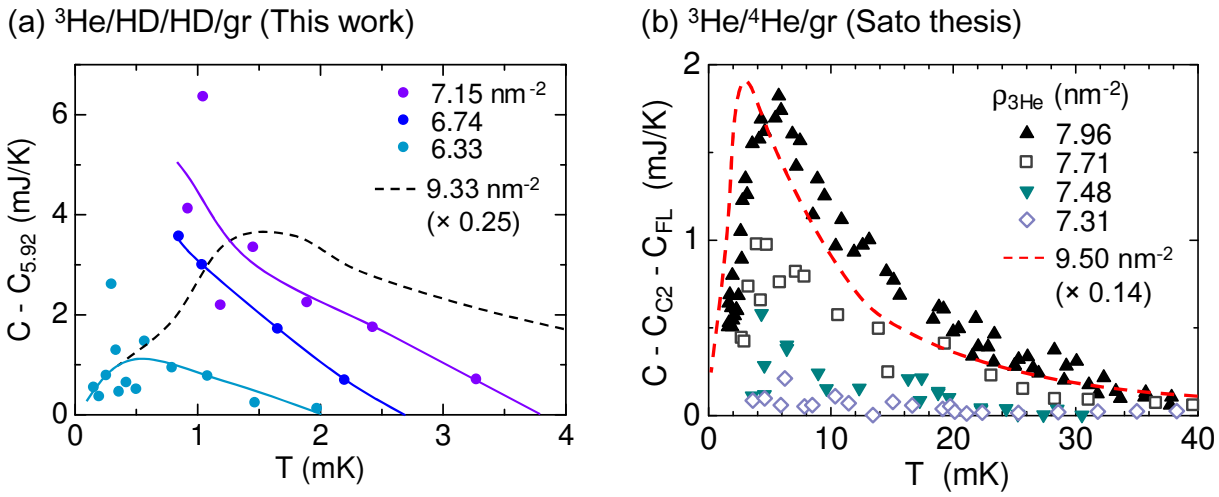

Fig. 5.8: (a) Heat capacity data of 6.33, 6.74, and 7.15 nm^{-2} from which the heat capacity of 5.92 nm^{-2} is subtracted. The black dashed line represents the data at 9.33 nm^{-2}, where the ^{3}He film is in the ferromagnetic IC2 phase, whose magnitude is multiplied by 0.25. (b) The excess heat capacities of the C2 phase of ^{3}He/^{4}He/gr after the layer promotion, from which the contributions of the C2 phase and the overlayer liquid are subtracted. The dashed line shows the ferromagnetic peak of the IC2 phase ($\rho = 9.50$ nm^{-2}), whose magnitude is multiplied by 0.14.

the overlayer liquid ^{3}He [107]. Figure 5.8 (b) shows the excess heat capacity of the C2 phase of ^{3}He/^{4}He/gr after subtracting the contribution from the C2 phase and overlayer liquid. The excess heat capacity has a peak and the peak temperature $T_{\rm peak}$ is close to that of the lowest density IC2 phase (9.50 nm^{-2}, the red dashed line in the figure). Conversely, the $T_{\rm peak}$ of $C_{6.33} - C_{5.92}$ of ^{3}/HD/HD/gr is smaller than 9.33 nm^{-2} (the black dashed in the figure; the magnitude is multiplied by 0.25). $T_{\rm peak}$ at 6.74 and 7.15 nm^{-2} are at lower than 0.8 mK. Since $J_{\rm C}$ is expected to decrease at higher densities due to the compression, the density of the emergent ferromagnetic component appears to be greater than the smallest density of the IC2 phase. However, in the case of ^{3}He/HD/HD/gr, the compression of the C2-like phase continues even after the layer promotion and it is difficult to separate the ferromagnetic contribution from that of the C2-like phase.

Comparison with the previous measurement

In Fig.5.9, we compare the heat capacity data of the C2-like phase, including the contributions from the 2D phonons and the overlayer liquid, with those of the^{3}He/HD/HD/gr taken by Casey *et al.* [18] down to $T = 0.8$ mK. In Fig.5.9 (a), the Casey density scales are clearly inconsistent with that in this work. The data in this work at 5.05 nm^{-2} are similar to the data at 5.4 nm^{-2} in Ref.[18]. The data at similar densities are plotted in similar colors. Note that the density of Ref.[18] is the nominal one including amorphous ^{3}He. The density scales of both measurements are seemingly consistent if the densities in Ref.[18] are multiplied by 0.93, as shown in Fig.5.9 (b). If we assume a difference in the

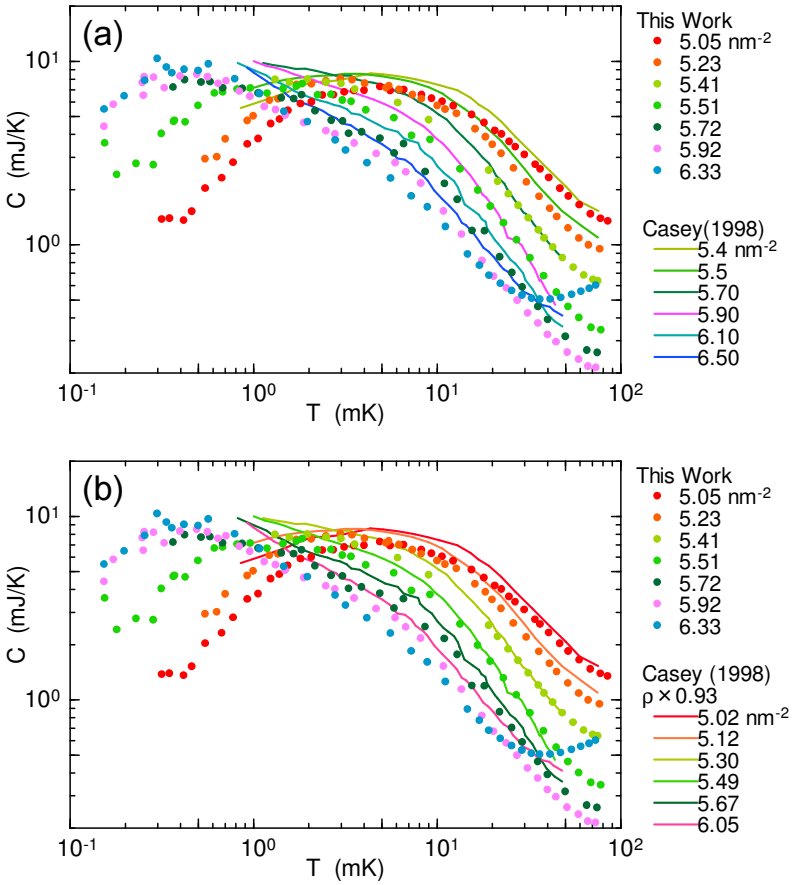

Fig. 5.9: Comparisons between the heat capacity data of the ^{3}He samples in the C2-like phase and the previous heat capacity measurements of ^{3}He/HD/HD/gr (Ref.[18]) using two different density scales. (a) The density scale as reported in Ref.[18] is the nominal one that includes the density of amorphous ^{3}He. (b) The density scale multiplied by 0.93. The data at similar densities are plotted in similar colors. The latter scale shows good agreement with the data in this work at $T > 3$ mK.

density scale of $\approx 7\%$ corresponding to the amount of amorphous ^{3}He in Ref.[18], it is estimated to be about 0.4 nm^{-2}. They claimed that the ^{3}He film forms the commensurate solid at 5.4 - 5.5 nm^{-2}. These densities become 5.02 - 5.12 nm^{-2} if multiplied by 0.93, corresponding to the formation of the C2-like phase. They also claimed that the heat capacity peak becomes narrower at 5.7 nm^{-2}, and above this density the heat capacity data show power law behavior which may be relevant to the phase transition or the structural disorder. However, as discussed above, the measurements in this work down to $T = 0.2$ mK revealed that all of the ^{3}He samples plotted in Fig.5.9 are in the highly compressible C2-like phase, which is confirmed by the scaling behavior (see Fig.5.4). The layer promotion density $\rho_{\rm promotion}$ is reported as 6.8 nm^{-2} in Ref.[18], which becomes 6.32 nm^{-2} when multiplied by 0.93. This value is still greater than $\rho_{\rm promotion} \approx 5.7$ nm^{-2} obtained in this work. However, the heat capacity in Ref.[18] at 6.05 nm^{-2} (in the density scale after the correction) shows the weaker decrease at $T > 20$ mK than those at 5.67 nm^{-2}. This indicates the existence of the small overlayer liquid component. If so, the promotion

density is between $5.67 < \rho < 6.05$ nm^{-2}, which is consistent with our data.

5.2 Incommensurate solid phase ($9.33 \leq \rho \leq 13.63$ nm^{-2})

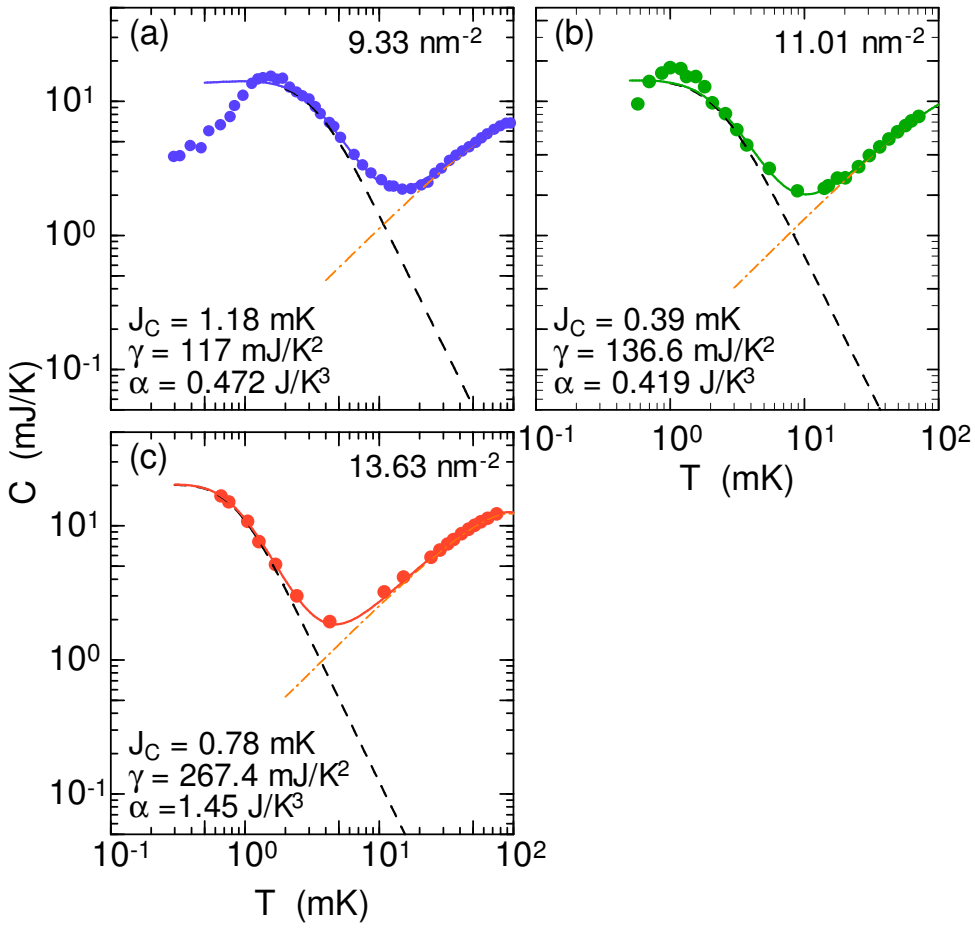

Fig. 5.10: Heat capacity data at 9.33, 11.01, and 13.63 nm^{-2} and the fitted curve using Eq.(5.3). The black dashed and orange dashed-dotted lines are the magnetic and overlayer liquid contributions, respectively.

The heat capacities of the ^{3}He sample at the three highest densities (9.33, 11.01, and 13.63 nm^{-2}) are shown in Fig.5.10. The heat capacity data have a peak around $T_{\rm peak} =$ 1.5 mK at 9.33 nm^{-2}, before shifting lower as the density increases. These peaks are narrower than those of the C2-like phase. At 9.33 nm^{-2}, a $C \propto T$ dependence is observed below the peak, near $T < 0.8$ mK. For $T > 20$ mK, the heat capacity increasse almost linearly with T, corresponding to the Fermi liquid heat capacity of the ^{3}He overlayer. All these features agree with the heat capacity of the 2nd layer incommensurate solid (IC2) phases of ^{3}He/^{3}He/gr [6, 25, 57] and ^{3}He/^{4}He/gr [37] (see Sec.2.2), whose magnetic ground state is ferromagnetically ordered. The $C \propto T$ behavior at low T is due to the 2D ferromagnetic spin wave excitations. The previous magnetic susceptibility measurements

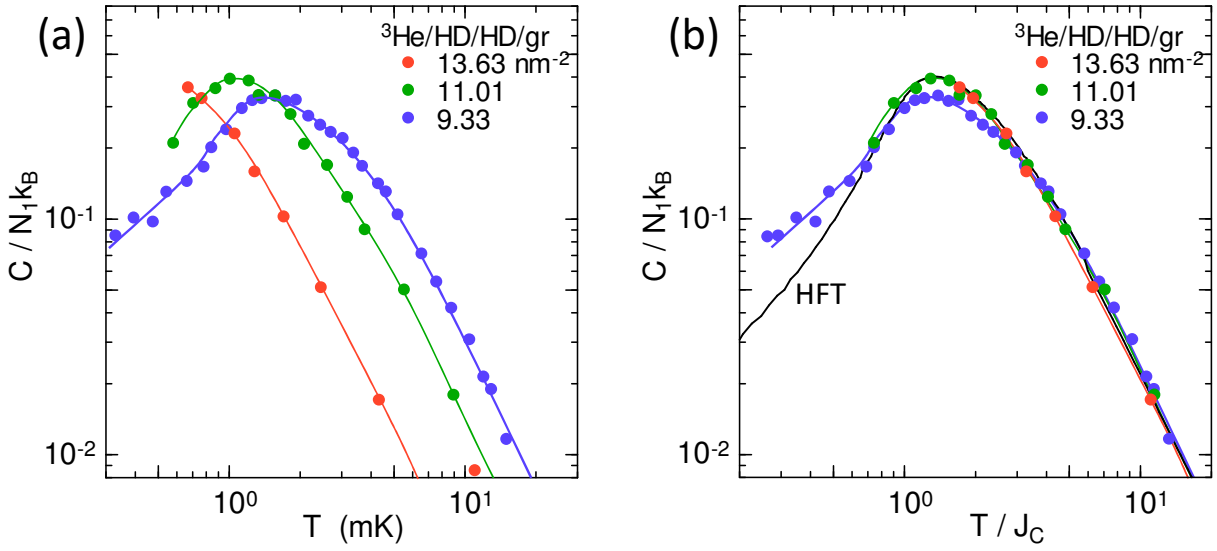

Fig. 5.11: (a) Specific heats C/N_1k_B for 9.33, 11.01 and 13.63 nm^{-2}. T_{peak} shifts to low T as the ^{3}He film is compressed by the increasing density. The solid lines are guides to the eye. (b) C/N_1k_B vs. the normalized temperature. As the density increases, C/N_1k_B is similar to the theoretical calculation of the HFT model [82], shown as the black solid line. Note that N_1 is the number of ^{3}He atoms derived from spin entropy at 9.33 m^{-2}, and the same N_1 was used for all of the data.

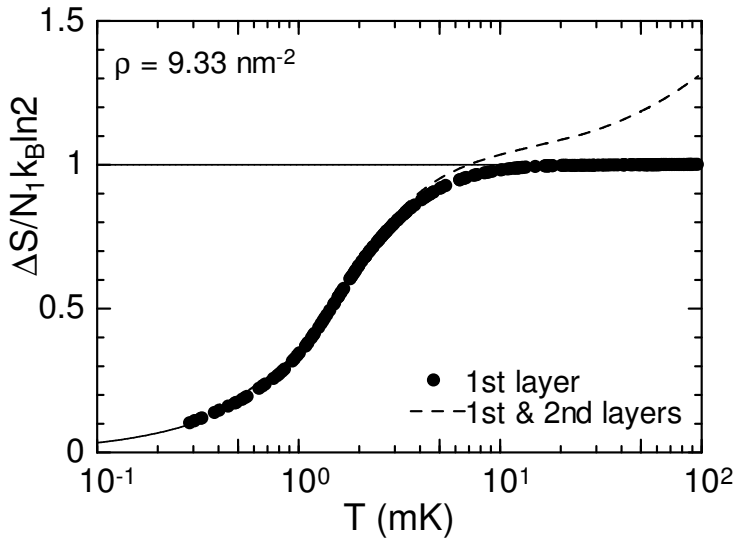

Fig. 5.12: Spin entropy of the 9.33 nm^{-2} data calculated from the measured heat capacity. The black circles and dashed lines represent the entropies of the 1st layer IC solid and total . Dashed line represents the entropy of total ^{3}He, respectively. The solid line shown below $T = 0.3$ mK represents the $C \propto T$ dependence. The N_1 estimated from this entropy change corresponds to 5.87 nm^{-2}.

of ^{3}He/HD/HD/gr show that the exchange interaction is ferromagnetic at $\rho \geq 9.7$ nm^{-2} [17]. We fitted the data to Eq.(5.3) to extract the spin contribution. The fitted results are shown in Fig.5.10. Figure 5.11 (a) shows the specific heat C/N_1k_B of the IC phase of ^{3}He/HD/HD/gr. At $T \gg T_{peak}$ the specific heats satisfies $C \propto T^{-2}$ as expected for localized spin systems. T_{peak} shifts to lower temperatures with increasing density, because the ^{3}He film is compressed. The specific heat as a function of the normalized temperature T/J_C is plotted in Fig.5.11 (b). The theoretical calculation of the HFT model [59] is also shown here as the black solid line. The temperature dependence of the specific heat of ^{3}He/HD/HD/gr approaches the calculated one based on the HFT model as the density increases. Such a tendency is consistent with the IC2 phases of the bilayer ^{3}He systems [37, 57] and the 2D MSE model [53] which predicts that J_3 is dominant for the high densities.

Figure 5.12 shows the normalized entropy change $\Delta S/N_1k_B \ln 2$ deduced from the measured heat capacity at 9.33 nm^{-2} after subtracting the liquid contribution. The solid line is the extrapolation assuming $C \propto T$. The entropy change deduced from the total heat capacity, including that of the overlayer liquid, is shown as the dashed line. In the IC phase, estimating the 2nd layer density ρ_2 from the γ coefficient of the overlayer liquid heat capacity is difficult because for such high densities the ^{3}He on the topmost layer is not the liquid puddle but the uniform Fermi liquid, so there is no criterion for estimating ρ_2 from γ. Therefore we tried to estimate N_1 from the entropy change in Fig.5.12. N_1 deduced in this way corresponds to 5.87 nm^{-2}, which is used to calculate the specific heat mentioned above. N_1 obtained from the data at 9.33 nm^{-2} is also used for the data at 11.01 and 13.63 nm^{-2}, because the lowest temperatures of the measurements are not enough to calculate the total entropy. Therefore N_1 may be underestimated by approximately 10 % for the data at 13.63 nm^{-2}. The obtained N_1 roughly corresponds to $\rho_{promotion}$ and is smaller than expected. The IC2 phase of ^{3}He/^{4}He/gr also displayed a smaller than the expected entropy change from the theoretical calculation [37]. The number of atoms of the IC2 phase estimated from ΔS of ^{3}He/^{4}He/gr is smaller by approximately 18 % compared with the theoretically calculated 2nd layer density [14]. The origin of this entropy reduction is not understood at present.

Density variation of J_C

Figure 5.13 summarizes the J_C values obtained by the fitted heat capacity data of ^{3}He/HD/HD/gr as a function of the density. In the plot, the horizontal axis is the ρ_1 density of the 1st ^{3}He layer on the HD. The quantum phase diagram of ^{3}He/HD/HD/gr is also shown in the upper panel.

We also plotted J_C of ^{3}He/^{3}He/gr[6, 57], and ^{3}He/^{4}He/gr[20, 58], as well as the $|J_\chi|$ values in ^{3}He/HD/HD/gr [17], in Fig.5.13. $|J_\chi|$ is the absolute value of the exchange interactions calculated from the Curie-Weiss temperature and Eq.(2.14). Note that the density scale of the data in Ref.[17] is corrected (see Appendix A), and the data of the bilayer ^{3}He systems are plotted as a function of the 2nd layer density.

There are large inconsistencies in the behavior of J_C of the C2(-like) and IC(2) phases of the ^{3}He/HD/HD/gr and bilayer ^{3}He systems. Compared with the extrapolation of J_C of the IC(2) phases, J_C of the C2(-like) phases are strongly suppressed by at least one order of magnitude. This means that the C2(-like) phases are clearly distinguishable from

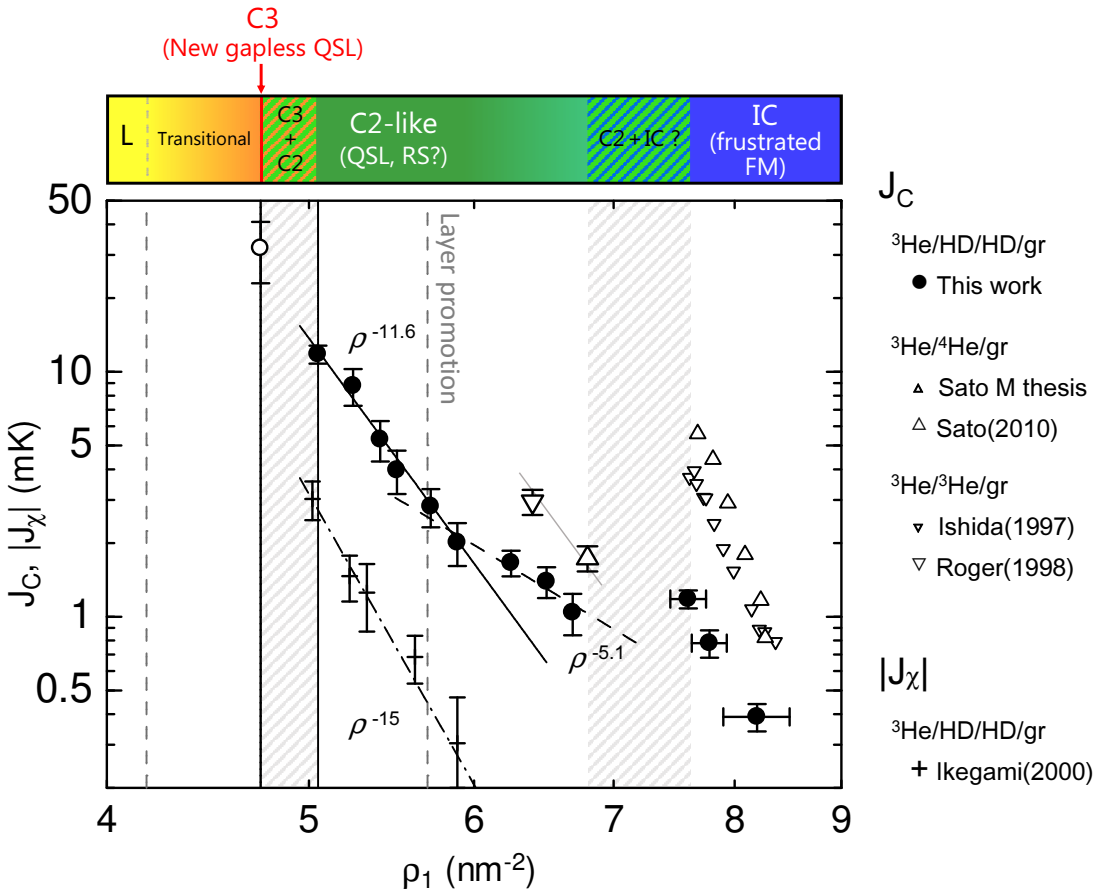

Fig. 5.13: Exchange interactions J_C and $|J_\chi|$ deduced by the measured specific heat or the magnetic susceptibility data as a function of ρ_1. ρ_1 is the density of the 1st ^{3}He layer of the ^{3}He/HD/HD/gr system and that of the 2nd layer for the bilayer ^{3}He systems. The plotted series are the J_C values with the symbols representing: ^{3}/HD/HD/gr for this work (black filled circle); C2 phase of ^{3}/^{4}He/gr (large triangle) (Ref.[108]); C2 phase of ^{3}/^{3}He/gr (large inverse triangle) (Ref.[6]); IC2 phase of ^{3}/^{4}He/gr (small triangle) (Ref.[37]); IC2 phase of ^{3}/^{3}He/gr (small inverse triangle) (Ref.[57]). Note that the data of the bilayer ^{3}He systems are plotted as a function of the 2nd layer density. The + symbols are the $|J_\chi|$ values of ^{2}He/HD/HD/gr (Ref.[17]). Its density scale is corrected by Eq.(A.2) (see Appendix A).

the IC(2) phases and the C2(-like) phases are affected by the corrugation potential of the substrate.

J_C and $|J_\chi|$ of ^{3}He/HD/HD/gr differ by a factor of ≈ 5. This is reasonable because the magnetism of the ^{3}He monolayer cannot be explained by a single exchange interaction J as mentioned in Sec.2.3.2. The difference between J_C and $|J_\chi|$ is also observed in the bilayer ^{3}He system [57].

The obtained J_C shows a strong density dependence at $5 < \rho < 6$ nm^{-2}, as observed in the previous studies [17, 18, 21]. J_C is reduced by a factor of 5 from 5.05 to 5.92 nm^{-2}.

The power law fitting of the data in this density region yields

$$\frac{\mathrm{d}\ln J_{\mathrm{C}}}{\mathrm{d}\ln \rho} = 11.6 \pm 1.5. \tag{5.4}$$

The gray solid line drawn near the data points of the C2 phases has the same slope of Eq.(5.4).This Grüneisen constant is smaller compared with $|J_\chi| \propto \rho^{-15}$ [17]. The density dependence of J_{C} becomes weaker after the layer promotion occurs because the C2-like phase is almost fully suppressed. The Grüneisen constant $\mathrm{d}\ln J_{\mathrm{C}}/\mathrm{d}\ln\rho$ is -5.1; approximately half of that before layer promotion. For the data at $5.92 \leq \rho \leq 7.15$ nm^{-2}, ρ_1 is calculated as $\rho_1 = \rho - \rho_2$ where ρ_2 is the density of the 2nd layer liquid. Judging from the magnitude of the γ coefficient, the 2nd layer liquid is in the self-condensed liquid, rather than the uniform liquid spreading over the whole surface of the substrate. As will be discussed in Sec.2.4.2, the density of the puddle phase is not strongly affected by the potential corrugation from the substrate, so ρ_{liquid} can be estimated using the relationship between γ and ρ of the 1st layer puddle on a bilayer HD shown in Fig.8.2. The resultant ρ_1 values are listed in Table.5.1

ρ (nm^{-2})	5.92	6.33	6.74	7.15
ρ_1 (nm^{-2})	5.89	6.25	6.50	6.69

Table 5.1: Listed densities of the 1st ^{3}He layer ρ_1 after the layer promotion.

For the IC2 phases in ^{3}He/^{3}He/gr and ^{3}He/^{4}He/gr, where the layer promotion has already occurred, ρ_1 is estimated from the total ^{3}He density and the theoretical calculation by Roger [14]. The ρ_1 values of ^{3}He/HD/HD/gr in this work is also determined by this calculation, assuming that the structure of the IC solid is less sensitive to the potential corrugation of the substrates.

5.3 Conclusion

We measured the magnetic specific heat of compressible phases, namely the C2-like and IC phases. The magnetic specific heat of the C2-like phase has a very broad peak around $T/J_{\mathrm{C}} = 0.4$, and $C \propto T$ at low T. The specific heat over a wide range of the density ($\rho =$ 5.05 - 5.9 nm^{-2}, $\Delta\rho/\rho_{\mathrm{C2like}} \approx$17%) follow the same curve. Such a scaling behavior suggest the uniform compressible quantum phase. These features are consistent with those of the C2 phases of bilayer ^{3}He systems. To understand the magnetism of this phase, not only the MSE interactions, but also the effects of the lattice disorder are seemingly important.

After the layer promotion at $\rho \approx 5.7$ nm^{-2}, compression of the C2-like phase is suppressed, but there is a low T ($T < 5$ mK) heat capacity increase related to the emergence of the ferromagnetism. This ferromagnetism, which starts to grow at the density where the layer promotion occur, can be thought to be caused by the indirect RKKY interactions via the liquid ^{3}He on the topmost layer.

In the IC solid phase at the highest density region ($\rho > 9.3$ nm^{-2}), the ferromagnetic specific heat is similar to that of the IC2 phases of the bilayer ^{3}He systems. The temperature dependence of the specific heat was similar to that of the HFT model. This behavior

is also consistent with that of the IC2 phases of the bilayer ^{3}He systems and theoretical calculation of the 2D MSE model.

Chapter 6

A new quantum phase between the liquid and C2-like phases: C3 phase

6.1 Successive phase transitions ($4.18 \leq \rho \leq 5.05$ nm^{-2})

In this chapter, we discuss the results of heat capacity measurements on the ^{3}He/HD/HD/gr system at $4.2 \leq \rho \leq 5$ nm^{-2}, shown as the colored region in Fig.6.1.

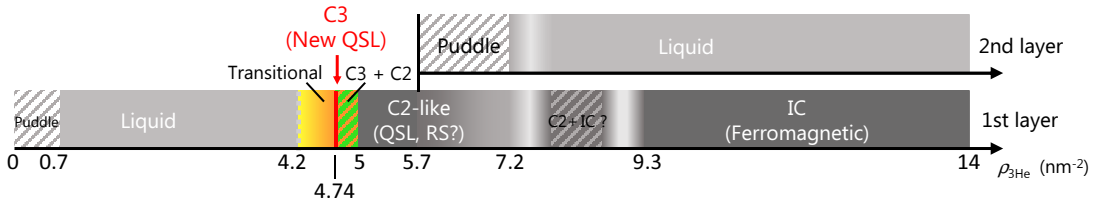

Fig. 6.1: Phase diagram of ^{3}He/HD/HD/gr. The shaded region is discussed in this chapter.

The heat capacity data up to $\rho = 4.18$ nm^{-2} followed the relationship $C \propto T$ at low T, which is characteristic of a Fermi liquid. However, the data for higher densities deviated from this behavior. This indicates that the ^{3}He film started to solidify and the spin heat capacity emerged. We fitted the low T part of the heat capacity data at $3.45 \leq \rho \leq 5.92$ nm^{-2} to $C = aT^n$ where a and n are the fitting parameters. The fitted results and n obtained from the fitting are shown in Fig.6.2. At 3.45 and 4.18 nm^{-2}, n was close to unity, because the ^{3}He monolayer was in the Fermi liquid phase. As the density increases, n displayed a U-shaped anomaly, with the minimum value $n = 0.64 \pm 0.03$ at 4.74 nm^{-2}. n increased above 4.74 nm^{-2}, before returning to unity at 5.05 nm^{-2}. Therefore, the phase transitional region was at $4.18 \leq \rho \leq 5.05$ nm^{-2}, with the singular point at 4.74 nm^{-2}.

Figure 6.3 shows the heat capacities at fixed temperatures in the transitional region. Between 4.74 and 5.05 nm^{-2} (the density region sandwiched by the two vertical solid lines in the figure) the heat capacity isotherm linearly changed with the density at all temperatures, and was constant at $T = 11$ mK. These are typical features of macroscopic

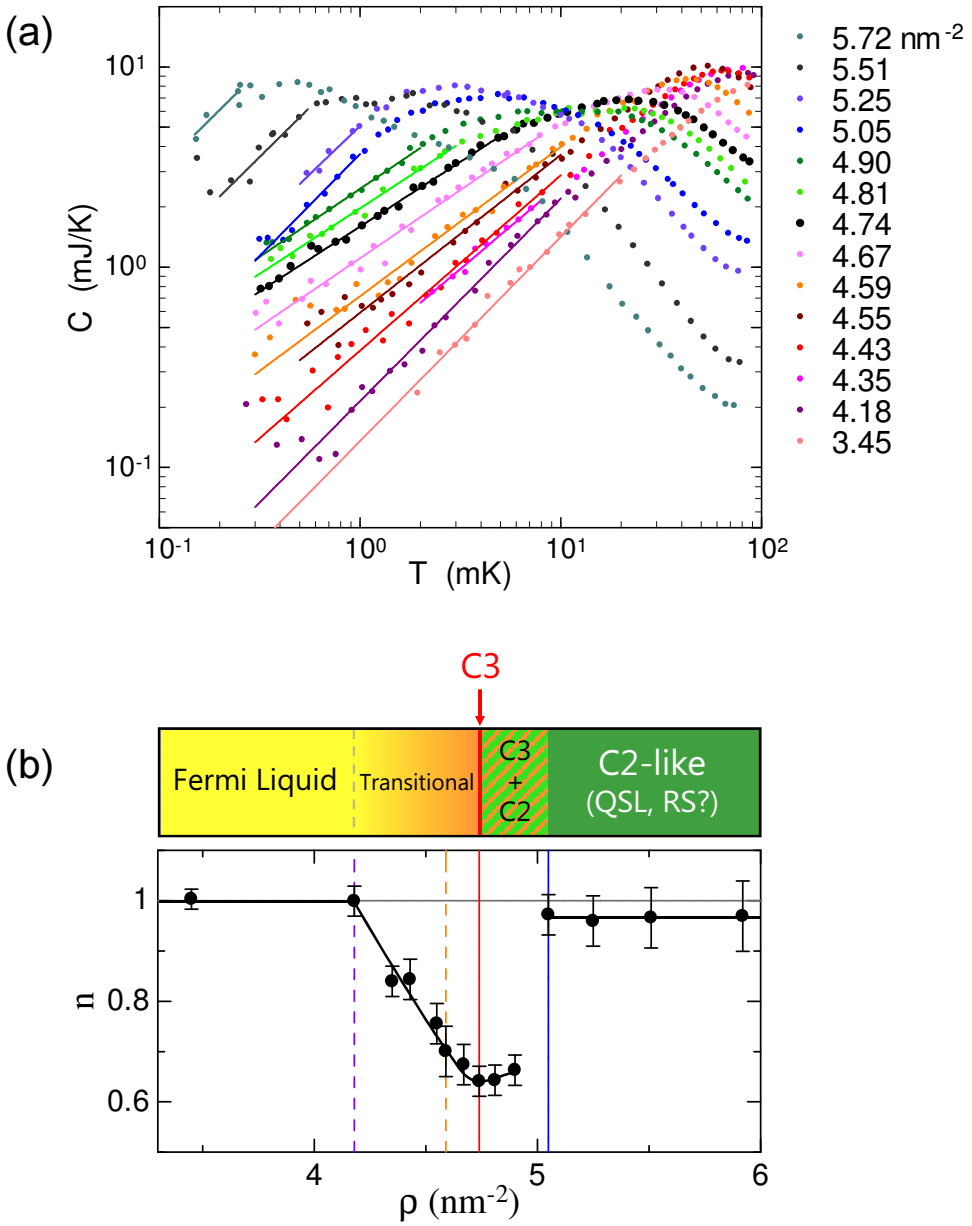

Fig. 6.2: (a) Power law fitting of the data at 4.18 to 5.92 nm^{-2} at low T. The temperature ranges of the solid lines were used for the fitting. (b) The power was deduced by fitting the low T heat capacity data to $C = aT^n$. The fitting parameter n shows a U-shaped anomaly with a minimum of $n = 0.64 \pm 0.03$ at 4.74 nm^{-2}. The solid lines correspond to the boundary of the two phase coexistence regions between the C3 and C2-like phases. The dashed lines indicate the onset of the phase transition (4.18 nm^{-2}) and the density where the behaviors of the high T heat capacity isotherms change (4.59 nm^{-2}, see Fig.6.3)

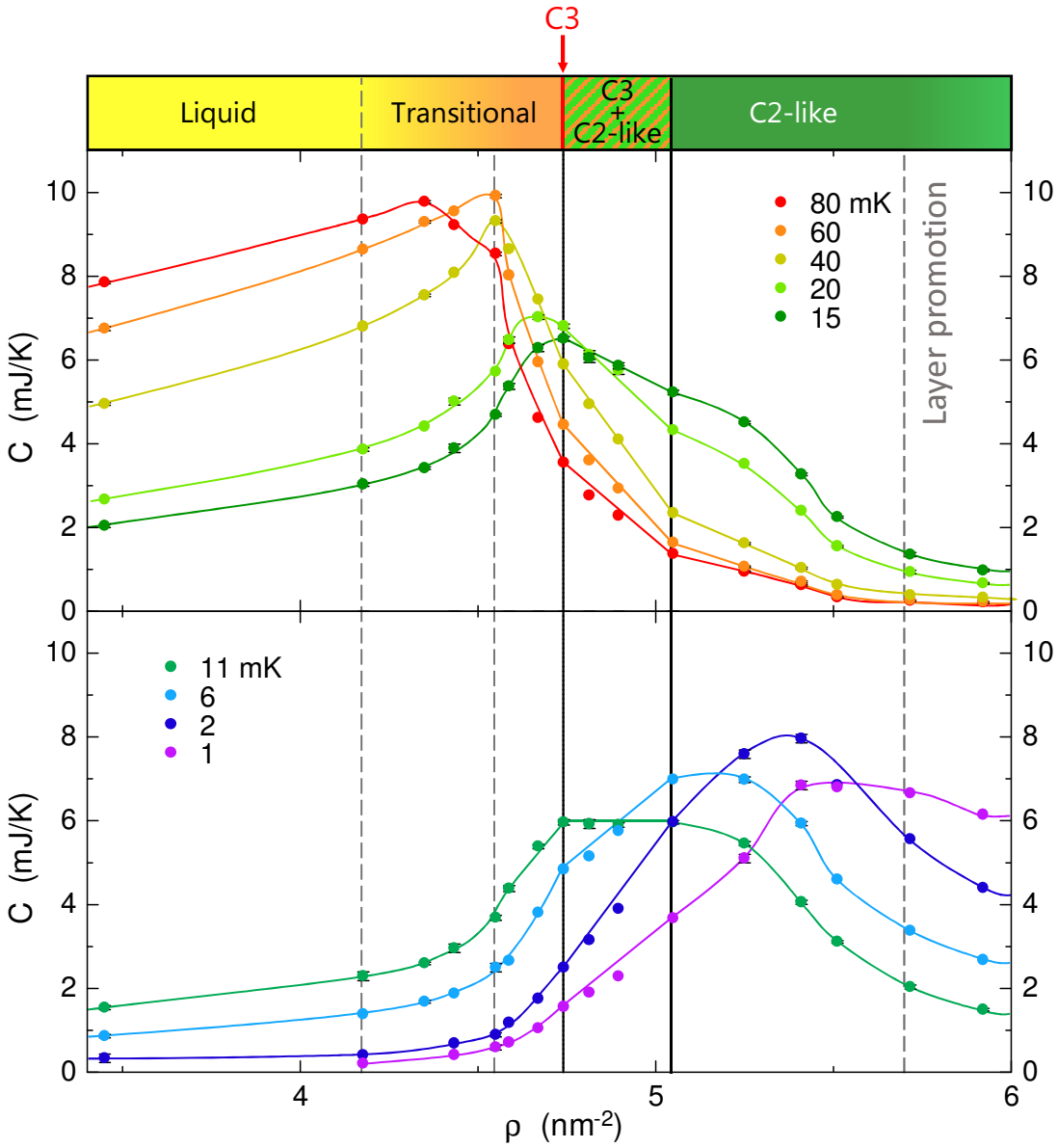

Fig. 6.3: Heat capacity isotherms at selected temperatures. At 4.74 $\leq \rho \leq$ 5.05 nm^{-2}, indicated by the two vertical solid lines, the heat capacity changed almost linearly with density, and become constant at $T = 11$ mK, indicating a two phase coexistence (1st order phase transition). The dashed line at 4.18 nm^{-2} indicates the onset of the phase transition. The dashed line at 4.59 nm^{-2} indicates the density where the behavior of the high T heat capacity changed.

two phase coexistence, or in other words, the 1st order phase transition where the low and high density phases are spatially separated. To confirm the scenario of two phase coexistence, we checked whether the heat capacities at the intermediate densities can be expressed as the linear combination of the data at the phase boundaries.

We fitted the data at 4.81 and 4.90 nm^{-2} to

$$C = (1 - x)C_{4.74} + xC_{5.05} \tag{6.1}$$

where $C_{4.74}$ and $C_{5.05}$ are the heat capacities of 4.74 and 5.05 nm^{-2}, respectively, and x is the fraction of the 5.05 nm^{-2} component. The fitted results are shown as the dashed lines in Fig.6.4 (a). The heat capacity data at the intermediate densities were reasonably reproduced by the linear combination of the heat capacities of the pure phases. x increases linearly with the density as shown in the inset. These results agree with the scenario of the 1st order phase transition. The heat capacities of 4.74, 4.81, 4.90, and 5.05 nm^{-2} cross at one point ($T \approx 11$ mK, $C \approx 6$ mJ/K), which is indicated by the red arrow in Fig.6.4 (b). The existence of such a crossing point is also the typical feature of two phase coexistence. Conversely, the heat capacities of 4.59, 4.67, and 4.74 nm^{-2} do not cross at one point as indicated by the two red arrows in Fig.6.4 (b). Therefore the details of the phase transition below 4.74 nm^{-2} cannot be interpreted as a simple two phase coexistence. At $\rho > 4.18$ nm^{-2}, although n deviates from unity as mentioned above, the divergence of the low T heat capacity is still observed at $T \leq 40$ mK and up to ~ 4.55 nm^{-2} as shown in Fig.6.3. Above 4.55 nm^{-2}, the high T ($T \geq 40$ mK) behavior changes sharply. Although the detail of the transition is not clear, it may be divided into two stages.

We found the solidification of the ^{3}He film above 4.18 nm^{-2} indicated by the low T specific heat deviating from $C \propto T$. At 4.74 nm^{-2} the anomalous behavior of the specific heat is observed, which will be discussed in the next section. Above this density, the 1st order phase transition occurred. These experimental findings suggest that there is a distinct phase in the vicinity of 4.74 nm^{-2}. Hereafter we call this new phase "C3 phase". The structure of the C3 phase is most likely the commensurate phase, judging from its weak compressibility $\Delta\rho/\rho_{C3} < 2\%$ compared with the C2(-like) phases. Therefore it is probably the "true" commensurate phase. The density ratio of the ^{3}He layer to the HD layer is $4.74/9.2 = 0.515$. This value is smaller than $4/7$ ($= 0.5714$) previously reported.

The existence of the C3 phase supports the claim that the C2(-like) phase is not truly the commensurate solid but the QLC. The reason why the C3 phases is realized only in the ^{3}He/HD/HD/gr system is assumed to be due to the difference in the substrate potentials. According to Fig.2.6, the potential corrugation of a bilayer HD on graphite is nearly three times as large as that of a monolayer ^{3}He on graphite, and therefore the wave function of ^{3}He on HD is more strongly localized than on ^{3}He. This tendency is consistent with the experimental results.

We revealed that the quantum phase diagram of ^{3}He/HD/HD/gr is qualitatively different from the bilayer ^{3}He systems and found the commensurate solid at the unexpectedly low density. Therefore the theoretical study of the ^{3}He monolayer on Hydrogen is strongly desired.

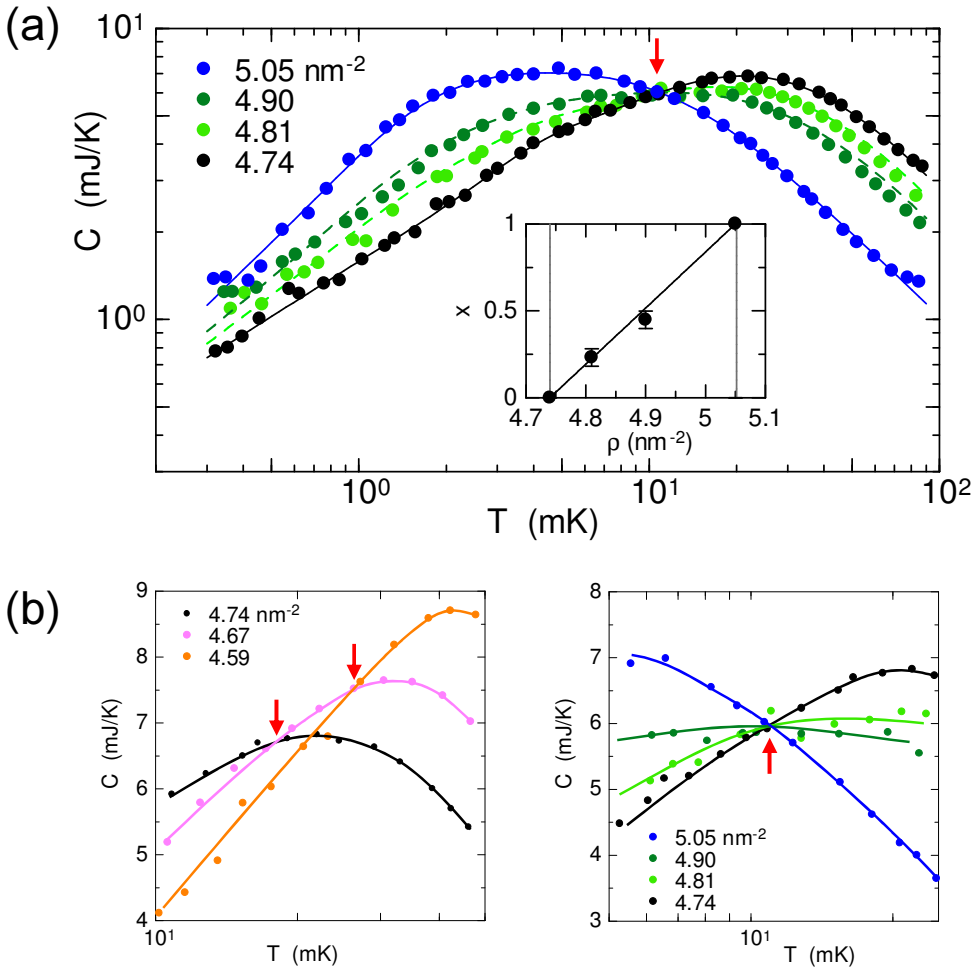

Fig. 6.4: (a) The heat capacity data at 4.74 4.81, 4.90 and 5.05 nm^{-2} in the coexistence region. All the data cross at one point indicated by the red arrow. The dashed lines are the fitted data using Eq.(6.1) with $x = 0.23$ and 0.45, where x is the fraction of the C2-like phase. The inset shows the density variation of x. (b) right: A closeup of panel (a) near the crossing point. left: A closeup of the heat capacity data at 4.59, 4.67, and 4.74 nm^{-2} for comparison. They do not cross at one point, as indicated by the two red arrows.

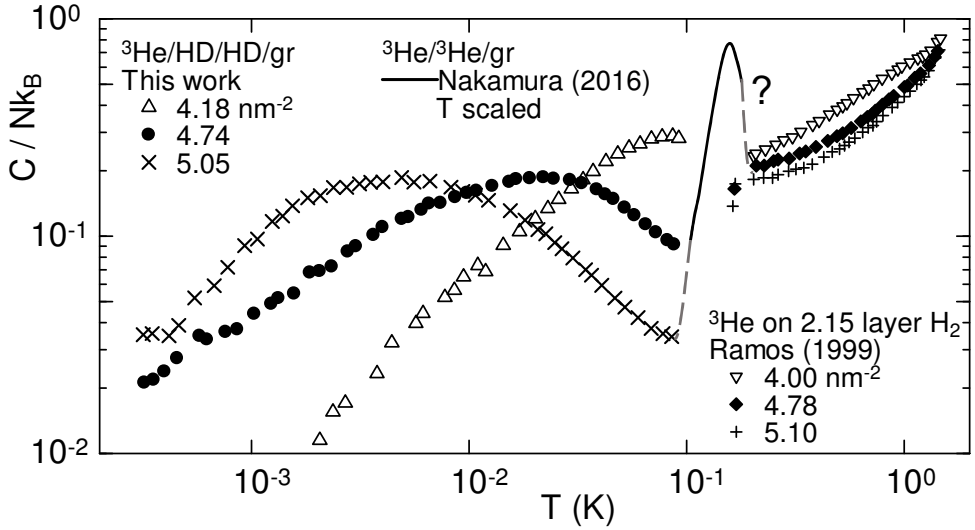

Fig. 6.5: The specific heat data of ^{3}He/HD/HD/gr at 4.18, 4.74, and 5.05 nm^{-2}, representing the Fermi liquid, C3, and C2 like phases. The ^{3}He/H$_2$/H$_2$/gr data at 4.00, 4.78, and 5.10 nm^{-2} are also plotted. The solid line is the specific heat anomaly of ^{3}He/^{3}He/gr indicating 2D melting of the C2 phase[16], whose temperature is divided by 6.5.

Comparison with the high T specific heat of ^{3}He/H$_2$/H$_2$/gr

The highest temperature of our measurements is limited to $T_{\max} = 90$ mK because the Zn HSW become thermally conductive at $T > 90$ mK, and no high temperature measurements on this system have not been performed. We compared the data in this work with the specific heat measurements of ^{3}He adsorbed on a 2.15 layer of H$_2$ by Ramos *et al.*[38] The areal density of the second layer HD and H$_2$ are 9.1 – 9.2 nm^{-2} and 8.65 nm^{-2}. Figure.6.5 shows the specific heat data of ^{3}He/HD/HD/gr measured at the selected densities; 4.18, 4.74, and 5.05 nm^{-2}, representing the Fermi liquid, C3, and C2-like phases. They are compared with the data of ^{3}He/H$_2$/H$_2$/gr system at densities similar to ours; 4.00, 4.78, and 5.05 nm^{-2} down to $T = 200$ mK. The specific heat of the sample at 5.05 nm^{-2} for ^{3}He/HD/HD/gr and the one at 5.10 nm^{-2} for ^{3}He/H$_2$/H$_2$/gr show similar disconnectivities, indicating the order-disorder transition of the C2-like phase. For example, there is a specific heat anomaly shown as the solid line in Fig.6.5 between 90 and 200 mK.This line is the specific heat peak associated with the 2D melting transition of the C2 phase of ^{3}He/^{3}He/gr [16] whose temperature is divided by 6.5.

6.2 Nuclear magnetism of C3 phase (4.74 nm^{-2})

Figure 6.6 shows the heat capacity at the density of the C3 phase ($\rho = 4.74$ nm^{-2}). The magnetic heat capacity has a broad single peak at $T = 21$ mK indicating short range ordering, and an unconventional temperature dependence $C \propto T^{2/3}$ at $T \leq 5$ mK indicating there are many low energy states. This behavior is quite inconsistent with the specific heat of the C2-like or IC phases, as shown as the thick lines in the

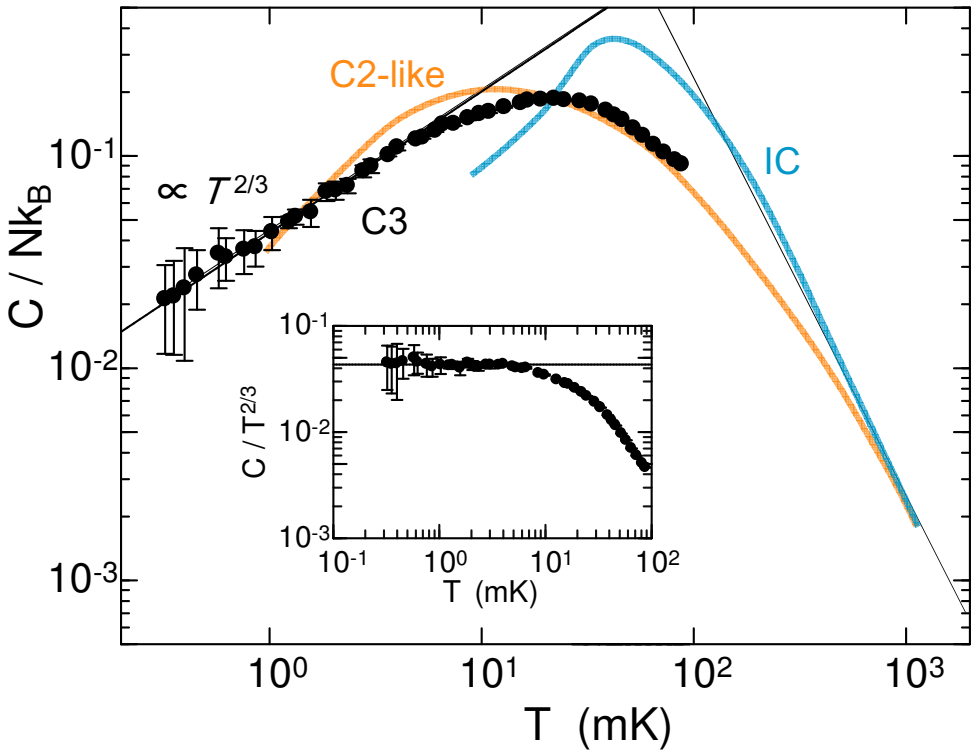

Fig. 6.6: Specific heat C/N_1k_B of the ^{3}He film at 4.74 nm^{-2}. At $T \lesssim 5$ mK, the data satisfy $C \propto T^{2/3}$. C/N_1k_B of the C2-like and IC phases are also shown for comparison. The temperature scale of these data are normalized by J_C. The inset shows the heat capacity divided by $T^{2/3}$.

Fig.6.6. The heat capacity of the C3 phase clearly disagrees with the $C \propto T$ behavior observed for other QSL candidates with triangular lattices [92, 94, 109], the C2 phases of ^{3}He/^{3}He/gr [6], and the ^{3}He/^{4}He/gr systems [36].The data also differ from the $C \propto T^2$ relationship expected for the magnon excitations of the 120° Neel ordered state [82]. Such an anomalous temperature dependence should reflect the quite strong magnetic frustration of the C3 phase due to an even lower density than the C2(-like) phase.

Figure 6.7 shows the spin entropy deduced by integrating the measured heat capacity. The entropy is normalized by the total spin entropy $N_1 k_B \ln 2$. We assumed $C \propto T^{2/3}$ below the lowest measured temperature 0.3 mK. Though the high T heat capacity was not fully observed in these measurements, within the measured temperature range, more than 93 % of the total entropy is released. This indicates that almost all of the nuclear spin properties were observed. At $T \gg T_{\rm peak}$ the heat capacity seems to follow $C \propto T^{-1}$.

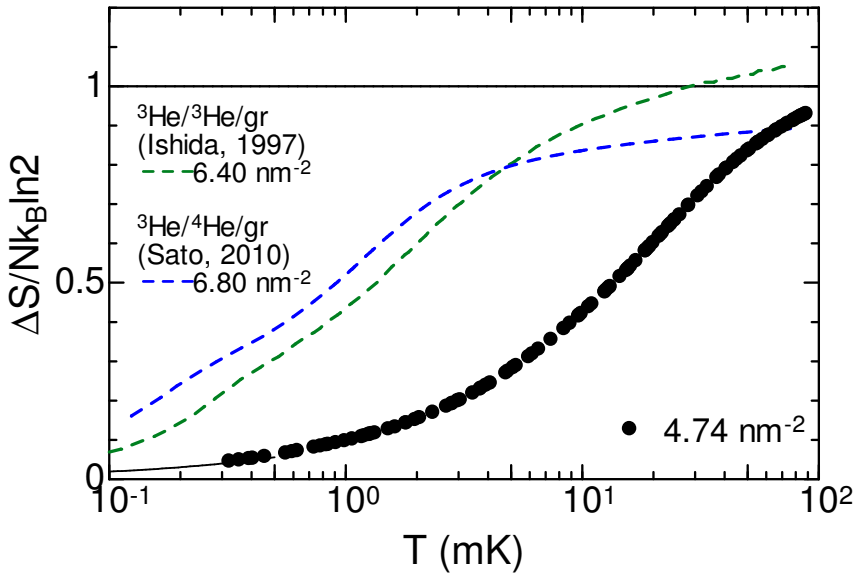

Fig. 6.7: The entropy calculated from the heat capacity data given in Fig.6.6. Below the lowest temperature (0.3 mK) of the present measurements, the entropy was calculated by assuming $C \propto T^{2/3}$. The lines are the entropies deduced from the specific data of the C2 phases. In these systems, we assumed the $C \propto T$ behavior to extrapolate the calculation to $T = 0$

It is theoretically expected that the high-T heat capacity of a spin system is $C \propto T^{-2}$, but our data decays more slowly. The exchange interaction J_C is inferred by fitting the data at 25 mK to

$$C = N k_B P[2, 2]. \tag{6.2}$$

Interestingly, the magnetic susceptibility (χ) data at $\rho' = 4.82$ nm^{-2}, obtained in the previous NMR measurements performed by Ikegami *et al.* and Masutomi *et al.* [7, 17], satisfy $\chi \propto T^{-1/3}$, which was not originally claimed by the authors. The density correction of the data in Ref.[7, 17] is described in Appendix A. Figure 6.8 shows $\chi T^{1/3}$ as a function of temperature. Therefore the C3 phase is gapless or with a spin gap less than $0.01/\theta_W = 0.01/9 \approx 10^{-3}$.

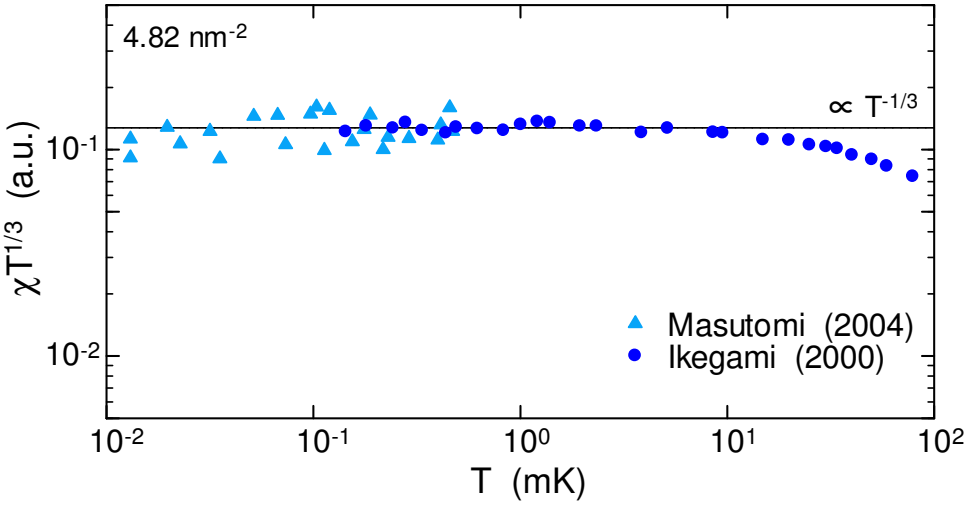

Fig. 6.8: The magnetic susceptibility χ data of Ref.[17] (dot) and of Ref.[7] (triangle) at 4.82 nm^{-2} divided by $T^{-1/3}$ are plotted as a function of temperature. The data agree very well with $\chi \propto T^{-1/3}$ in a wide temperature range over three orders of magnitude.

Such unconventional behaviors of C and χ enables us to define the Wilson ratio $R_{\rm W}$

$$R_{\rm W} \equiv \frac{\chi T}{C} \propto \frac{T^{-1/3}T}{T^{2/3}} = \text{const.} \tag{6.3}$$

We calculate $R_{\rm W}$ using our heat capacity data at 4.74 nm^{-2} and susceptibility data at 4.82 nm^{-2} [17] and obtain $R_{\rm W} \approx 6$. This value is considerably larger than that of the ideal Fermi gas and organic QSL materials with $R_{\rm W} \approx 1$[83, 92]. This indicates that elementary excitations in the ^{3}He C3 phase have strong correlations rather than the noninteracting Fermi gas. Considering the characteristic T dependence of the specific heat and magnetic susceptibility, the elemental excitations from the ground state is likely to be the fermionic excitations with $E \propto k^3$ dispersion, where E is the energy and k is the momentum.

Both $C \propto T^{2/3}$ and $\chi \propto T^{-1/3}$ are qualitatively consistent with the gapless QSL theory by Biswas *et al.* [110]. The theory is not based on a specific Hamiltonian. The authors derived the relation from the triangular lattice, SO(2) symmetry, and Majorana Fermions elementary excitation of $S = 1$. From these assumptions, they derive the dispersion $E \propto k^3$, resulting in a specific heat of $C = 1.18 r_0 T^{2/3}$ and magnetic susceptibility of $\chi = 0.38 \mu^2 r_0 T^{-1/3}$ at low temperatures, where μ is a magnetic moment and r_0 is a parameter proportional to the density of state. Both are qualitatively consistent with experimental observations. To check the quantitative consistency, we compared a constant parameter r_0 deduced independently by fitting the C and χ data at 4.74 and at 4.82 nm^{-2}, respectively [17]. The coefficient of the $T^{2/3}$ term of the specific heat is 0.43, corresponding to $r_0 = 0.37$. The fitting of the χ data yields $r_0 = 0.084$. The r_0 values deduced from the experimental data differ by a factor of ≈ 4.4. The Wilson ratio calculated from this theory is $R_{\rm W} = 4.3$ [110], which is smaller than $R_{\rm W} \approx 6$ by a factor of ≈ 1.4. Though this theory does not have perfect quantitative agreement with the experiments, it demonstrates the best consistency with the C3 phase, and it is therefore expected that the gapless QSL state in the C3 phase has exotic elementary excitations, such as Majorana Fermions.

Another theory based on the MSE Hamiltonian for up to 4 body exchange predicts the U(1) QSL state with a $C \propto T^{2/3}$ dependence [65]. The theory predicts a QSL ground state if the contribution from J_4 is large. However, this model also predicts the constant magnetic susceptibility, which is not consistent with the experimental result. Moreover, in this theory only the parameter space with $J_2^{\text{eff}} > 0$ is investigated, but $J_2^{\text{eff}} < 0$ is obtained by fitting the susceptibility data [17].

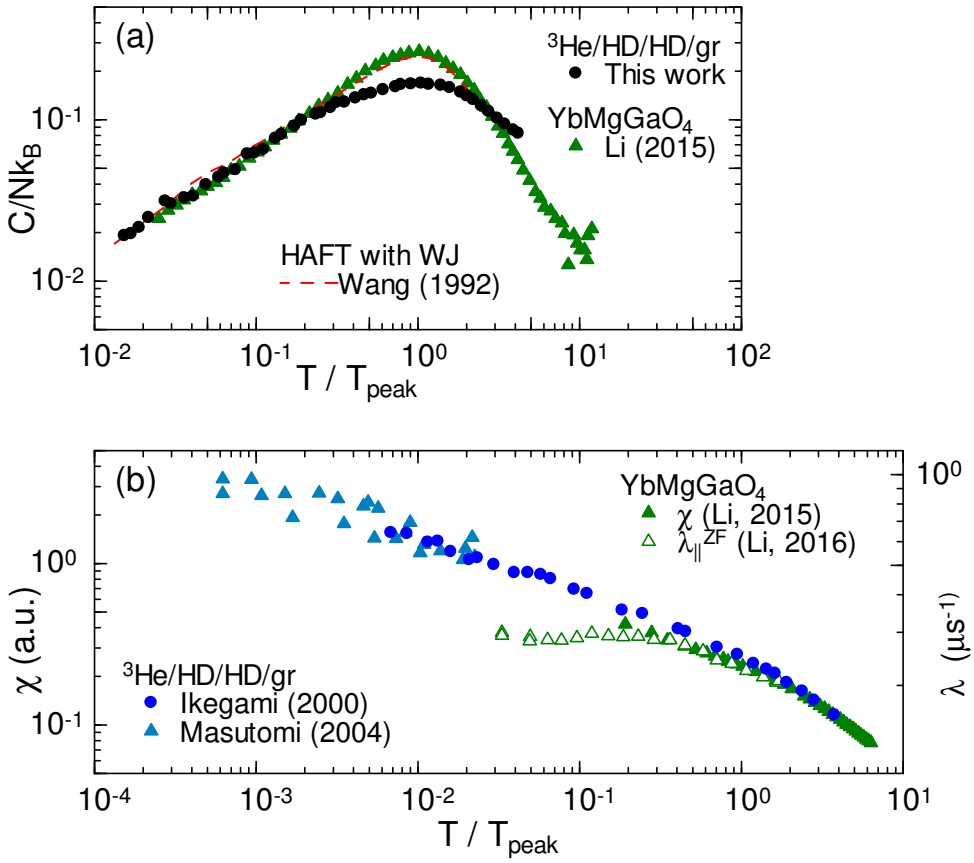

Fig. 6.9: Comparison between the C3 phase of ^{3}He/HD/HD/gr and other studies yielding $C \propto T^{2/3}$. (a) The specific heat C/k_{B} obtained in this work and $YbMgGaO_4$ (The green symbols) vs normalized temperature T/T_{peak}. The theoretical calculation based on the HAFT model with the WJ transform [111] is also shown as the red dashed line. (b) The magnetic susceptibility data of ^{3}He/HD/HD/gr at 4.82 nm^{-2}[7, 17], and that of $YbMgGaO_4$. The relaxation rate at zero field with the incident beam parallel to the c axis (perpendicular to the triangular plane) is also plotted.

Wang calculated the HAFT model based on the 2D Wigner-Jordan (WJ) transformation, where the spin operators $\mathbf{S}$ are transformed into spinless operators d. The author found that the nearest neighbor virtual bonding (NNVB) state of the WJ fermion has a smaller energy compared with the Néel state. The elementary excitations of the NNVB state are gapless fermions. In this model, the single particle energy become

$$E(\mathbf{k}) = -2J(1+2\Delta)[\sin(\mathbf{k}.\delta_1) + \sin(\mathbf{k}.\delta_2) + \sin(\mathbf{k}.\delta_3)], \tag{6.4}$$

where J, Δ, $\mathbf{k}$, and δ_i are the exchange interaction, magnitude of the nearest neighbor bonding field, momentum vector, and nearest neighbor vector, respectively. At $|\mathbf{k}| \to 0$ this relation can be approximated as $E \propto k^3$, which results in $C \propto T^{2/3}$ and $\chi \propto T^{-1/3}$. The specific heat calculated in Ref.[111] is compared with the experimental data of the C3 phase in Fig.6.9. The calculated specific heat has a peak at $T/2J = 0.75$. The peak is sharper with a faster decay at high temperature compared with the experimental data of the C3 phase.

The $C \propto T^{2/3}$ dependence was recently observed in the QSL candidate with triangular lattice $YbMgGaO_4$[112]. Figure 6.9 shows the specific heats of both systems as a function of normalized temperature $T/T_{\rm peak}$. These data agree with each other at $0.02 < T/T_{\rm peak} < 0.2$. This consistency indicates that the elementary excitations of these materials have similar energy spectrums. However, their peak structures are different. The peak for $YbMgGaO_4$ is sharper and its magnitude is approximately 40 % larger, than that of the C3 phase. At $T > T_{\rm peak}$, the specific heat decay satisfy $C \propto T^{-2}$ as expected for a noninteracting spin system with $S = 1/2$; however, as mentioned above, the C3 phase show weaker dependence.

The magnetic susceptibility of both systems also show similar $\chi \propto T^{-1/3}$ behavior down to $T/T_{\rm peak} = 0.1$. However, the μSR measurements on $YbMgGaO_4$ demonstrated that the relaxing rate λ become T-independent at $T/T_{\rm peak} < 0.1$, which is evidence of the U(1) QSL. However, the ^{3}He C3 phase satisfies the $\chi \propto T^{-1/3}$ relation down to $T/T_{\rm peak} \approx 0.0006$.

6.3 Conclusion

We performed heat capacity measurements on ^{3}He/HD/HD/gr in the density region between the Fermi liquid and C2-like phases, with small density steps. As a result, we discovered the new quantum phase, termed "C3 phase", previously unreported in bilayer ^{3}He systems. The C3 phase is separated by the Fermi liquid and C2-like phases via phase transitional regions and is limited in a narrow density window ($\Delta\rho/\rho_{\rm C3} \lesssim 2\%$). Previous studies on this system overlooked this phase. The phase transition from the Fermi liquid to the C3 phase cannot be explained by simple two phase coexistence and the details are yet to be determined. However, the transition from the C3 to C2-like phase is most probably produced by macroscopic two phase coexistence (the 1st order phase transition). The reason why the C3 phase exists only in ^{3}He/HD/HD/gr and not in bilayer ^{3}He systems, is probably the larger potential corrugation by the HD layer which assists ^{3}He localization.

The magnetic specific heat of the C3 phase displays an unusual temperature dependence of $C \propto T^{2/3}$ below a single broad peak. Considering the equally unconventional magnetic susceptibility $\chi \propto T^{-1/3}$, we defined the Wilson ratio $\chi T/C$ with the results suggesting fermion type elemental excitations with $E \approx k^3$ dispersion. These are expected to be the exotic elementary excitations, such as Majorana fermions. Such interesting nuclear magnetism of the C3 phase is likely due to its low density, which enhances competition among the MSE parameters and produces stronger magnetic frustration than that of the C2(-like) phase.

Chapter 7

Normal Fermi liquid phase near localization

In this chapter, we discuss the results of heat capacity measurements on the ^{3}He/HD/HD/gr system at $0.7 \leq \rho \leq 4.2$ nm^{-2}, shown as the colored region in Fig.7.1.

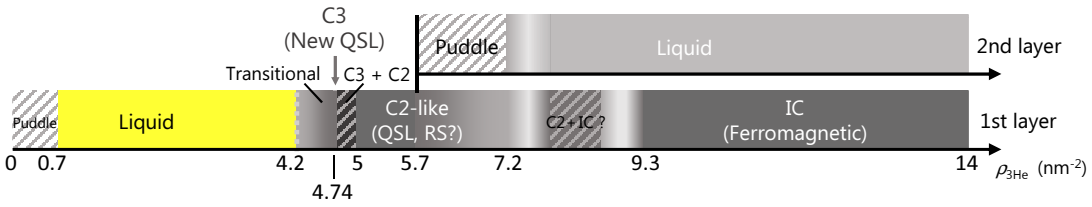

Fig. 7.1: Phase diagram of ^{3}He/HD/HD/gr. The shaded region is discussed in this chapter.

7.1 Critical behavior of Fermi liquid near localization ($0.7 \leq \rho \leq 4.2$ nm^{-2})

The heat capacity data up to 4.18 nm^{-2} satisfy $C \propto T$ at low T, which is the typical behavior of a Fermi liquid. We fitted the heat capacity data for $T > 2$ mK to Eq.(2.22), and the fitted results are shown in Fig.7.2. The temperature range of the fitted curve in the figure represents the temperature range of the data used for the fit. Figure 7.3 (a) shows the density dependence of the γ coefficient obtained by fitting the data to and Eq.(2.21). The γ coefficients of the previous study on ^{3}He/HD/HD/gr taken by Casey *et al.*[39] are also plotted. In addition to the original data from Fig.2 in Ref.[39], we plotted the γ values obtained by reanalysing the data in Ref.[39] assuming that the $T-$dependence of the amorphous heat capacity is the same as the 0.46 nm^{-2} data in this work (hereafter "reanalyzed data"). We also corrected the density scale of the reanalyzed data by considering the amount of the amorphous ^{3}He. The details of this reanalysis is described in Appendix A. The reanalyzed γ coefficient is larger than the original value, because the amorphous heat capacity used for the reanalysis decrease with increasing temperature for $T > 3$ mK. Therefore the γ value become greater than the value deduced

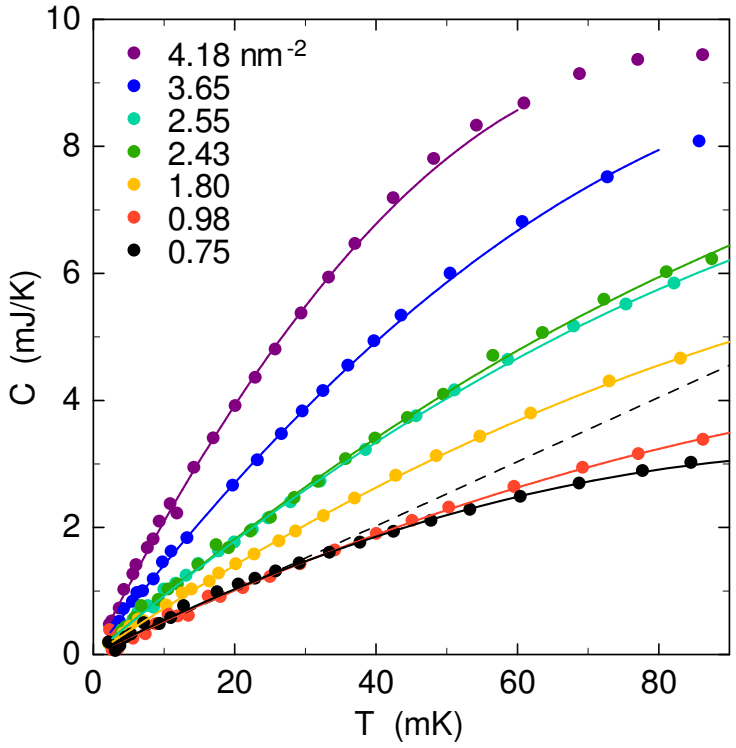

Fig. 7.2: The heat capacity data at $0.75 \leq \rho \leq 4.18$ nm^{-2} in the Fermi liquid region. The solid lines are the fitted curves using Eq.(2.22). The dashed line represents the behavior of noninteracting 2D Fermi gas.

using the T-independent amorphous heat capacity which is predicted by the Golov-Pobell model. In Ref.[39], the heat capacity data up to 5.00 nm^{-2} were analysed as the Fermi liquid. However, as discussed in Sec.6.1, we observed that the low T heat capacity deviated from $C \propto T$ for the densities greater than 4.18 nm^{-2}, indicating solidification of the ^{3}He film. This means that in Ref.[39] the data of the samples which were not in the Fermi liquid were analysed as the Fermi liquid. Because the γ coefficient of the reanalyzed data at 3.88 nm^{-2} ($m^*/m \approx 4.3$) and that of the data in this work at 4.18 nm^{-2} ($m^*/m \approx 4.4$) is almost the same, we only used the data in Ref.[39] for $\rho \leq 3.88$ nm^{-2}, corresponding to 4.4 nm^{-2} in the original density scale, in the following discussion. The effective mass showed the divergence. The maximum value of m^*/m obtained in this work was 4.4 ± 0.3 at 4.18 nm^{-2}. We analysed these data in the same way as in Ref.[39]. The m^*/m data were fitted to Eq.(2.23). The fitted curves are shown as the solid lines in Fig.7.3 (a). The small triangles were not used for the fit. ρ_c and ν obtained from the fitting are described in Table.7.1. The data in this work yielded $\rho_c = 6.35 \pm 0.08$ nm^{-2}. This critical density was far larger than the reported value of 5.1 nm^{-2} [39], the density of the C3 phase (4.74 nm^{-2}), and the onset of the C2-like phase (5.05 nm^{-2}). We also obtained $\nu = 1.36 \pm 0.02$ which is larger than $\nu = 1$ expected from Eq.(2.27) with a critical exponent $z = 4$.

The reanalyzed data yielded $\rho_c = 5.85$ nm^{-2} and $\nu = 1.34$. Both of these values were similar to the data in this work, rather than that in the original data. The critical density ρ_c of the original data was 5.46 nm^{-2}, greater than 5.1 nm^{-2} reported in Ref.[39], because the density range for the fit was limited up to 4.4 nm^{-2}. Note that $\rho_c = 5.1$ nm^{-2} was

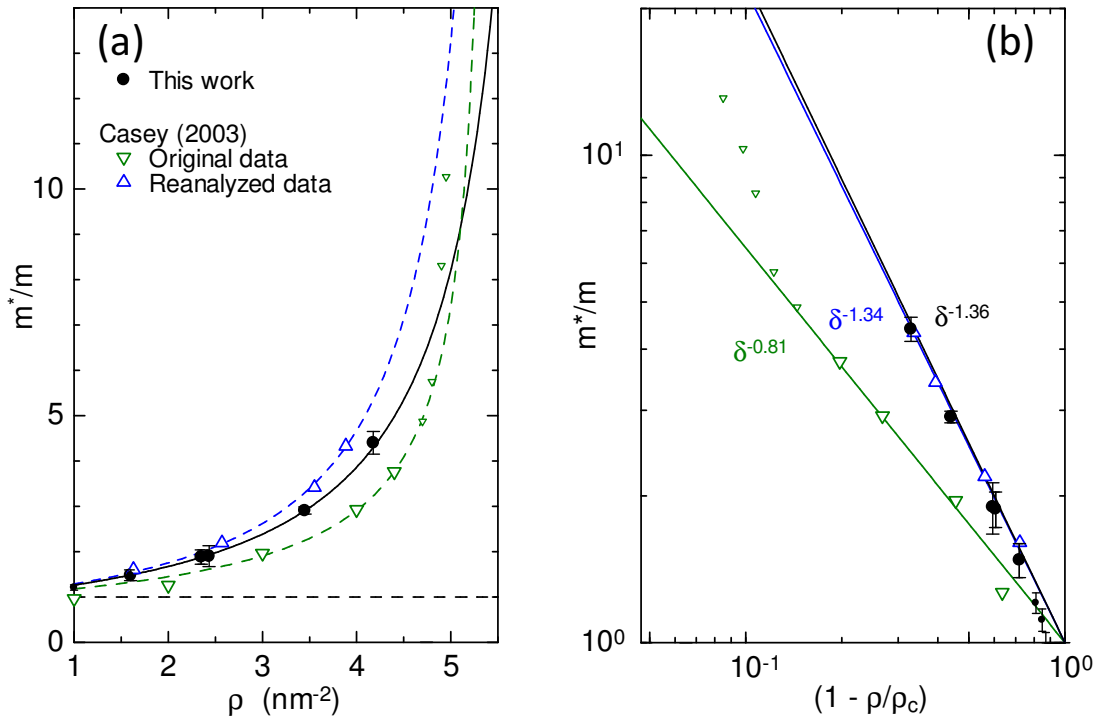

Fig. 7.3: (a) The density dependence of the ^{3}He quasiparticle effective mass enhancement m^*/m deduced from the heat capacity data. (b) The effective mass plotted as a function of $(1-\rho/\rho_c)$. The green inverse triangles and blue triangles are the original and reanalyzed data in Ref.[39], respectively. See Appendix A for details of the reanalysis. The solid lines are the fitted curves using Eq.(2.23). The small triangles are not used for the fit.

reproduced if we used the original data up to 5.00 nm^{-2} for the fit, but in this case we obtained $\nu = 0.77$, smaller than $\nu = 1$ expected from the scaling relations proposed by Imada [72] and the critical exponent $z = 4$ deduced by the α coefficient of the T^2 term [39]. Figure 7.3 (b) shows m^*/m as a function of $(1 - \rho/\rho_c)$

	ρ_c	ν	z_ν	μ	z_μ
This work	6.35±0.08	1.36±0.03	4.72±0.06	2.3±0.1	3.5±0.2
Casey, reanalysis[39]	5.85±0.43	1.34±0.17	4.68±0.34	2.5±0.1	4.3±0.5
Casey, original[39]	5.46±0.43	0.81±0.15	3.62±0.67	3.0±0.2	3.2±0.3

Table 7.1: ρ_c, ν, and μ obtained by fitting these data sets. Critical exponentsz_ν and z_μ are deduced from ν and μ assuming the scaling theory in Ref.[72].

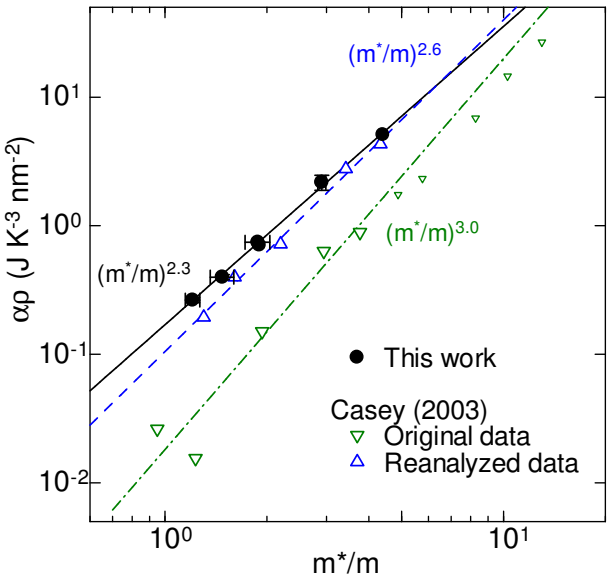

Fig. 7.4: $\alpha\rho$ as a function of the effective mass enhancement m^*/m. Here, α is the coefficient of the T^2 term in Eq.(2.22). The symbols are the same as Fig.7.3. The lines are the fitted curves using Eq.(7.1)

Next, we analysed α, the coefficient of T^2 term. Figure 7.4 shows the product of the α coefficient and the density ρ as a function of m^*/m. Three data sets were fitted to

$$\alpha\rho = a(m^*/m)^\mu, \tag{7.1}$$

where a and μ are fitting parameters. The original data kept the reported value of $\mu = 3$ even after changing the density range for the fit. However the data in this work and the reanalyzed data yielded smaller values of $\mu = 2.3$ (this work), $\mu = 2.6$ (reanalyzed data).

The fitted results were compared with the scaling theory in Ref.[72] which is introduced in Sec.2.2.3. Using the scaling relations, we deduced the critical exponent z in

two independent methods. One used ν and Eq.(2.27), and z determined in this way was named z_ν which is expressed as follows

$$z_\nu = d(1+\nu) = 2(1+\nu), \tag{7.2}$$

where d is the dimension of the system. The other method used ν, μ, and Eqs.(2.27) and (2.28). The z exponent determined in this way was named z_μ which is expressed as follows

$$z_\mu = d\nu(\mu - 1) = 2\nu(\mu - 1). \tag{7.3}$$

Calculated z_ν and z_μ are described in Table.7.1. We observed the self-inconsistency between z_ν and z_ν for the data in this work. For the original and reanalysed data in Ref.[39], z_ν and z_μ were consistent, but the values were different from the reported value of $z = 4$. The reason why z_ν and z_ν of the original data is different from $z = 4$ is that we used $\nu = 0.81$ and not $\nu = 1$ originally assumed.

Another theory of Mott-Hubbard transition from the dynamical mean field theory points out that the coherence temperature T_0, below which the system can be well described as the Fermi liquid, shows the power law behavior $T_0 \approx \delta^{1.5}$ [113]. If we define the coherence temperature in the same way as in Eq.(2.26), the data in this work (reanalyzed data) yield $T_0 \approx \delta^{1.6}$ ($T_0 \approx \delta^{1.9}$) and the value is close to 1.5. Although this theory does not predict the critical exponent ν, it shows better consistency with the experimental results in this work.

7.2 Conclusion

We measured heat capacity of the normal Fermi liquid. The effective mass divergence was observed, but the critical behavior near localization was different from the previous report. The new results still do not exclude the Mott-Hubbard scenario. The discrepancy between this work and the previous results is owing to two factors. One is that the previous workers included the data which is in the transitional region towards the C3 phase. The other is that they assumed the too simplified amorphous heat capacity based on the Golov-Pobell model.

Chapter 8

Liquid puddle formation in the low density limit

In this chapter, we discuss the results of heat capacity measurements on the ^{3}He/HD/HD/gr system at $0.1 \leq \rho \leq 0.7$ nm^{-2}, shown as the colored region in Fig.8.1.

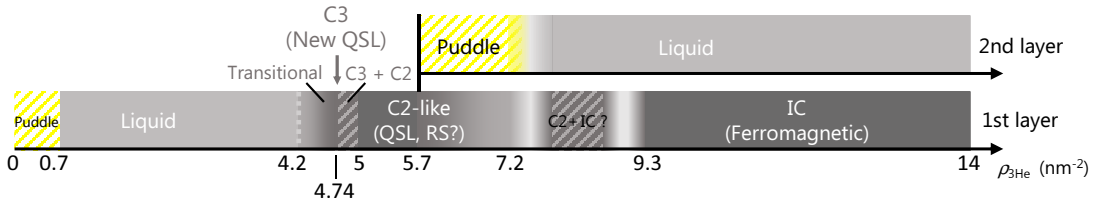

Fig. 8.1: Phase diagram of ^{3}He/HD/HD/gr. The shaded region is discussed in this chapter.

8.1 1st layer

The heat capacity data of the ^{3}He film below $\rho = 4$ nm^{-2} are shown in Fig.8.2 (a). As already discussed in the previous chapter, in this density range the data satisfy $C \propto T$ at low T. We fitted the data to Eq.(2.22) shown as the solid curves in Fig.8.2 (a). The dashed line in Fig.8.2 (a) represents the $C = \gamma_0 T$ behavior, where γ_0 is the value of the noninteracting Fermi gas spreading over the whole surface area. The density dependence of the γ coefficient obtained by fitting the heat capacity data to Eq.(2.22) is shown in Fig.8.2 (b). The dashed line in this figure represents the value of γ_0. The behavior of γ was similar to that of the 1st and 2nd ^{3}He layer on bare graphite surfaces, shown as the blue and red symbols in Fig.8.2 (b), respectively [23, 24, 43]. There is a kink at $\rho_C \approx 0.7$ nm^{-2}. At $\rho > 0.7$ nm^{-2} γ diverged with increasing density, as discussed in the previous section. Below the kink γ changed linearly with the density and was smaller than γ_0. This is strong evidence that the ^{3}He self-condensed liquid phase was also formed on a bilayer of HD despite the difference in the potential corrugations. If we extrapolate the behavior of the γ coefficient above the kink density to 0 nm^{-2}, the value is slightly larger than γ_0. This indicates the mass of a ^{3}He atom is enhanced by the interaction between a ^{3}He atom and the underlayers, and the similar behavior was also observed in the previous

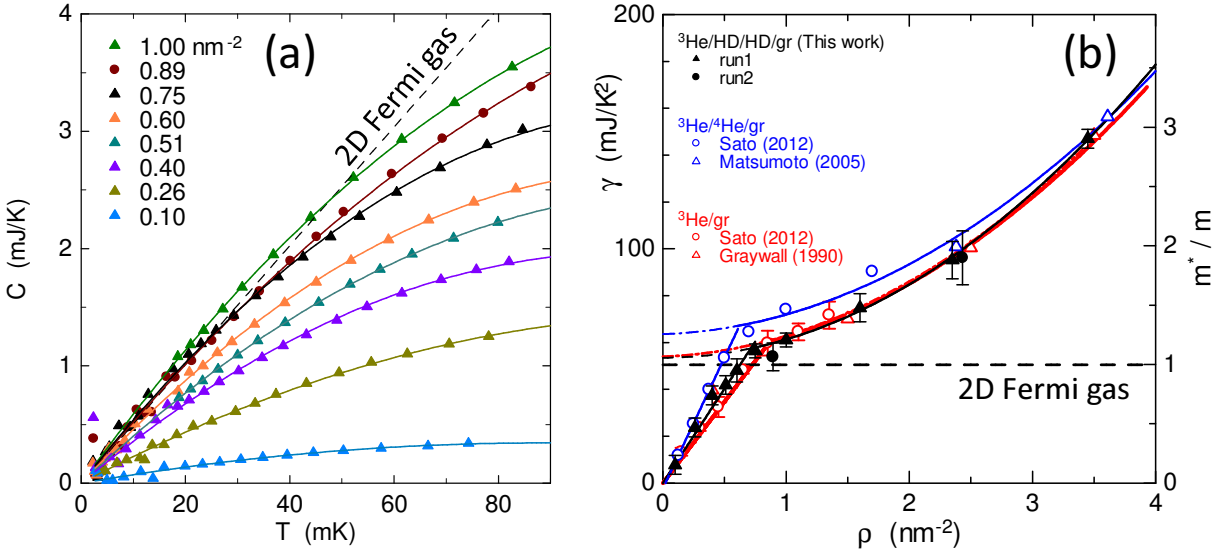

Fig. 8.2: (a) The heat capacity data at $0.1 \leq \rho \leq 1.00$ nm^{-2}. The dashed line shows $C = \gamma_0 T$ behavior expected to the noninteracting Fermi gas. (b) The density dependence of the ^{3}He quasiparticle effective mass enhancement m^*/m deduced from the heat capacity data. Below a kink at $\rho \approx 0.7$ nm^{-2}, m^*/m changes linearly with ρ. The data of the 1st and 2nd layer ^{3}He on graphite are also shown for comparison. The dashed line represents γ_0

results of the 1st and 2nd ^{3}He layers on the bare graphite [23]. The mass enhancement at $\rho \to 0$ is predicted by some theories considering the realistic potential corrugations from the substrates. [10, 79, 114] For example, a theory of the 1st ^{3}He layer on the bare graphite predictes the mass enhancement of $m^*/m = 1.03$, and another theory of the ^{3}He film on graphite plated with the ^{4}He monolayer predicts $m^*/m = 1.02$ [79]. According to Gasparini *et al.*, the liquid puddle with the higher critical density ρ_C has the greater mass enhancement at dilute limit [114]. However, the 2nd layer puddle, which has the lowest critical density $\rho_C \approx 0.6$, has the largest m^*/m. Therefore the prediction by Gasparini is inconsistent with the experimental results.

In the puddle phase, the γ and α coefficients obtained by fitting the data to Eq.(2.22) increases with increasing density in a similar manner as shown in Fig.8.3. This behavior is consistent with the simple expectation that, added ^{3}He is not used to change the liquid density but to increase the surface area of the puddle. The previous measurements of the ^{3}He puddle on graphite plated with the ^{4}He monolayer by Sato *et al.* displayed the decrease in α/γ to zero at $\rho \to 0$ [23]. They concluded that the reduction is because the long-wavelength modes of the spin fluctuations were cut off when the size of the puddle was small. This is inconsistent with the results of the ^{3}He puddle on the HD. However, the detailed comparison and discussion are difficult because the α coefficients obtained in this work have large error bars especially at low density, mainly due to determination of the amorphous heat capacity. Once the puddle spread over the whole surface of the substrate, γ and α coefficients show different density dependences because added ^{3}He is used to increase the density of the liquid and enhance the interactions among ^{3}He atoms

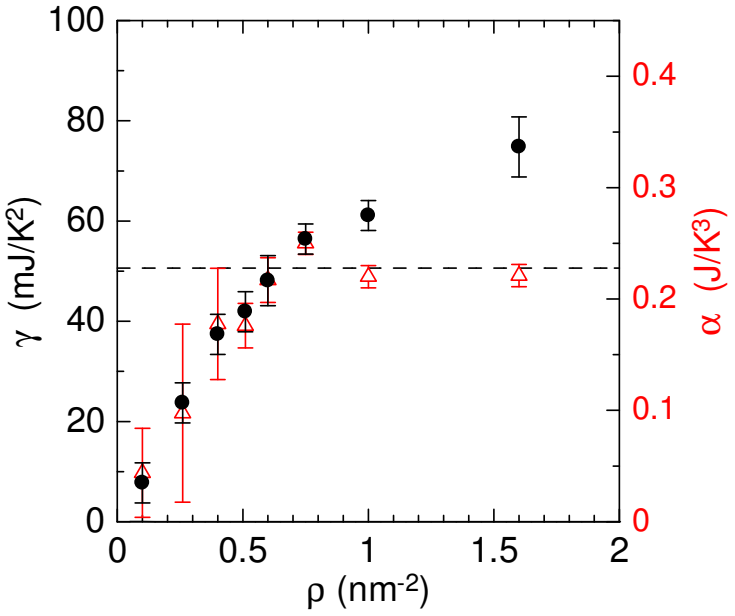

Fig. 8.3: The density dependence of the γ (the filled circles) and α (the open triangles) coefficients. The dashed line represents the value of γ_0. In the puddle region these coefficients increase similarly with the density.

8.2 2nd layer

The γ coefficient of the 2nd layer liquid on the HD as a function of $\rho - \rho_{\rm promotion}$ is shown in Fig.8.4, where $\rho_{\rm promotion}$ is the density where the layer promotion occur. The 2nd layer promotion occured at $\rho_{\rm promotion} \approx 5.7$ nm^{-2} (see Sec.5.1). At $\rho - \rho_{\rm promotion} \leq 1.45$ nm^{-2}, γ is smaller than γ_0. Therefore the 2nd ^{3}He layer on the HD forms the self-condensed liquid like the 1st layer on the HD. A previous heat capacity measurements of the ^{3}He films on the HD also mentioned the $\gamma < \gamma_0$ relation just after the 2nd layer promotion [18]. The γ coefficients of the 1st ^{3}He layer on the HD and that 3rd ^{3}He layer on the bare graphite (^{3}He/^{3}He/^{4}He/gr) [23] are also plotted in Fig.8.4 for comparison. The γ coefficient of the 2nd ^{3}He layer on the HD increased far more slowly than that of the 1st ^{3}He layer on the HD. The slope is rather close to that of the 3rd ^{3}He layer on the bare graphite just after the layer promotion. The slope of the γ coefficient of the 2nd ^{3}He layer on the HD increased gradually with increasing density. The change in the slope was also observed for the 3rd layer ^{3}He puddle on the bare graphite. The density dependence of γ of the 3rd layer ^{3}He had a clear kink at $\rho - \rho_{\rm promotion} = 0.5$ nm^{-2} where the slope was three times larger. Below this kink a 1/3 of the added ^{3}He was adsorbed on the topmost layer but the other 2/3 compressed the second layer. Above the kink all of the added ^{3}He atoms were adsorbed on the 3rd layer. The NMR measurements of the 3rd ^{3}He layer [116] were consistent with the heat capacity measurements [23]. Note that not all of the ^{3}He atoms added after layer promotion are necessarily adsorbed on the topmost layer. As already mentioned, the neutron scattering experiments on the ^{3}He films on the bare graphite observed the increase in the density of the 1st ^{3}He layer by a few % even after

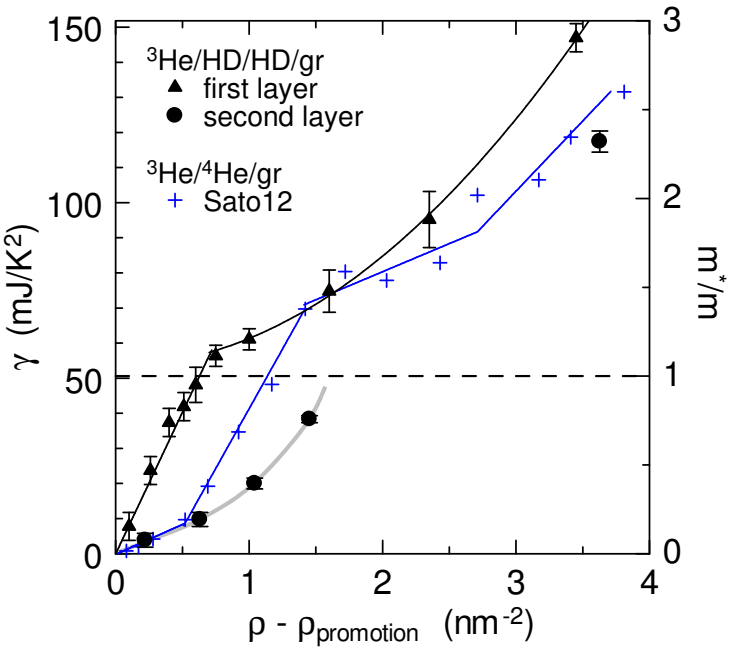

Fig. 8.4: The γ coefficient ($\propto m^*/m$) as a function of the density after subtracting the one where layer promotion occur $\rho - \rho_{\rm promotion}$. The filled circles are the data of the 2nd layer puddle on the HD. The thick grey line is a guide to the eye. At $\rho - \rho_{\rm promotion} \leq 1.4$ nm^{-2}, m^*/m is smaller than 1, which indicates the self-bound liquid state in topmost layer ^{3}He. The black triangles and blue crosses are the data of the 1st layer ^{3}He on the HD and the 3rd ^{3}He on the bare graphite from Ref.[23], respectively.

the layer promotion[35]. However, the change in the slope of γ of the 2nd ^{3}He layer on the HD was continuous without a kink. This indicates that, a 1/3 of added ^{3}He was adsorbed on the topmost layer just after the layer promotion, forming the self-condensed liquid, and then the fraction increased gradually with increasing density.

8.3 conclusion

We measured heat capacities of the low density liquid ^{3}He films of the 1st and 2nd layers on a bilayer of HD. The γ coefficients of the T-linear term in both the 1st and 2nd layers were smaller than γ_0, indicating the formation of the self-condensed liquid. The critical density $\rho_{\rm C}$ of the 1st layer puddle was 0.7 nm^{-2}. This value was very close to $\rho_{\rm C}$ of the 1st, 2nd and 3rd ^{3}He layers on the bare graphite (0.6 - 0.9 nm^{-2}) despite the difference in potential corrugations. For the 2nd layer puddle on the HD, $\rho_{\rm C}$ was apparently higher than these values, but the weak density dependence of γ at lowest densities suggests that not all of the added ^{3}He atoms are adsorbed on the 2nd layer but part of them are used to compress the 1st layer.

Chapter 9

Summary and future prospects

Summary

In this study, we performed the heat capacity measurements on ^{3}He/HD/HD/gr system over wide ranges of areal density ($0.10 \leq \rho \leq 13.63$ nm^{-2}) and temperature ($0.16 \leq \rho \leq$ 90 mK) to determine the nuclear magnetic phase diagram of this system and the magnetic properties of the QSL state.

Amorphous Solid At very low areal density in Run1, measured heat capacities have weak temperature dependence, which is roughly consistent with the Golov-Pobell model. This indicates that ^{3}He atoms are in the "amorphous" state where atoms are adsorbed on substrate heterogeneities rather than a flat surface. Although it has been known that HD layer do not reduce heterogeneities of substrate[17]. It was the first direct measurement of the heat capacity of amorphous ^{3}He on the HD film. This enables us to analyze the heat capacity data more accurately beyond the Golov-Pobell model.

C2-like Phase At $5.05 \leq \rho \leq 5.92$ nm^{-2}, we found the system show rather similar frustrated magnetism to that of the C2 phase which was originally anticipated as the 4/7 phase but was reconsidered by the recent heat capacity measurements [16]. Thus we named the relevant phase in the ^{3}He/HD/HD/gr the "C2-like" phase. The magnetism of the C2-like phase is characterized by the quite broad heat capacity peak with the nearly T-linear low temperature envelope. The scaling behavior of normalized specific heat by J_C from 5.05 nm^{-2} to 5.92 nm^{-2} shows large compressibility of 17 %. This is qualitatively consistent with the C2 phase in bilayer ^{3}He system. This result supports the scenario that the C2(-like) phase is not the commensurate solid but probably the "quantum liquid crystal" in which rotational or translational symmetry is partially broken. At $5.7 < \rho$, the T-linear heat capacity above $T = 10$ mK appears, which suggests the layer promotion to the 2nd layer. At the same time, the heat capacity below $T = 5$ mK increases which is associated with the emergent of the ferromagnetic component. This component is probably made under second layer puddle.

Incommensurate Solid At $\rho \geq 9.33$ nm^{-2}, the ferromagnetic heat capacity is observed, which is consistent with the previous magnetization measurements [17]. These results suggest that the ^{3}He film forms the solid phase which has a triangular lattice incommensurate with the underlayer lattice, like the bilayer ^{3}He system. This similarity appears because at such high densities the effect of underlayers is weaker compared with that of theinteractions between ^{3}He atoms.

C3 Phase Between 4.18 and 5.05 nm^{-2}, we observed successive phase transitions separated by the distinct phase (C3 phase). The phase transition between C3 and C2-like phases is the first order transition which is confirmed by the two ways. One is that heat capacities at intermediate densities between the two pure phases can be represented by linear combinations of those of the pure phases. The other is that there exist temperatures (11 mK) at which the $C(T)$ vs. T lines cross each other within the two phase densities. The phase transition between the Fermi liquid and C3 phases is not interpreted as the first order transition. The low T magnetic specific heat of the C3 phase shows the peculiar temperature dependence as $C \propto T^{2/3}$ in a wide T range of $0.015 \leq T/T_{\mathrm{peak}} \leq 0.2$. Here T_{peak} (= 21 mK) is the temperature at which the specific heat has a broad maximum. This is different from any other known T dependence such as $C \propto T^2$ for the 2D antiferromagnetic spin waves, $C \propto T$ for 2D ferromagnetic spin waves or other QSL candidates with triangular lattices [6, 92], etc. However, by combining with the fact that the previously measured magnetic susceptibility[7, 17] follows the similarly curious T dependence as $\chi \propto T^{-1/3}$, our data are indicative of gapless quantum spin liquid phase with exotic magnetic excitations represented by Majorana Fermions.

Fermi Liquid neat Localization At $0.10 \leq \rho \leq 4.18$ nm^{-2}, the T-linear heat capacity at low T is observed, indicating the degenerate Fermi liquid. The coefficient of the T-linear term γ, which is proportional to the effective mass of a ^{3}He quasiparticle, is enhanced with increasing density. We found the critical behavior near the localization is inconsistent with the previous result which suggests the Mott-Hubbard transition with the critical exponent $z = 4$ [39]. We showed that this discrepancy comes from their inappropriate inclusion of the data points belonging to the transitional density region from the Fermi liquid towards the C3 phases and their assuming a less accurate amorphous heat capacity based on the Golov-Pobell model.

Self-Condensed Liquid At $0.10 \leq \rho \leq 0.7$ nm^{-2} and just after the layer promotion to the 2nd layer, we observed the coefficient of the $C \propto T$ term γ smaller than the value of the noninteracting Fermi gas γ_0. Therefore the self-condensed liquid is formed in both the 1st and 2nd layer on HD. The critical density of the 1st layer puddle (0.7 nm^{-2}) is quite similar to the previous results (0.6 - 0.9 nm^{-2} [23]), despite the difference in the potential corrugations.

Future prospects

The result of this work supports the recent melting heat capacity measurement which claims that the C2 phase is not the 4/7 commensurate solid, but compressible QLC state with partially broken symmetry. To confirm it, neutron diffraction studies on the C2 and C3 phases, and theoretical studies for ^{3}He on the HD are desirable.

To understand the complex transitional region in the vicinity of the C3 phase, the detailed density dependence of the magnetic susceptibility of the ^{3}He/HD/HD/gr system is also desirable.

Chapter 10

Acknowledgement

First of all, I would like to express my sincere gratitude to my supervisor Professor Hiroshi Fukuyama for giving me the opportunity for this work and continuous guidance.

I would like to thank Dr.Tomohiro Matsui for instruction about experimental technique, helping me operate the refrigerator, and many things related to daily activities.

The nuclear demagnetization refrigerator used in this work was constructed by early members of Fukuyama laboratory including Dr.Yosuke Matsumoto and Associate Professor Satoshi Murakawa. Dr.Daisuke Sato taught me how to use this powerful refrigerator and basics of a low temperature experiment when I was the first year master student.

In this work I operated the refrigerator for nearly two years in total (Run1 and Run2), and many people collaborated the experiments. Dr.Sachiko Nakamura and Dr.Ryo Toda helped me in an early stage of Run 1. They also gave me many technical advises. Mr.Ryuji Nakamura worked with me for about one year, the most part of Run1. The procedure of removing ^{3}He with keeping a bilayer of HD was developed with him. Mr.Katsuyoshi Ogawa collaborated me from the beginning of Run2. A bilayer of HD in this run was made with him. Mr.Takamasa Suzuki, a member of Murakawa laboratory, joined in the latter half of Run2. Stable supply of liquid ^{4}He by Cryogenic Research Center enabled us to perform such long term experiments.

Dr.Maria Carmen Gordillo and Professor Jordi Boronat kindly allowed me to use the results of their calculation in this thesis before publication.

When I was the master student, Dr.Yuya Kubota and I operated the refrigerator together.

Past and present members of Fukuyama laboratory, Mr.Kouta Matsui, Dr.Kazuki Nakayama, Dr.Jan Raphael Bindel, Mr.Takayuki Nakajima, Mr.Hideki Sato, Mr.Andre E. B. Amend, Mr.Kazuma Kita, Mr.Jun Usami, and Ms.Megumi Avigail Yoshitomi, gave me a lot of support. Past laboratory secretary Mrs.Kayoko Ogita helped me about administrative issues when I was the master student.

MERIT (Material Education program for the future leaders in Research, Industry, and Technology) supported my research life financially and gave me an opportunity to interact with students over wide range of research fields related to material science.

Finally, I wish to thank my family for their warm support throughout my student life.

Decembar 2017
Masahiro Kamada

Appendix A

Reanalysis of measurements on ^{3}He/HD/HD/gr by previous workers

As discussed in Sec.(4.1), we deduced the density of ^{3}He adsorbed on a flat surface of the substrate by subtracting the amount of amorphous ^{3}He. However, previous workers who studied on ^{3}He/HD/HD/gr adopted the nominal density scale including amorphous ^{3}He. Here, we discuss correction of the density scales of some previous works in order to compare our results with them.

A.1 Magnetization measurements by Ikegami (2000) and Masutomi (2004)

Ikegami et al. estimated the amount of the amorphous ^{3}He by fitting the magnetization data in the Fermi liquid region at the 3 densities ($\rho_{\rm nominal}$ = 3.3, 3.8, and 4.5 nm^{-2}). The density evolution of $N_{\rm G}$ is shown in Fig.4.8. Their data is multiplied by 562.5/10.7, the ratio of the substrate surface area. The relation between $N_{\rm G}$ and the total amount of ^{3}He $N_{\rm total}$ as

$$N_{\rm G}[{\rm ccSTP}] = aN_{\rm total} + b. \tag{A.1}$$

By dividing both sides of this equation by the surface area, the correction formula become

$$\rho[{\rm nm}^{-2}] = \rho_{\rm total} - \rho_{\rm G} \tag{A.2}$$

$$\rho_{\rm G}[{\rm nm}^{-2}] = 0.0383\rho_{\rm total} + 0.332. \tag{A.3}$$

For example, through Eq.(A.2) 5.20 nm^{-2} become 4.82 $\pm$ 0.04 nm^{-2}. The density of the ^{3}He film on a bilayer HD reported in Ref.[7] can also be viewed as 4.82 nm^{-2}, because the authors mention that the density of their sample is consistent with the ^{3}He film at 5.2 nm^{-2} in Ref.[17].

A.2 Heat capacity measurements by Casey (2003)

In Ref.[39], Casey *et al.* analyzed their heat capacity data assuming the amorphous contribution as a temperature independent term β. They obtained γ and α coefficients

by fitting the data to

$$C(T) = \gamma T - \alpha T^2 + \beta. \tag{A.4}$$

The magnitude of β term is not reported in their papers. They only commented that β term increases by a factor of 3 over the density range investigated. Here, we reanalyzed their heat capacity data using the directly measured amorphous heat capacity in our study ($\rho_{\mathrm{Run1}} = 0.46$ nm^{-2}, see Sec.4.2). The heat capacity data fitted to

$$C(T) = \gamma T - \alpha T^2 + aC_{\mathrm{amor}}(T) \tag{A.5}$$

$$C_{\mathrm{amor}}(T) = \frac{0.9585}{1.96\log(1.3T)^2 - 2.0\log(1.3T) + 2.555} + 0.00231. \tag{A.6}$$

The fit results is shown in Fig.A.1. The a coefficient obtained from the fitting is plotted in Fig.A.2. a moderately increase with increasing density up to about 4.4 nm^{-2}. However at $\rho > 4.4$ nm^{-2} the increase in a coefficient become steeper, shown as the open symbols of Fig.A.2. Such a drastic change indicate that the assumption of the Fermi liquid is no longer valid in this density range.

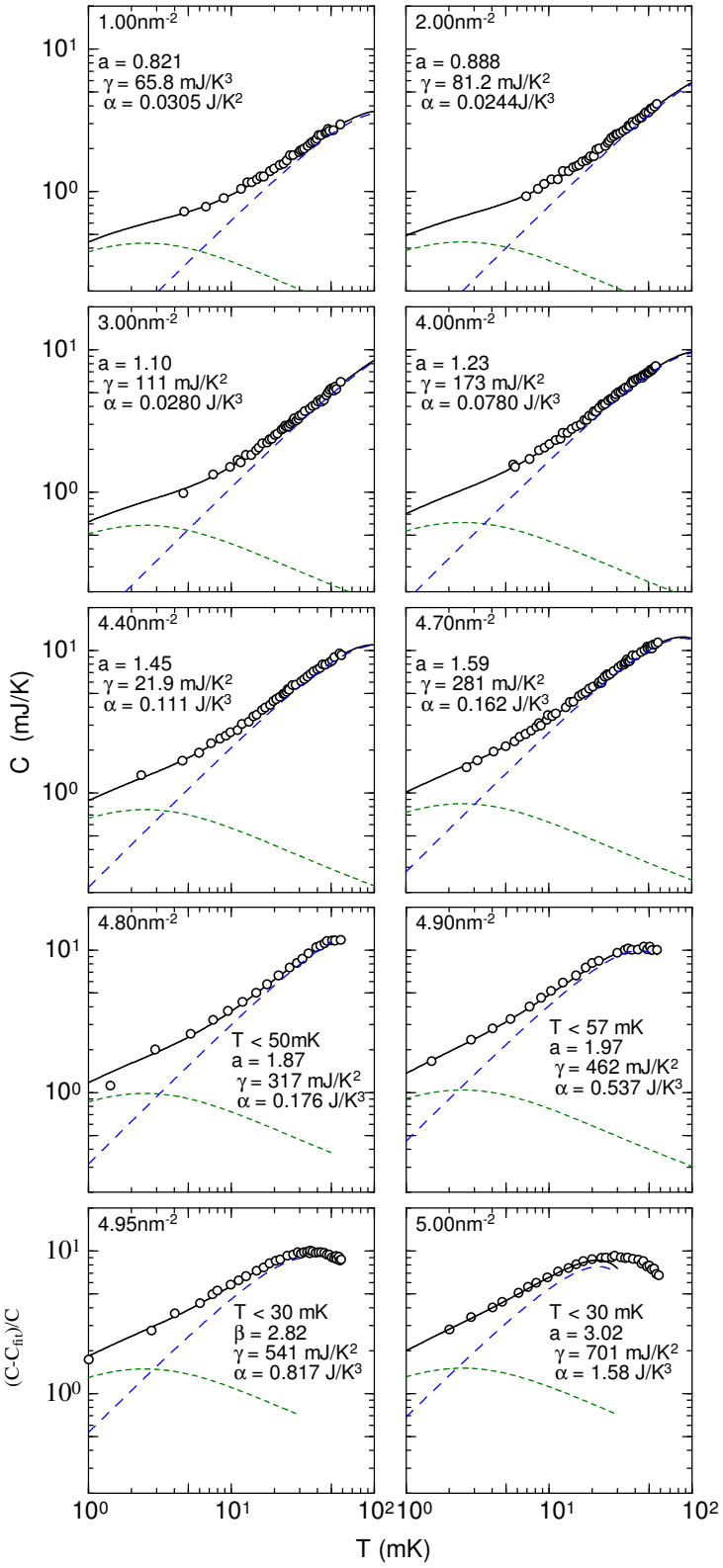

Fig. A.1: Refitting of heat capacity data from Ref.[39] using Eq.A.5. The blue and green lines are the liquid and amorphous contribution, respectively.

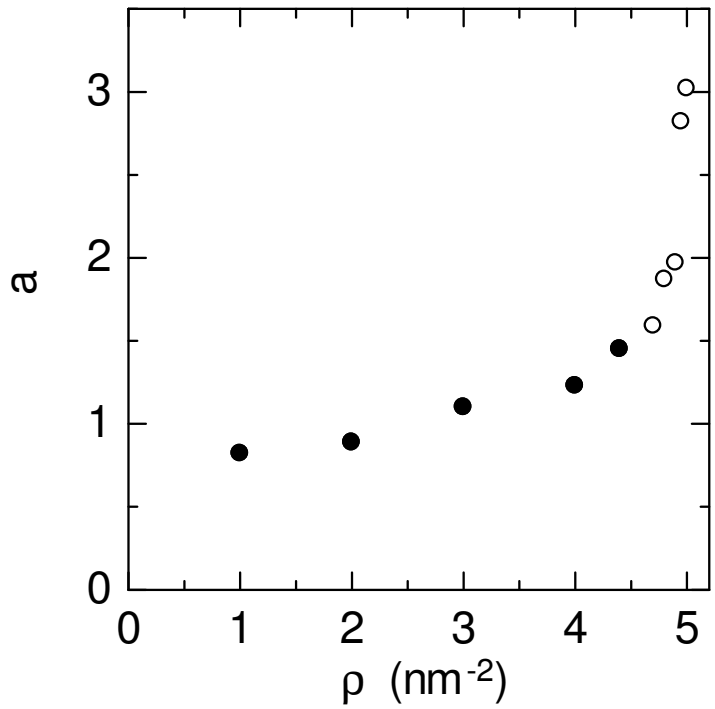

Fig. A.2: The a coefficient in Eq.(A.5) obtained by the data fitting shown in Fig.A.1. Rapid increase of a at $\rho > 4.4$ nm^{-2} indicates that the assumption of the Fermi liquid is no longer valid.

Appendix B

Ortho-para conversion heating of a bilayer H_2 on Grafoil

As mentioned in Sec.2.2, a bilayer H_2 is avoided as the substrate of ^{3}He monolayer for sub mK measurements, because of heat emission by conversion between ortho- and para-H_2. These states correspond to spin triplet and singlet states of nuclear spins. Abundance ratio of ortho- and para-H_2 at room temperature is 3:1, reflecting the degree of degeneracy. However, when temperature decrease ortho-H_2 convert to para-H_2 increase because the ground state energy of para-H_2 is 14.7 meV smaller than that of ortho-H_2. Heat release from this conversion is harmful for cooling down to ultra low temperature. In this section, we report the measurement of heat release from a bilayer H_2 on Grafoil at mK temperatures to testify the feasibility of it for the experiment at ultra low T.

We made a bilayer H_2 whose areal density is 17.52 nm^{-2}, corresponding to 2.03 layer [19]. H_2 gas was introduced into the cell at $T > 17$ K to prevent H_2 from being frozen in a capillary before reaching the sample cell. 7 days after fabricating H_2 film, we cooled the refrigerator and measured the speed of natural warm up from 30 mK in adiabatic condition. Heat release deduced by the speed and the addendum heat capacity, shown in Fig.B.1 was $\approx$ 130 nW. Our experimental apparatus requires heat leak into the cell to be less than 1 nW for sub mK measurement, so measured value is too large. Abundance ratio of ortho-H_2 is $\approx$ 0.5 % if we assume that ortho-para conversion rate is 0.4 at $T < 6$ K % [117].

We measured heat release again 7 days after the 1st measurement. We obtained 7 $\pm$ 1 nW at $40 < T < 70$ mK, which was measured by the same method as that used after the first time, as shown in Fig.B.1. Heat release become about 1/20 of the value after the first anneal and abundance ratio of ortho-H_2 become 0.03 %, but it is still too larger than is required.

Finally we estimate the conversion rate. When we assume the rate is insensitive to temperature below $T = 20$ K [118], ortho-para conversion rate is 33 $\pm$ 3 %/day, so heat release may be below 1 nW by waiting 5 extra days.

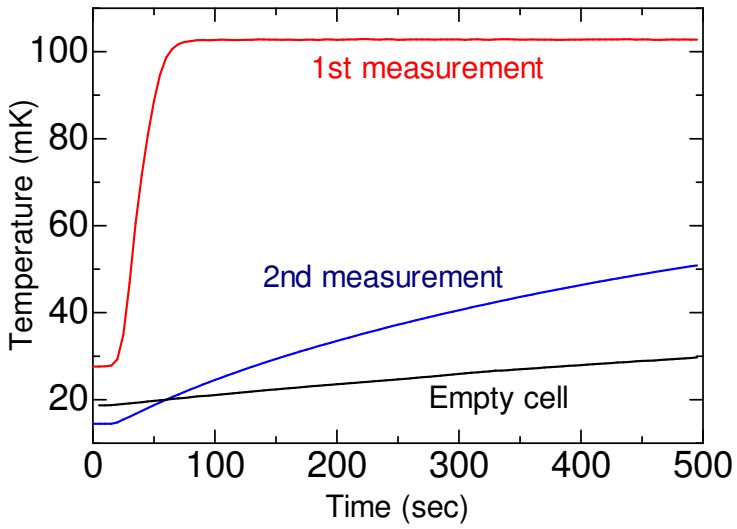

Fig. B.1: Natural warm up after the Zn HSW is opened at $t = 0$. The data of the empty cell (addendum) is also plotted for comparison.

Bibliography

[1] J. M. Kosterlitz and D. J. Thouless, J. Phys. C **6**, 1181 (1973).

[2] D. J. Bishop and J. D. Reppy, Phys. Rev. Lett **40**, 1727 (1978).

[3] K. v. Klitzing, G. Dorda, and M. Pepper, Phys. Rev. Lett **45**, 494 (1980).

[4] D. C. Tsui, H. L. Stormer, and A. C. Gossard, Phys. Rev. Lett **48**, 1559 (1982).

[5] J. G. Bednorz and K. A. Muller, Z. Phys. B **64**, 189 (1986).

[6] K. Ishida, M. Morishita, K. Yawata, and Hiroshi Fukuyama, Phys. Rev. Lett. **79**, 3451 (1997).

[7] R. Masutomi, Y. Karaki, and H. Ishimoto, Phys. Rev. Lett. **92**, 025301 (2004).

[8] R. A. Aziz, V. P. S. Nain, J. S. Carley, W. L. Taylor, and G. T. McConville, J. Chem. Phys **70**, 4330 (1979).

[9] L. C. van den Bergh and A. Schouten, J. Chem Phys. **89**, 2336 (1988).

[10] M. W. Cole, D. R. Frankl, and D. L. Goodstein, Rev. Mod. Phys. **53**, 199 (1981).

[11] manufactured by Union Carbide Corporation.

[12] Y. Niimi, T. Matsui, H. Kambara, K. Tagami, M. Tsukada, and H. Fukuyama, Phys. Rev. B **73**, 085421 (2006).

[13] W. E. Carlos and M. W. Cole, Phys. Rev. B **21**, 3713 (1980).

[14] M. Roger, C. Bäuerle, H. Godfrin, L. Pricoupenko, and J. Treiner, J. Low Temp. Phys. **112**, 451 (1998).

[15] E. Ilisca, Prog. Surf. Sci. **41**, 217 (1992).

[16] S. Nakamura, K. Matsui, S. Matsui, and H. Fukuyama, Phys. Rev. B **94**, 180501 (2016).

[17] H. Ikegami, R. Masutomi, K. Obata, and H. Ishimoto, Phys. Rev. Lett. **85**, 5146 (2000).

[18] A. Casey, H. Patel, J. Nyéki, B. P. Cowan, and J. Saunders, J. Low. Temp. Phys. **113**, 265 (1998).

[19] H. Wiechert, *Excitations in Two−Dimensional and Three−Dimensional Quantum Fluids*, Edited by A. G. F. Wyatt, and H. J. Lauter, Prenum Press, p499 (1991).

[20] D. Sato, D. Tsuji, S. Takayoshi, K. Obata, T. Matsui, and H. Fukuyama, J. Low Temp. Phys. **158**, 201 (2010).

[21] M. Siqueira, C. P. Lusher, B. P. Cowan, and J. Saunders, Phys. Rev. Lett. **71**, 1407 (1993).

[22] M. C. Gordillo and J. Boronat, private communication.

[23] D. Sato, K. Naruse, T. Matsui, and H. Fukuyama, Phys. Rev. Lett. **109**, 235306 (2012).

[24] D. S. Greywall and P. A. Busch, Phys. Rev. Lett. **65**, 2788 (1990).

[25] D. S. Greywall, Phys. Rev. B **41**, 1842 (1990).

[26] V. Elser, Phys. Rev. Lett. **62**, 2405 (1989).

[27] T. Takagi, J. Phys. Conf. Series **150**, 032102 (2009).

[28] J. Saunders, C. P. Lusher, and B. P. Cowan, Phys. Rev. Lett. **64**, 2523 (1990).

[29] F. Y. Wu, Rev. Mod. Phys. **54**, 235 (1982).

[30] M. Bretz, Phys. Rev. Lett. **38**, 501 (1977).

[31] S. Nakamura, K. Matsui, T. Matsui, and H. Fukuyama, J. Low Temp. Phys. **171**, 7115 (2013).

[32] H. Freimuth and H. Wiechert, Phys. Rev. B **42**, 587 (1990).

[33] S. N. Coppersmith, D. S. Fisher, B. I. Halperin, P. A. Lee, and W. F. Brinkman, Phys. Rev. Lett. **46**, 549 (1982).

[34] H. J. Lauter, H. P. Schildberg, H. Godfrin, H. Wiechert, and R. Haensel, Can. J. Phys. **65**, 1435 (1987).

[35] H. J. Lauter, H. Godfrin, V. L. P. Frank, and H. P. Schildberg, Physica B **165 &** **166**, 597 (1990).

[36] Y. Matsumoto, Ph.D. Thesis, The University of Tokyo (2003).

[37] D. Sato, Takayoshi, K. Obata, T. Matsui, and H. Fukuyama, J. Low Temp. Phys. **158**, 544 (2010).

[38] R. C. Ramos Jr, P. S. Ebey, and O. E. Vilches, J. Low Temp. Phys. **110**, 615 (1998).

[39] A. Casey, H. Patel, J. Nyéki, B. P. Cowan, and J. Saunders, Phys. Rev. Lett. **90**, 115301 (2003).

[40] R. Masutomi, Ph.D thesis, The University of Tokyo (2003).

[41] M. Morishita, H. Nagatani, and Hiroshi Fukuyama, Physica B **284-288**, 228 (2000).

[42] A. Golov and F. Pobell, Phys. Rev. B **53**, 12647 (1996).

[43] Y. Matsumoto, D. Tsuji, S. Murakawa, H. Akisato, H. Kambara, and H. Fukuyama, J. Low. Temp. Phys. **138**, 271 (2005).

[44] M. Morishita, H. Nagatani, and Hiroshi Fukuyama, Phys. Rev. B **65**, 104524 (2002).

[45] A. Casey, H. Patel, M. Siqueira, C. P. Lusher, J. Nyéki, B. Cowan, and J. Saunders, Physica B **284**, 224 (2000).

[46] D. D. Osheroff, Physica **109-110B**, 1461 (1982).

[47] E. D. Adams, Y. H. Tang, and K. Uhlig, J. Low Temp. Phys. **84**, 109 (1991).

[48] D. S. Greywall and P. A. Busch, Phys. Rev. B **36**, 6853 (1987).

[49] D. D. Osheroff, M. C. Cross, and D. S. Fisher, Phys. Rev. Lett. **44**, 792 (1980).

[50] T. C. Prewitt and J. M. Goodkind, Phys. Rev. Lett. **39**, 1283 (1977).

[51] M. Roger, J. H. Hetherington, and J. M. Delrieu, Rev. Mod. Phys. **55**, 1 (1983).

[52] M. Roger, Phys. Rev. B **30**, 6432 (1984).

[53] B. Bernu and D. M. Ceperley, J. Phys.: Condens. Matter **14**, 9099 (2002).

[54] M. Roger, Phys. Rev. B **56**, R2928 (1997).

[55] B. Bernu, D. Ceperley, and C. Lhuillier, J. Low Temp. Phys. **89**, 589 (1992).

[56] C. Bäuerle, Y. M. Bunkov, S. N. Fisher, and H. Godfrin, Czech. J. Phys. **46**, 399 (1996).

[57] M. Roger, C. Bäuerle, Yu. M. Bunkov, A. S. Chen, and H. Godfrin, Phys. Rev. Lett. **80**, 1308 (1998).

[58] D. Sato, Ph.D thesis, The University of Tokyo (2011).

[59] B. Bernu and G. Misguich, Phys. Rev. B **63**, 134409 (2001).

[60] E. Collin, Ph.D. Thesis, (2002).

[61] G. Misguich, B. Bernu, C. Lhuillier, and C. Waldtmann, Phys. Rev. Lett. **81**, 1098 (1998).

[62] T. Momoi, H. Sakamoto, and K. Kubo, Phys. Rev. B **59**, 9491 (1999).

[63] G. Misguich, C. Lhuillier, and B. Bernu, Phys. Rev. B **60**, 1064 (1999).

[64] M. Roger, Phys. Rev. Lett. **64**, 297 (1990).

[65] O. I. Motrunich, Phys. Rev. B **72**, 045105 (2005).

[66] T. Koretsune, M. Udagawa, and A. Schouten, Phys. Rev. B **80**, 075408 (2009).

[67] Y. Fuseya and M. Ogata, J. Phys. Soc. J. **78**, 013601 (2009).

[68] S. Watanabe and M. Imada, J. Phys. Soc. J. **76**, 075408 (2009).

[69] K. Watanabe, H. Kawamura, H. Kaneko, and T. Sakai, J. Phys. Soc. J. **83**, 034714 (2014).

[70] M. Ogura and H. Namaizawa, J. Phys. Soc. Jpn. **66**, 3706 (1997).

[71] D. Vollhardt, Rev. Mod. Phys. **56**, 99 (1984).

[72] M. Imada, J. Phys. Soc J. **64**, 2954 (1995).

[73] S. G. Sydriak, E. R. Grilly, and E. F. Hammel, Phys. Rev. **75**, 303 (1949).

[74] M. D. Miller and L. H. Nosanow, J. Low Temp. Phys. **32**, 145 (1978).

[75] V. Grau, J. Boronat, and J. Casulleas, Phys. Rev. Lett. **89**, 045301 (2002).

[76] B. K. Bhattacharyya and F. M. Gasparini, Phys. Rev. Lett. **49**, 919 (1982).

[77] M. C. Gordillo and J. Boronat, Phys. Rev. Lett. **116**, 145301 (2016).

[78] M. C. Gordillo and J. Boronat, Phys. Rev. B **94**, 165421 (2016).

[79] M. Ruggeri, E. Vitali, D. E. Galli, M. Boninsegni, and S. Maroni, Phys. Rev. B **93**, 104102 (2016).

[80] P. W. Anderson, Mat. Res. Bull. **8**, 153 (1973).

[81] D. A. Huse and V. Elser, Phys. Rev. Lett. **60**, 2531 (1988).

[82] B. Bernu, P. Lecheminant, C. Lhuillier, and L. Pierre, Phys. Rev. B **50**, 10048 (1994).

[83] L. Balents, Nature **464**, 199 (2010).

[84] Y. Zhou, K. Kanoda, and T-K. Ng, Rev. Mod. Phys. **89**, 025003 (2017).

[85] Y. Shimizu, K. Miyagawa, K. Kanoda, M. Maesato, and G. Saito, Phys. Rev. Lett. **91**, 107001 (2003).

[86] J. S. Helton, K. Matan, M. P. Shores, E. A. Nytko, B. M. Bartlett, Y. Yoshida, Y. Takano, A. Suslov, Y. Qiu, J. H. Chung, D. G. Nocera, and Y. S. Lee, Phys. Rev. Lett. **98**, 107204 (2007).

[87] T-H. Han, J. S. Helton, S. Chu, D. G. Nocera, J. A. Rodriguez-Rivera, C. Broholm, and Y. S. Lee, Nature **492**, 406 (2012).

[88] Y. Okamoto, M. Nohara, H. Aruga−Katori, and H. Takagi, Phys. Rev. Lett. **99**, 137207 (2007).

[89] H. Yamaguchi, M. Okada, Y. Kono, S. Kittaka, T. Sakakibara, T. Okabe, Y. Iwasaki, and Y. Hosokoshi, Sci. Rep. **7**, 16144 (2017).

[90] T. Itou, A. Oyamada, S. Maegawa, and R. Kato, Nat. Phys. **6**, 673 (2010).

[91] T. Isono, H. Kamo, A. Ueda, K. Takahashi, M. Kimata, H. Tajima, S. Tsuchiya, T. Terashima, S. Uji, and H. Mori, Phys. Rev. Lett. **112**, 177201 (2014).

[92] S. Yamashita, T. Yamamoto, Y. Nakazawa, M. Tamura, and R. Kato, Nat. Commun. **2**, 275 (2011).

[93] M. Yamashita, N. Nakata, Y. Senshu, M. Nagata, H. M. Yamamoto, R. Kato, T. Shibauchi, and Y. Matsuda, Science **328**, 1246 (2010).

[94] H. D. Zhou, E. S. Choi, L. Balicas G. Li, C. R. Wiebe, Y. Qiu, J. R. D. Coplay, and J. S. Gardner, Phys. Rev. Lett. **106**, 147204 (2011).

[95] Y. Li, D. Adroja, P. K. Biswas, P. J. Baker, Q. Zhang, J. Liu, A. A. Tsirlin, P. Gegenwart, and Q. Zhang, Phys. Rev. Lett. **117**, 097201 (2016).

[96] J. A. M. Paddison, M. Daum, Z. Dun, G. Ehlers, Y. Liu, M. B. Stone, H. Zhou, and M. Mourigal, Nat. Phys. **13**, 117 (2016).

[97] S. Murakawa, Ph.D. Thesis, The University of Tokyo (2005).

[98] D. S. Greywall, Phys. Rev. B **33**, 7520 (1986).

[99] J. P. Shepherd, Rev. Sci. Instrum **56**, 273 (1985).

[100] Y. M. Liu, P. S. Ebey, O. S. Vilches, and J. G. Dash, Phys. Rev. B **54**, 6307 (1996).

[101] H. J. Hoge and Arnold R. D, J. Res. Natl. Bur. Stand. **47**, 63 (1951).

[102] T. R. Roberts and S. G. Sydriak, Phys. Rev. **102**, 304 (1956).

[103] B. I. Halperin and D. R. Nelson, Phys. Rev. Lett. **41**, 121 (1978).

[104] H. Nema, A. Yamaguchi, T. Hayakawa, and H. Ishimoto, Phys. Rev. Lett. **102**, 075301 (2009).

[105] S. V. Hering, S. W. Van Sciver, and O. E. Vilches, J. Low Temp. Phys. **25**, 793 (1976).

[106] M. Bretz, J. G. Dash, D. C. Hickernell, E. O. McLean, and O. E. Vilches, Phys. Rev. A **8**, 1589 (1973).

[107] S. Tasaki, Prog. Theor. Phys. **79**, 1311 (1988).

[108] D. Sato, Master thesis, The University of Tokyo (2008), unpublished.

[109] M. Yamashita, N. Nakata, Y. Kasahara, T. Sasaki, N. Yoneyama, N. Kobayashi, S. Fujimoto, T. Shibauchi, and Y. Matsuda, Nat. Phys. **5**, 44 (2009).

[110] R. B. Biswas, L. Fu, C. R. Laumann, and S. Sachdev, Phys. Rev. B **83**, 245131 (2011).

[111] Y. R. Wang, Phys. Rev. B **45**, 21 (1992).

[112] Y. Li, H. Liao, Z. Zhang, S. Li, F. Jin, L. Ling, L. Zhang, Y. Zou, L. Pi, Z. Yang, J. Wang, Z. Wu, and Q. Zhang, Sci. Rep. **5**, 16419 (2015).

[113] H. Kajueter, G. Kotliar, and G. Moeller, Phys. Rev. B **53**, 16214 (1996).

[114] F. Gasparini, H. Holler, and E. Krotscheck (unpublished).

[115] W. E. Carlos and M. W. Cole, Surf. Sci **91**, 339 (1980).

[116] E. Collin, S. Triqueneaux, R. Harakaly, M. Roger, C. Bäuerle, Yu. M. Bunkov, and H. Godfrin, Phys. Rev. Lett. **86**, 2447 (2001).

[117] P. R. Kubik, W. N. Hardy, , and H. Glattli, Can. J. Phys. **63**, 605 (1985).

[118] S. Yucel, N. Alexander, and A. Honig, Phys. Rev. B **42**, 820 (1990).